

Improving the Excitation Efficiency of Surface Plasmon Polaritons Near Small Apertures in Metallic Films

by

Reyad Mehfuz

B.Sc., Bangladesh University of Engineering and Technology, 2004
M.Sc., International Islamic University Malaysia, 2008

A THESIS SUBMITTED IN PARTIAL FULFILLMENT OF
THE REQUIREMENTS FOR THE DEGREE OF

DOCTOR OF PHILOSOPHY

in

THE COLLEGE OF GRADUATE STUDIES

(Electrical Engineering)

THE UNIVERSITY OF BRITISH COLUMBIA

(Okanagan)

November 2013

© Reyad Mehfuz, 2013

Abstract

Light incident onto a small aperture in a metal film can convert into light waves bound to the surface of that film. At visible frequencies and beyond, these surface-bound waves are commonly known as surface plasmon polaritons (SPPs). In this work, we explore ways to enhance the excitation efficiency of SPPs in the vicinity of a slit aperture. We introduce a basic method to treat this problem in which the slit and adjacent metal surface are approximated as independent waveguides. By mapping out the electromagnetic modes sustained by the waveguide components approximating the slit structure, we predict enhanced SPP excitation efficiency when wave vector matching is achieved between the waveguide modes. The concept of wave vector matching is applied to investigate SPP coupling efficiencies for various slit geometries and material configurations. We consider slits with dimensions comparable to the incident wavelength, categorizing this work into explorations of sub-wavelength and super-wavelength slits. We show that SPP coupling from a sub-wavelength slit can be enhanced by placing a dielectric layer onto the exit side of the metal surface. By varying the layer thickness, it is possible to tune the efficiency of SPP coupling, which can be enhanced significantly (about six times) relative to that without the layer. Broadband enhancement of SPP coupling from a sub-wavelength slit over most of the visible spectrum is demonstrated using the same method. We also show that high-efficiency SPP coupling can be achieved using a super-wavelength slit. We hypothesize that higher-order modes in a large slit can assist wave vector matching and boost SPP coupling. Enhanced SPP excitation in a super-wavelength slit aperture is first shown using numerical simulations, and later verified with experiments. Overall, the thesis demonstrates that simple wave vector matching conditions, similar to classical SPP coupling methods based on prisms or gratings, can also be applied to describe SPP coupling in small slit apertures. The thesis also provides insights into the role of different parameters, such as slit width, dielectric layer thickness and surrounding dielectric media, in realizing significant enhancements in SPP coupling efficiencies.

Preface

This work has been done under the guidance of Dr. Kenneth Chau at the School of Engineering in The University of British Columbia. Portions of my thesis have been published in three journal articles:

- R. Mehfuz, F. A. Chowdhury, and K. J. Chau, “Imaging slit-coupled surface plasmon polaritons using conventional optical microscopy”, *Optics Express*, vol. 20, pp. 10527-10537, 2012.
- R. Mehfuz, M. W. Maqsood, and K. J. Chau, “Enhancing the Efficiency of Slit-Coupling to Surface-Plasmon Polariton via Dispersion Engineering,” *Optics Express*, vol. 18, pp. 18206-18216, 2010.
- M. W. Maqsood, R. Mehfuz, and K. J. Chau, “High-throughput diffraction assisted surface-plasmon-polariton coupling by a super-wavelength slit,” *Optics Express*, vol. 18, pp. 21669-21677, 2010.

Portions of my thesis have also been presented at the following conferences:

- R. Mehfuz and K. J. Chau, “Surface plasmon polariton coupling from a slit: can bigger be better?” SPP6, Ottawa, Canada, 2013.
- R. Mehfuz and K. J. Chau, “Far-field detection and imaging of surface plasmon polaritons by engineering sub-wavelength slit-structure,” SPIE Optics+Photonics, San Diego, USA, 2012.
- R. Mehfuz and K. J. Chau, “Design of Metal-Dielectric Sub-Wavelength Slit Structure for High Efficiency Coupling of Surface Plasmon Polaritons,” Photonics North, Ottawa, Canada, 2011.

Table of Contents

Abstract	ii
Preface	iii
Table of Contents	iv
List of Tables	vii
List of Figures	viii
Acknowledgements	xx
Dedication	xxi
Chapter 1: Introduction	1
1.1 Early work on light diffraction through apertures	1
1.2 Maxwell's equations	4
1.3 Kirchhoff's scalar diffraction theory	6
1.4 Helmholtz-Kirchhoff integral equation for scalar diffraction	7
1.5 Kirchhoff's formulation of scalar diffraction by a plane screen	10
1.6 Fraunhofer diffraction and the Fourier transform	12
1.7 Bethe's vectorial diffraction theory	15
1.8 Scalar wave equation for two-dimensional problems	16
1.9 Angular spectrum representation	17
1.10 Scalar diffraction through small slits	18
1.11 Computational solvers for Maxwell's equations	19
1.11.1 Finite-difference time-domain method	20
1.11.2 Finite-difference frequency-domain method	21
1.11.3 Application of FDTD and FDFD to model light transmission through a slit	22

TABLE OF CONTENTS

1.12	Recent research interest in light transmission through aperture in metallic films	22
1.13	Surface plasmon polaritons	24
1.13.1	Excitation of surface plasmon polaritons	29
1.14	Understanding aperture coupling to surface plasmon polaritons	32
1.15	Improving the excitation efficiency of surface plasmon polaritons	36
1.16	Thesis outline	38
Chapter 2: Improving the SPP Coupling Efficiency Near a Sub-wavelength Slit 39		
2.1	SPP coupling from a coated slit	40
2.2	Numerical investigation of enhanced SPP coupling	44
2.2.1	Simulation design	44
2.2.2	Control studies	46
2.2.3	Results	48
2.3	Experimental investigation of enhanced SPP coupling	54
2.3.1	Fabrication	55
2.3.2	Experimental design	55
2.3.3	SPP measurement	57
2.3.4	SPP coupling efficiency measurements	62
2.3.5	SPP propagation distance measurements	65
2.3.6	SPP lensing using an array of holes	66
2.4	Broadband enhancement of SPP coupling	67
2.4.1	Fabrication	67
2.4.2	Experimental design	68
2.4.3	Results	70
2.5	Summary	70
Chapter 3: Improving the SPP Coupling Efficiency Near a Super-wavelength Slit 74		
3.1	Hypothesis: enhanced SPP coupling due to higher-order modes	75
3.2	Simulation design	81
3.3	Simulation results	81
3.4	Experimental design	86
3.5	Experimental SPP coupling efficiency measurements	92
3.6	Summary	94
Chapter 4: Conclusion 97		
Bibliography 102		

TABLE OF CONTENTS

Appendices	112
Appendices A: Drude Model and its Limitations	112
Appendices B: Fabrication Tools	117

List of Tables

Table 2.1 Control simulation geometries and results. Fixed parameters include $w = 150$ nm, $d = 100$ nm, $t = 300$ nm, and $\lambda_0 = 500$ nm. 47

Table A.1 Plasma frequency and collision rate measured by Zeman and Sachts for Ag, Au, and Al 113

Table B.1 Spin speed of the Laurell WS-400B-6NPP-LITE coater versus the expected thickness and experimentally measured PMMA layer thickness 119

List of Figures

Figure 1.1	Huygens' secondary wavelet analysis of a wavefront passing through an opening in an opaque screen.	2
Figure 1.2	Image of the Arago spot in the shadow of a circular obstacle placed in a coherent beam. This image was used with permission.	3
Figure 1.3	Theoretical construct consisting of a closed surface S associated with a volume V and surrounding an observation point P_0 used to illustrate Green's theorem. Note that we take the normal direction to correspond to the outward normal.	8
Figure 1.4	Application of the Helmholtz-Kirchhoff integral theorem to solve for the scalar disturbance at an observation point P_0 when an opaque screen with an opening is placed between a source and the observation point.	11
Figure 1.5	Configuration used to analyze scalar diffraction from an opening in an opaque screen.	13
Figure 1.6	Configuration considered by Kowarz to analyze near-field diffraction from a slit.	19
Figure 1.7	Three-dimensional Yee Grid depicting the electric and magnetic field components distributed over a discrete spatial grid.	21
Figure 1.8	Application of the FDTD and FDFD method to solve the two-dimensional problem of TM-polarized plane-wave incident onto a slit in a metallic film. Figure (a) shows the schematic of the simulation grid consisting of a metallic film with a small opening, immersed in a dielectric. The simulation space is surrounded by a perfectly matched layer (PML). Figures (b) and (c) show the calculated magnetic field distribution about the aperture obtained using the FDFD and FDTD method, respectively.	23

LIST OF FIGURES

Figure 1.9	A single interface between two disparate media can, under certain conditions, sustain surface waves that obey Maxwell's equations.	25
Figure 1.10	Schematic of the TM-polarized electromagnetic waves and surface charges associated with SPPs at the interface of a metal and dielectric.	27
Figure 1.11	Dispersion relation of a SPP wave and a free-space plane wave. k_{spp} and k_0 are the wave vectors of a SPP wave and free-space plane wave, respectively. At any given frequency, k_{spp} is larger than k_0	28
Figure 1.12	Schematic of light coupling to SPPs by using a prism. (a) Mechanism of wave vector matching by prism coupling, manifested in the (b) Kretschmann configuration and (c) Otto configuration.	30
Figure 1.13	Schematic of free-space light coupling to SPPs using a grating immersed in free-space.	31
Figure 1.14	Schematic of the coupling of free-space light to SPPs by an aperture.	33

LIST OF FIGURES

Figure 1.15 (a) Three-dimensional plasmonic nano-focusing of light with asymmetrically patterned silver pyramids showing i) a scanning electron microscope (SEM) image of the device, ii) a side-view of the scanning confocal Raman image at an incident wavelength of 710 nm. (b) Splitting of surface plasmons into two channels, showing i) a SEM image and ii) a near-field optical image at an incident wavelength of 1600 nm. (c) Sub-wavelength focusing of surface plasmon to a 250-nm-wide Ag strip guide with a curved array of holes, showing i) a SEM image (light gray, Ag and dark gray, Cr) and ii) a near-field optical image of SPP focusing and guiding at a wavelength of 532 nm. (d) Surface plasmon propagation along a 18.6 μm long silver nano-wire at an incident wavelength of 785 nm, showing i) a sketch of optical excitation where I is the input and D is the end of the wire, ii) a conventional optical microscopic image showing the bright spot to the left is the focused exciting light, iii) a near-field optical image corresponding to the white box in ii, and iv) a 2- μm -long cross-cut along the chain dotted line in iii. (e) Surface plasmon waveguiding, showing i) a SEM image and ii) photon scanning tunneling microscopy image at a wavelength of 800 nm. 34

Figure 1.16 (a) Basic two-dimensional configuration to be studied consisting of a slit in a metallic film. The slit structure is conceptually divided into two uni-axial semi-infinite waveguides: (b) a vertical metal-dielectric-metal (MDM) waveguide, which sustains longitudinal and transverse wave vector components k_z and k_x , respectively, and (c) a horizontal metal-dielectric (MD) waveguide, which sustains a longitudinal wave vector component k_{spp} along the metal-dielectric interface. Wave vector matching is achieved when the transverse component of the wave vector in the MDM waveguide matches with the longitudinal component of the wave vector in the MD waveguide. 37

LIST OF FIGURES

Figure 2.1	(a) Real-space (left) and k -space (right) depictions of the modes scattering from the exit of a slit in a metal film when the metal film is completely immersed in a dielectric. (b) Real-space (left) and k -space (right) depictions of the modes scattering from the exit of a slit in a metal film when the slit is filled with a dielectric and the metal film is coated with a dielectric layer.	41
Figure 2.2	Simulation geometry used to study SPP coupling from an illuminated slit. The detectors D_1 and D_2 capture the SPP modes, and the detector D_3 captures the radiating modes.	45
Figure 2.3	Image of the FDTD-calculated instantaneous $ H_y ^2$ distribution for a slit of width $w = 150$ nm illuminated by a quasi-plane-wave of wavelength $\lambda_0 = 500$ nm. The simulation geometry is depicted by the above graphic. Lines indicating the position of detectors D_1 , D_2 , and D_3 have been superimposed on the image.	48
Figure 2.4	Basic principle used to enhance slit-coupling to SPP modes near a sub-wavelength slit in a metallic film. (a) Dispersion curve of n_{spp} as a function of λ_0 for various d calculated from the roots of the eigenvalue equation for the SPP mode on an asymmetric, three-layer silver-glass-air waveguide. (b) n_{spp} as a function of d for $\lambda_0 = 500$ nm. The dotted gray line corresponds to the refractive index of a plane-wave mode in glass, $\sqrt{\epsilon_d}$	49
Figure 2.5	Image of the FDTD-calculated instantaneous $ H_y ^2$ distribution for a slit of width $w = 150$ nm illuminated by a quasi-plane-wave of wavelength $\lambda_0 = 500$ nm when a dielectric layer of thickness (a) 100 nm and (b) 500 nm is placed on the metal film. The simulation geometry is depicted by the above graphic.	50
Figure 2.6	(a) The time-averaged SPP intensity, I_{SPP} (blue squares), and time-averaged radiated intensity, I_r (red circles), and (b) the corresponding SPP coupling efficiency, η , as a function of d . The error bars describe the uncertainties in the measurement of I_{SPP} and I_r due to, respectively, the finite amount of I_r captured by D_1 and D_2 and the finite amount of I_{SPP} captured by D_3	51

LIST OF FIGURES

Figure 2.7	SPP wavelength measured from the FDTD simulations (blue squares) and predicted from the mode solver (red line) as a function of dielectric layer thickness d . The dotted gray line indicates the value of $\lambda_i = \lambda_0/\sqrt{\epsilon_d}$. The error bars describe the uncertainty in the measurement of λ_{spp} from the FDTD simulations due to variation in λ_{spp} as a function of distance from the slit exit.	52
Figure 2.8	Image of the FDTD-calculated instantaneous $ H_y ^2$ distribution for a slit illuminated by a quasi-plane-wave of wavelength $\lambda_0 = 500$ nm when the slit width is (a) 150 nm and (b) 300 nm. The dielectric layer thickness $d = 100$ nm is held constant. The simulation geometry is depicted by the above graphic. . . .	53
Figure 2.9	a) The time-averaged SPP intensity, I_{SPP} (blue squares), and time-averaged radiated intensity, I_r (red circles), and (b) the corresponding SPP coupling efficiency, η , as a function of w . The error bars describe the uncertainties in the measurement of I_{SPP} and I_r due to, respectively, the finite amount of I_r captured by D_1 and D_2 and the finite amount of I_{SPP} captured by D_3	54
Figure 2.10	Simulation procedure to determine an upper bound for the slit width, for an arbitrary set of parameters, when the slit is filled with a dielectric and loaded with a dielectric layer. Image of the FDTD-calculated instantaneous $ H_y ^2$ distribution for a slit illuminated by a quasi-plane-wave of wavelength $\lambda_0 = 500$ nm when the slit width is (a) 150 nm, (b) 200 nm, (c) 250 nm, (d) 300 nm, (e) 350 nm, and (f) 450 nm. Dispersionless glass with the refractive index of 1.5 is used as the dielectric. The dielectric layer thickness $d = 100$ nm is held constant. Note the transition of the field profile in the slit as the slit width increases.	56

LIST OF FIGURES

Figure 2.11	<p>(a) $\text{Re}[k_{spp}]$ corresponding to SPP modes propagating along a silver metal surface coated with a dielectric layer of refractive index $n = 1.5$ and surrounded by air, for various layer thickness values, along with the nk_0 line. Complex k_{spp} values are calculated by solving the dispersion relation of a semi-infinite three-layer silver-glass-air waveguide, where the permittivity of silver is fitted to experimental data. The circles highlight, for a given dielectric layer thickness, the frequency at which the momentum matching condition $\text{Re}[k_{spp}] = nk_0$ is satisfied. It should be noted that the momentum matching condition is an approximation and provides only a first-order procedure to estimate the optimal dielectric layer thickness. (b) Schematic of the experimental set-up. Polarized light from a He-Ne laser ($\lambda_0 = 632.8 \text{ nm}$) illuminates the sample and the far-field transmission image is captured by an optical microscope (Zeiss Axio Imager) using a $100\times$ objective lens with a numerical aperture of 0.90 in air ambient and recorded using a Si CCD camera.</p>	58
Figure 2.12	<p>Representative microscope images of the slit and grooves for (a) an uncoated sample, (b) a coated sample with PMMA layer thickness $d = 80 \text{ nm}$, and (c) a coated sample with PMMA layer thickness $d = 120 \text{ nm}$. The width of the slits is $w = 150 \text{ nm}$. The left column shows scanning electron microscope (SEM) images, and the middle and right columns show optical microscope images under x-polarized and y-polarized illumination, respectively. The color of the optical microscope images has been modified for clarity, but the images are otherwise unprocessed.</p>	59

LIST OF FIGURES

Figure 2.13	<p>Experiment to distinguish diffraction from a slit and SPP scattering from adjacent grooves. (a) SEM image of a representative sample consisting of two identical slits of width $w = 150$ nm, one of which is flanked by grooves. The sample is coated with a PMMA layer of thickness $d = 80$ nm. Optical microscope image of the sample under (b) x-polarized illumination and (c) y-polarized illumination. We apply a subtraction procedure to images (b) and (c) in which the region R2 is subtracted from R1. The resulting subtracted image derived from (b) show bright spots at the groove location indicative of SPP scattering. These bright spots are absent in the subtracted image derived from (c), suggesting the absence of SPPs.</p>	61
Figure 2.14	<p>(a) SPP coupling efficiency, η, as a function of the PMMA layer thickness, for a fixed slit width of $w = 150$ nm. η is measured using two methods. In the first method, labeled “expt-1”, η is calculated by using $I_{ng,L}$ and $I_{ng,R}$ derived from the image of the slit and grooves under y-polarized illumination and then using Eq. (2.13) (red circles). In the second method, labeled “expt-2”, η is calculated by using $I_{ng,L}$ and $I_{ng,R}$ derived from the image of the slit with no grooves under x-polarized illumination and then using Eq. (2.13) (magenta diamond). We calculate η from two-dimensional FDTD simulations modeling x-polarized plane-wave illumination of a coated slit for various d values (blue squares). We also calculate, for the optimal case of $d = 80$ nm, the SPP coupling efficiency when a 20-nm-deep dimple is present in the dielectric layer above the slit (cyan square), which emulates possible non-planarity of the polymer layer due to conforming to the slit walls. (b) shows the SPP coupling efficiency measured using the method “expt-1” (red circles) and calculated using FDTD simulation (blue squares) as a function of the slit width. The error bars in (a) and (b) correspond to the variance of five independent measurements.</p>	63

LIST OF FIGURES

Figure 2.15	(a) SEM image of an array of identical $w = 150$ nm slits where the groove spacing from the slits is varied from $s = 1 \mu\text{m}$ to $s = 8 \mu\text{m}$ in $1 \mu\text{m}$ increments. The array is coated with a PMMA layer of thickness $d = 80$ nm. (b) shows the corresponding microscope image of the array. (c) depicts profiles of the image intensity along horizontal lines intersecting the slit and grooves for various slit-groove separation values. (d) The integrated SPP intensity normalized to the integrated intensity of the slit as a function of the slit-groove separation (red circles), where the blue line corresponds to an exponential fit.	64
Figure 2.16	Measurement of a focused SPP beam emitted from a curved array of sub-wavelength holes using optical microscopy. (a) SEM image of three plasmonic lenses consists of a curved array of holes, with different groove patterns milled adjacent to the lenses. The lenses consist of 17 holes, each of diameter $\simeq 200$ nm, milled into a semi-circle of radius $5 \mu\text{m}$. Optical microscope image of the three lenses under (b) x-polarized illumination and (c) y-polarized illumination.	66
Figure 2.17	(a) Experimental setup to characterize broadband SPP coupling using a slit-groove structure. Light from a tungsten light source is directed through a polarizer and is incident onto the slit structure. An image of the top of the slit structure is collected by a $100\times$ objective lens with numerical aperture of 0.9. The spectral data are collected by a spectrum analyzer, which is placed in the image plane of the microscope. (b, top) Spectrum of the light that is supplied from the tungsten source and (b, bottom) transmitted through the various slit structures.	69

LIST OF FIGURES

Figure 2.18	(a) SEM image of a slit-groove structure with slit-to-groove separation distances of $3\ \mu\text{m}$ and $6\ \mu\text{m}$. (b) Normalized intensity profile measured in the horizontal direction across the slit and grooves extracted from a transmission-mode microscope image of the structure shown in (a). (c) and (d) show the spectra collected by sampling at slit-to-groove separation distances of $3\ \mu\text{m}$ and $6\ \mu\text{m}$. (e) and (f) plot the ratio of the groove spectra of the coated samples to that of the uncoated samples for measurements taken at slit-to-groove separation distances of 3 and $6\ \mu\text{m}$	71
Figure 2.19	(a) SEM image of a slit-groove structure with slit-to-groove separation distances of $8\ \mu\text{m}$ and $10\ \mu\text{m}$. (b) Normalized intensity profile measured in the horizontal direction across the slit and grooves extracted from a transmission-mode microscope image of the structure shown in (a). (c) and (d) show the spectra collected by sampling at slit-to-groove separation distances of $8\ \mu\text{m}$ and $10\ \mu\text{m}$, respectively. (e) and (f) plot the ratio of the groove spectra of the coated samples to that of the uncoated samples for measurements taken at slit-to-groove separation distances of 8 and $10\ \mu\text{m}$, respectively.	72
Figure 3.1	Magnetic field profiles of the (a) TM_0 and (b) TM_1 modes at $\omega_0 = 6.0 \times 10^{14}$ Hz in an infinite metal-dielectric-metal (MDM) waveguide having a dielectric core thickness $w = 150$ nm. Silver is used as the metal and the core consists a dielectric of index 2.5. The field profiles are normalized so that the modes carry unit power in the upward direction.	76

LIST OF FIGURES

Figure 3.2	Formulation of a hypothesis for diffraction-assisted SPP coupling by a super-wavelength slit aperture. (a) Figure-of-merit and (b) the real transverse wave vector component versus frequency and wavelength for TM_0 and TM_1 modes sustained in slits of different widths. (c) Diffraction spectrum corresponding to the TM_0 mode in a 200-nm-wide slit and the TM_1 modes in 350 nm-wide and 500 nm-wide slits. (d) Wave vector-space depiction of diffraction-assisted SPP coupling from slits of width $w = 200$ nm, $w = 350$ nm, and $w = 500$ nm, immersed in a uniform dielectric of refractive index $n = 1.75$	78
Figure 3.3	Images of the FDTD-calculated instantaneous $ H_y ^2$ distribution (left) and the time-averaged $ H_y ^2$ angular distribution (right) for a slit of width values (a) $w = 150$ nm, (a) $w = 350$ nm, and (a) $w = 500$ nm immersed in a dielectric ($n=1.75$) and illuminated by a quasi-plane-wave of wavelength $\lambda_0 = 500$ nm. A common saturated color scale has been used to accentuate the fields on the exit side of the slit.	82
Figure 3.4	(a) SPP coupling efficiency as a function of optical slit width for dielectric refractive index values $n = 1.0$ (squares), $n = 1.5$ (circles), $n = 1.75$ (upright triangles), $n = 2.0$ (inverted triangles), $n = 2.5$ (diamonds). (b) The measured SPP intensity (circles), radiative intensity (squares), and total intensity (diamonds). The shaded region indicates the sub-wavelength-slit-width regime.	84
Figure 3.5	Wave vector mismatch as a function of refractive index of the dielectric region for a fixed optical slit width $nw = 600$ nm and free-space wavelength $\lambda_0 = 500$ nm.	85

LIST OF FIGURES

Figure 3.6	(a) SPP coupling from a slit in an opaque gold film. High-efficiency SPP coupling is achieved when the wave vector of light leaving the slit is wave vector matched with the SPP mode. Frequency dependence of the real parts of the (b) longitudinal and (c) lateral wave vector of the lowest-order modes in a Au-dielectric-Au waveguide, which approximates the slit structure. The refractive index of the dielectric is assumed to be 1.4. Note the large increase in the lateral wave vector of the first-order mode relative to that of the zero-order mode, which provides a wave vector boost needed for SPP coupling.	88
Figure 3.7	Schematic of the experimental set-up. The slit-groove structures etched into a gold film are immersed in a high-index fluid. TM-polarized light from a He-Ne laser ($\lambda_0 = 632.8$ nm) illuminates the sample and the far-field transmission image is captured using a CCD camera by oil immersion microscopy (100x objective lens and numerical aperture of 1.3). We place a cover slide and silicone oil successively on top of the high index fluid to avoid the possible damage of the eyepiece (as most of the high index fluid reacts).	89
Figure 3.8	Scanning electron microscope of a typical slit structure etched into a 300-nm-thick Au film by focused ion beam milling. The whitish boundary at the edge of the slit represents the blunted slit edges resulting from bombardment of a spherical ion beam.	91
Figure 3.9	(a) Representative SEM image of a sample of two identical slit structures ($w = 450$ nm) where the bottom slit is flanked by two grooves. (b) The far field image of the sample when it is immersed in a high index fluid ($n = 1.7$). The color map of the optical microscope images has been modified for clarity, but the images are otherwise unprocessed. (c) The normalized intensity profile obtained from the area bounded by dotted boxes in (b). Note the enhanced light intensity of the side lobes next to the slit due to the presence of the grooves.	92

LIST OF FIGURES

Figure 3.10	FDFD simulations of TM-polarized illumination ($\lambda_0=632.8$ nm) of a set of tapered slits (with parameters matching slit pairs with a nominal width of $w = 350$ nm used in the experiments) immersed in a dielectric medium where $n = 1.6$. (a) Energy density distribution for the case where the slit is (a) without grooves and (b) with grooves. (c) Normalized energy density profiles extracted from the simulations along the magenta line shown in (a) and (b), which approximates the object plane imaged by the microscope. . .	93
Figure 3.11	SPP coupling efficiency (η) as a function of the exit slit width (w_2) when immersed in index fluids of refractive index (a) 1.5, (b) 1.6, and (c) 1.7.	95
Figure 3.12	FDFD simulation of the electromagnetic response of a slit structure with a nominal width of $w = 350$ nm at $\lambda_0 = 632.8$ nm, with a zoomed-in section highlighting the fields at the slit exit. (b) Two-dimensional Fourier transformation applied to the fields at the slit exit, revealing large spatial frequency components along the horizontal (x) axis. (c) Plot of Fourier amplitude at the spatial frequency k_{spp} as a function of the slit width.	96
Figure 4.1	SPP coupling efficiency as a function of dielectric layer thickness calculated at representative wavelengths in the infrared, visible, and UV. For the case of UV illumination, the metal is aluminum, the slit width is 50 nm, and the incident wavelength is 250 nm. For the case of visible illumination, the metal is silver, the slit width is 100 nm, and the incident wavelength is 500 nm. For the case of IR illumination, the metal is gold, the slit width is 150 nm, and the incident wavelength is 822 nm.	100
Figure A.1	Permittivity values of gold predicted by the Drude model and obtained from experimental measurements	114
Figure A.2	Permittivity values of silver predicted by the Drude model and obtained from measurements	115
Figure A.3	Permittivity values of aluminum predicted by the Drude model and obtained from measurements	116

Acknowledgements

I have been fortunate to be surrounded by many wonderful people, and I want to take this opportunity to thank them all for their love, support and encouragement. First of all, I would like to express my sincere gratitude to my PhD advisor, Dr. Kenneth Chau, for his relentless support and guidance throughout my Doctoral studies. His confidence in my abilities was crucial for my smooth transition to become a contributor of knowledge in the exciting area of nano-scale photonics. His scientific brilliance, boundless energy and exemplary vision will forever be an inspiration.

I am thankful to Dr. Jonathan Holzman, Dr. Stephen O’Leary and Dr. Murray Neumann for their valuable comments and suggestions that helped enrich my work. I am grateful to Dr. Deborah Roberts for allowing me to use her microscope for the experimental portions of this work. I would like to thank Dr. Karen Kavanagh of Simon Fraser University (SFU) for supporting my research activities at the Nanoimaging facilities. I am specially thankful to Dr. Li Yang and Chris Ballicki of 4D labs, SFU for training me on different nanofabrication tools.

I have spent wonderful moments with my extraordinary research colleagues. Waqas Maqsood, Faqrul Alam Chowdhury, Samuel Schaefer, Mohammed Al-Shakhs and Max Bethune-Waddell have been a consistent source of support, sharing their views on different research and non-research issues. During his short stay in Kelowna, Dr. Peter Ott from Heilbronn University has tremendously motivated me through his excellent work ethic.

I am grateful to Brad Armstrong for assisting me in many ways and especially for getting me a quiet study room. Special thanks and appreciation to my friends in Kelowna, who made me feel at home despite being 8000 miles away from home.

Finally, it is my parents, in-laws and family members who have worked behind the scene to always keep me motivated to go ahead. It will be futile to give simply thanks to them. Without the love, care and patience of my parents, wife and kids I would not have been able to do what I have done.

Dedication

To four caring ladies: my mother, wife, daughter and sister

Chapter 1

Introduction

This thesis examines the interaction between electromagnetic waves and a small aperture in a metallic film. How small is small? We will focus our attention to a regime in which the aperture dimension is comparable to the wavelength of the optical wave, parsing the work into the study of an aperture having sub-wavelength (smaller than the wavelength) and super-wavelength (greater than the wavelength) dimensions. We will also restrict our efforts to understanding and improving the process in which an optical wave incident onto an aperture in a metallic film converts into a surface wave immediately adjacent to the aperture exit. This phenomenon has been gaining greater research attention in recent years because it offers a means to control light on very small size scales and may have potential application in miniaturized light-based devices. To treat this problem, we will develop and propose a basic physical model to describe wave coupling in the vicinity of an aperture in a metallic film, drawing upon approximate scalar diffraction theories and analytical solutions to Maxwell's equations. Predictions made using the physical model will be validated by two independent approaches: first, we will use computer simulations solving Maxwell's equations to model optical wave interaction with apertures in metallic films in various configurations and second, apertures in metallic films will be fabricated over a large parameter range and their optical wave response will be experimentally measured. The result of this thesis work is a robust model of surface wave excitation near small apertures and several experimentally and numerically validated approaches to optimize the efficiency of this excitation mechanism.

1.1 Early work on light diffraction through apertures

Before proceeding further, it is appropriate to describe the rich historical context of this topic and how it has evolved to become a field of modern research. The interaction of light with small apertures is a classical problem,

1.1. Early work on light diffraction through apertures

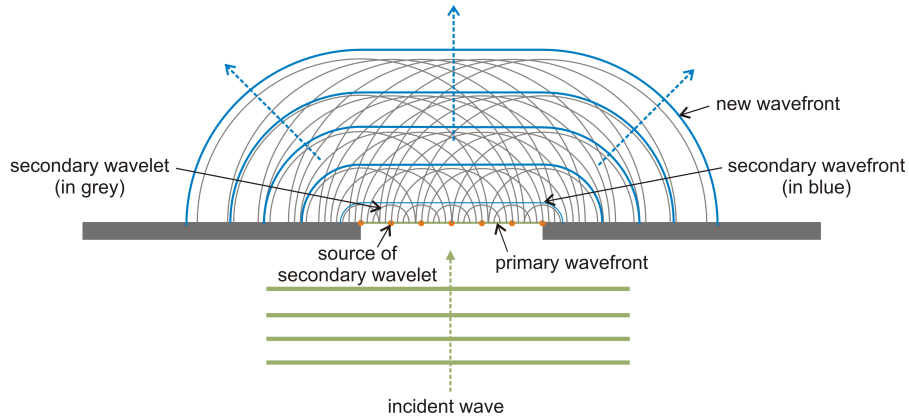


Figure 1.1: Huygens' secondary wavelet analysis of a wavefront passing through an opening in an opaque screen.

spanning several centuries, and has been instrumental to the formation of our current understanding of light. In the 15th century, observations of the blurred edges of a shadow cast by a small pinhole in an opaque screen could not be explained by the predominant corpuscular theory of light championed by Isaac Newton, which predicted that the shadow of a small pinhole would have sharp, well-defined borders due to the purely rectilinear propagation of light particles along well-defined rays. In 1670, Christiaan Huygens proposed an alternative picture viewed light as a collection of spherical waves forming a wavefront. Each point of the wavefront in turn becomes a source of secondary spherical waves which have tangents that collectively form an envelope defining the wavefront at a subsequent time and a farther position. Although this wave picture could explain the spreading shadow cast by a pinhole in terms of the natural spreading of spherical wavelets (refer to Fig. 1.1), it was not widely accepted over the corpuscular theory of light, due in large part to Newton's enormous influence. It was not until 1803 that further evidence of the wave nature of light was provided by Thomas Young, who experimentally showed that light transmitted through two closely spaced slits formed a diffraction pattern consisting of bright and dark fringes. Later, in 1816, Augustin-Jean Fresnel modified Huygens' principle by adding the concept of wave interference. The bright and dark regions of a diffraction pattern due to light transmission through slits could be explained by Huygens-Fresnel theory in terms of the constructive and destructive interference of secondary wavelets emanating from the

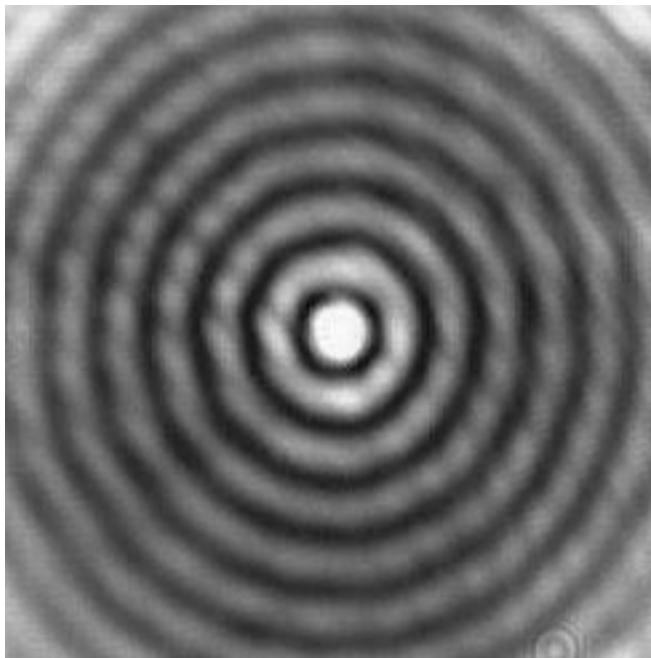


Figure 1.2: Image of the Arago spot in the shadow of a circular obstacle placed in a coherent beam. This image was used with permission from Ref [1].

slits. The theory was initially deemed to be incorrect because it made seemingly strange predictions - for example, it predicted that the center of the shadow of a small circular disk would exhibit a bright spot. However, the theory was later vindicated by the experimental observation of this effect by Dominique-Francois-Jean Arago (and hence named the “Arago spot”). Although Fresnel’s wave theory of light was successful in describing diffraction through apertures, many at the time still supported the corpuscular theory of light. It was not until James Maxwell’s transcendental work on the dynamical equations of the electromagnetic field and the subsequent experimental verification by Heinrich Hertz of electromagnetic wave propagation predicted by Maxwell’s equations that an electromagnetic wave picture of light became fully entrenched in the scientific community.

1.2 Maxwell's equations

Maxwell's equations, published in 1873, are a set of differential equations that relate four vector fields - the displacement field, \vec{D} , the electric field, \vec{E} , the magnetic flux density, \vec{B} , and the magnetic field, \vec{H} - to the presence of sources of fields - the charge density, ρ , and the current density, \vec{J} [2]. The equations are given by

$$\vec{\nabla} \cdot \vec{D}(\vec{r}, t) = \rho, \quad (1.1)$$

$$\vec{\nabla} \cdot \vec{B}(\vec{r}, t) = 0, \quad (1.2)$$

$$\vec{\nabla} \times \vec{E}(\vec{r}, t) = -\frac{\partial \vec{B}(\vec{r}, t)}{\partial t}, \quad (1.3)$$

and

$$\vec{\nabla} \times \vec{H}(\vec{r}, t) = \vec{J}(\vec{r}, t) + \frac{\partial \vec{D}(\vec{r}, t)}{\partial t}, \quad (1.4)$$

where \vec{r} is the position vector and t is the time variable. Since there are six variables and only four equations, Maxwell's equations as written above are not solvable. However, by imposing at least two constitutive relations - independent equations relating the vector fields and sources - it becomes possible to obtain analytical solutions. The most common constitutive relation is that the displacement field \vec{D} and the magnetic flux density \vec{B} are linearly related to the electric field \vec{E} and magnetic field \vec{H} , respectively, giving

$$\vec{D}(\vec{r}, t) = \epsilon_r \epsilon_o \vec{E}(\vec{r}, t), \quad (1.5)$$

and

$$\vec{B}(\vec{r}, t) = \mu_r \mu_o \vec{H}(\vec{r}, t), \quad (1.6)$$

where ϵ_r is the relative electric permittivity, ϵ_o is the free-space permittivity, μ_r is the relative magnetic permeability, and μ_o is the free-space permeability. Since most materials are non-magnetic at optical frequencies, we typically set $\mu_r = 1$. An additional assumption commonly made is that the current density \vec{J} is linearly related to the electric field \vec{E} , resulting in a relation widely known as Ohm's law given by

$$\vec{J}(\vec{r}, t) = \sigma \vec{E}(\vec{r}, t), \quad (1.7)$$

where σ is the electric conductivity. Together, the constitutive relations given by Eqs. 1.5, 1.6, and 1.7, correspond to a medium that is deemed to be linear, isotropic, homogeneous, and instantaneously responsive. To reveal the wave nature of light implicit to Maxwell's equations in such a medium,

1.2. Maxwell's equations

let us first make the assumption that a region is source-free, so that $\rho = 0$ and $\vec{J} = 0$. Maxwell's equations can then be succinctly re-written as

$$\vec{\nabla} \cdot \vec{E}(\vec{r}, t) = 0, \quad (1.8)$$

$$\vec{\nabla} \cdot \vec{H}(\vec{r}, t) = 0, \quad (1.9)$$

$$\vec{\nabla} \times \vec{E}(\vec{r}, t) = -\mu_r \mu_o \frac{\partial \vec{H}(\vec{r}, t)}{\partial t}, \quad (1.10)$$

and

$$\vec{\nabla} \times \vec{H}(\vec{r}, t) = \epsilon_r \epsilon_o \frac{\partial \vec{E}(\vec{r}, t)}{\partial t}. \quad (1.11)$$

The modified Maxwell's equations can be manipulated into the form of wave equations for the electric and magnetic fields. Taking the curl of both sides of Eq. 1.10 and setting $\mu_r = 1$ results in

$$\begin{aligned} \vec{\nabla} \times \vec{\nabla} \times \vec{E}(\vec{r}, t) &= \vec{\nabla} \times \left(-\mu_o \frac{\partial \vec{H}(\vec{r}, t)}{\partial t} \right) \\ &= -\mu_o \frac{\partial}{\partial t} (\vec{\nabla} \times \vec{H}(\vec{r}, t)). \end{aligned} \quad (1.12)$$

Using Eqs. 1.5 and 1.11, Eq. 1.12 simplifies to

$$\begin{aligned} \vec{\nabla} \times \vec{\nabla} \times \vec{E}(\vec{r}, t) &= -\mu_o \frac{\partial^2 \vec{D}(\vec{r}, t)}{\partial t^2} \\ &= -\mu_o \epsilon_o \epsilon_r \frac{\partial^2 \vec{E}(\vec{r}, t)}{\partial t^2}. \end{aligned} \quad (1.13)$$

The left side of Eq. 1.13 can be written as

$$\vec{\nabla} \times \vec{\nabla} \times \vec{E}(\vec{r}, t) = \vec{\nabla}(\vec{\nabla} \cdot \vec{E}(\vec{r}, t)) - \vec{\nabla}^2 \vec{E}(\vec{r}, t), \quad (1.14)$$

which, in a source-free region, simplifies to

$$\vec{\nabla} \times \vec{\nabla} \times \vec{E}(\vec{r}, t) = -\vec{\nabla}^2 \vec{E}(\vec{r}, t). \quad (1.15)$$

Combining Eq. 1.13 and Eq. 1.15, we get

$$\vec{\nabla}^2 \vec{E}(\vec{r}, t) - \mu_o \epsilon_o \epsilon_r \frac{\partial^2 \vec{E}(\vec{r}, t)}{\partial t^2} = 0. \quad (1.16)$$

By defining the speed of light through the free-space permittivity and permeability as

$$c = \frac{1}{\sqrt{\mu_o \epsilon_o}}, \quad (1.17)$$

we arrive at a wave equation describing the electric field

$$\vec{\nabla}^2 \vec{E}(\vec{r}, t) - \frac{\epsilon_r}{c^2} \frac{\partial^2 \vec{E}(\vec{r}, t)}{\partial t^2} = 0, \quad (1.18)$$

which is also known as the *Helmholtz wave equation*. A similar treatment can be applied to yield a wave equation for the magnetic field, given by

$$\vec{\nabla}^2 \vec{H}(\vec{r}, t) - \frac{\epsilon_r}{c^2} \frac{\partial^2 \vec{H}(\vec{r}, t)}{\partial t^2} = 0. \quad (1.19)$$

Thus, Maxwell's equations introduced the revolutionary concept that light propagates as a vector wave for both the electric and magnetic fields. While this theory was initially met with resistance, the experimental verification of the existence of electromagnetic waves at microwave frequencies by Heinrich Hertz in 1888, and the countless experimental observations of electromagnetic wave phenomena since have conclusively proved the validity and veracity of Maxwell's theory.

1.3 Kirchhoff's scalar diffraction theory

With the establishment of Maxwell's equations, there was sufficient mathematical theory to tackle the problem of light diffraction through an aperture. The first major contribution after the advent of Maxwell's equations was provided by Gustav Kirchhoff, who in 1882, introduced scalar diffraction theory to accurately model the physical diffraction principles put forth by Huygens and Fresnel. Although scalar diffraction theory makes several assumptions (which will be discussed here) that in fact make it an invalid solution to Maxwell's equations, it has been highly influential due to its predictive powers and simplicity of use. To this day, introductory optics textbooks use Kirchhoff's scalar theory to derive the well-known Fraunhofer and Fresnel descriptions of light diffraction in the far- and near-field, respectively. Due to the importance of scalar diffraction theory in modern optics and its use in this thesis, we will detail its foundation, its critical assumptions, and various ways in which it has been used to describe light diffraction through an aperture. For interested readers, excellent discussions of scalar diffraction theory are given in the textbooks *Introduction to Fourier Optics* by Joseph Goodman [3] and *Principles of Optics* by Max Born and Emil Wolf [4].

The starting point of scalar diffraction theory is the postulation of a governing wave equation to solve. In contrast to the vector electric and

1.4. Helmholtz-Kirchhoff integral equation for scalar diffraction

magnetic wave equations shown above to be derivable from Maxwell's equations, scalar diffraction theory assumes that the electric and magnetic fields can be treated as scalar quantities which obey a scalar wave equation

$$\nabla^2 - \frac{1}{c^2} \frac{\partial^2 \underline{u}(\vec{r}, t)}{\partial t^2} = 0. \quad (1.20)$$

where $\underline{u}(\vec{r}, t)$ is a scalar function representing either the electric or magnetic field in free-space propagating at the speed of light. Equation 1.20 ignores the vectorial coupling between the electric and magnetic fields, as described by Maxwell's equations, which is a valid assumption in an isotropic and homogeneous medium, but is not valid near boundaries. Nonetheless, let's proceed with this line of thought and explore its implications.

To analytically solve the scalar wave equation, let's assume that the function \underline{u} describes a monochromatic wave

$$\underline{u}(\vec{r}, t) = \underline{U}(\vec{r})e^{-i\omega t}, \quad (1.21)$$

where \underline{U} is the amplitude and ω is the frequency (the position and time dependences will be dropped in subsequent discussions for brevity). Substitution of this candidate solution into the scalar wave equation yields the time-independent Helmholtz equation expressed as

$$(\nabla^2 + k^2)\underline{U} = 0, \quad (1.22)$$

where k is the wave number given by $k = 2\pi\omega/c = 2\pi/\lambda_0$ and λ_0 is the free-space wavelength.

1.4 Helmholtz-Kirchhoff integral equation for scalar diffraction

The Huygens-Fresnel theory postulated that light diffraction can be viewed as the superposition of the secondary waves emanating from a surface. Kirchhoff made this picture mathematically rigorous, demonstrating that the Huygens-Fresnel concept was an approximation to an integral solution to the Helmholtz equation. This integral solution, derived from Green's theorem, enabled the field at an arbitrary point to be expressed in terms of the value of the solution, and its first derivative, at points on a surface enclosing that point. Thus, Kirchhoff transformed the physical wave-based picture of diffraction into a mathematical solution of the wave equation solvable by imposing appropriate boundary conditions.

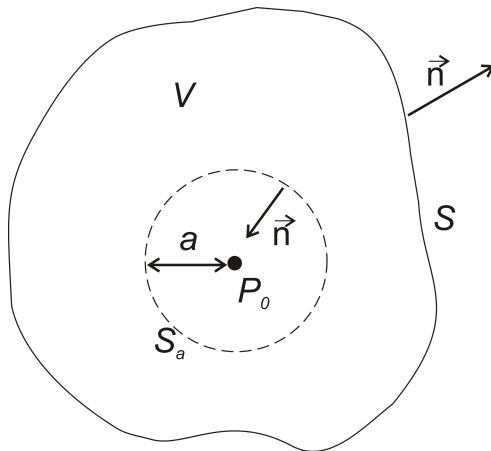


Figure 1.3: Theoretical construct consisting of a closed surface S associated with a volume V and surrounding an observation point P_0 used to illustrate Green's theorem. Note that we take the normal direction to correspond to the outward normal.

Assume that we have a closed surface S surrounding a volume V and enclosing an observation point P_0 (this is where we would like to calculate the field \underline{U}). Let \underline{U} , which represents either the electric or magnetic scalar field, be a complex-valued scalar function that has single-valued first and second partial derivatives continuous within and on S . If another complex-valued scalar function \underline{G} satisfies the same continuity conditions imposed on \underline{U} , then the scalar Green's theorem provides a relationship between the two scalar functions given by

$$\iiint_V (\underline{G}\nabla^2\underline{U} - \underline{U}\nabla^2\underline{G}) dV = \iint_S \left(\underline{G}\frac{\partial\underline{U}}{\partial n} - \underline{U}\frac{\partial\underline{G}}{\partial n} \right) dS, \quad (1.23)$$

where the partial derivatives with respect to n are differentials in the direction of the outward surface normal (consistent with mathematical convention but opposite to the discussion in *Principles of Optics* by Max Born and Emil Wolf [4]). If the function \underline{G} is chosen so that it also satisfies the time-independent scalar wave equation

$$(\nabla^2 + k^2)\underline{G} = 0, \quad (1.24)$$

then the volume integrals on the left-hand side of Eq. 1.23 disappear and

1.4. Helmholtz-Kirchhoff integral equation for scalar diffraction

we are left with

$$\iint_S \left(\underline{G} \frac{\partial U}{\partial n} - U \frac{\partial \underline{G}}{\partial n} \right) ds = 0. \quad (1.25)$$

The question then becomes: what function should we select for \underline{G} ? Originally, Kirchhoff was inspired by the spherical wave picture of Huygens and Fresnel and chose the function \underline{G} to represent a scalar spherical wave emanating from the observation point given by

$$\underline{G} = \frac{e^{iks}}{s}, \quad (1.26)$$

where s represents the distance from the observation point to any arbitrary position (it can be easily checked that this particular \underline{G} satisfies the time-independent Helmholtz equation in spherical coordinates for $s > 0$). A spherical wave seems to be a reasonable choice, except that it has a singularity at $s = 0$ and Green's theorem requires that \underline{G} be continuous and differentiable both within and on S . Therefore, to exclude the discontinuity at P_0 , a small spherical surface S_a of radius a , is inserted about the point P_0 . Green's theorem is then applied over the surfaces S and S_a

$$\iint_S \left\{ \frac{e^{iks}}{s} \frac{\partial U}{\partial n} - U \frac{\partial}{\partial n} \left(\frac{e^{iks}}{s} \right) \right\} ds + \iint_{S_a} \left\{ \frac{e^{iks}}{s} \frac{\partial U}{\partial n} - U \frac{\partial}{\partial n} \left(\frac{e^{iks}}{s} \right) \right\} ds = 0. \quad (1.27)$$

To further simplify this expression, we can develop the normal derivative of \underline{G} in the direction of s assuming a spherical coordinate system centered at P_0 ,

$$\frac{\partial}{\partial s} \left(\frac{e^{iks}}{s} \right) = \frac{e^{iks}}{s} \left(ik - \frac{1}{s} \right). \quad (1.28)$$

Substituting Eq. 1.28 into Eq. 1.27 and evaluation of the surface integral on S_a in a spherical coordinate system yields

$$\begin{aligned} & \iint_S \left\{ \frac{e^{iks}}{s} \frac{\partial U}{\partial n} - U \frac{\partial}{\partial n} \left(\frac{e^{iks}}{s} \right) \right\} ds \\ &= - \iint_{S_a} \left\{ \frac{e^{iks}}{s} \frac{\partial U}{\partial n} - U \frac{e^{iks}}{s} \left(ik - \frac{1}{s} \right) \right\} ds \\ &= - \iint_{S_a} \left\{ \frac{e^{ika}}{a} \frac{\partial U}{\partial n} - U \frac{e^{ika}}{a} \left(ik - \frac{1}{a} \right) \right\} a^2 d\Omega, \end{aligned} \quad (1.29)$$

where $d\Omega$ denotes the solid angle. If we allow the radius a to shrink to zero, all the terms on the right hand side of Eq. 1.29 go to zero except for the last

one, which equals $4\pi\underline{U}$. We can then re-arrange the equation in terms of \underline{U} as

$$\underline{U} = \frac{1}{4\pi} \iint_S \left\{ \frac{e^{iks}}{s} \frac{\partial \underline{U}}{\partial n} - \underline{U} \frac{\partial}{\partial n} \left(\frac{e^{iks}}{s} \right) \right\} ds, \quad (1.30)$$

which expresses the value of \underline{U} at an observation point P_0 in terms of the values of \underline{U} , and its derivative on a surface bounding P_0 . This elegant solution is known as the integral theorem of Helmholtz and Kirchhoff.

1.5 Kirchhoff's formulation of scalar diffraction by a plane screen

We are now in position to apply scalar diffraction theory to the problem of light diffraction from an aperture in an opaque planar screen. Let's consider a monochromatic spherical wave disturbance from a point source located at the origin O which is situated on one side of an opening in an opaque screen. We will let P_0 as before represent a point located on the other side of the opening where we want to determine the value of the scalar disturbance. With the help of the integral theorem, we can now find the value of the disturbance at P_0 by carefully selecting an appropriate surface to surround that point. Let's take a surface on the exit side of the screen, as shown in Fig. 1.4, which consists of a planar section S_1 covering the opening, another planar section S_2 covering the screen, and a third circular section S_3 with a radius R that is centered on P_0 . The Helmholtz-Kirchhoff integral theorem, applied over this closed surface, takes the form

$$\underline{U} = \frac{1}{4\pi} \left[\iint_{S_1} + \iint_{S_2} + \iint_{S_3} \right] \left\{ \frac{e^{iks}}{s} \frac{\partial \underline{U}}{\partial n} - \underline{U} \frac{\partial}{\partial n} \left(\frac{e^{iks}}{s} \right) \right\} ds, \quad (1.31)$$

where s is the distance from P_0 to an element on the surface. At this point, we need to make some assumptions to make the integral solvable. Let's first assume that the field and its derivative over the section S_2 are both approximately zero since every point on S_2 lies in the geometric shadow of the opaque screen. It could also be reasoned that if we make the radius R sufficiently large, the contributions to the surface integral over S_3 diminish to zero. We are then left with just a surface integral term applied over the opening S_1 . At the opening, we assume that the field is everywhere the same as if the screen were not present, which would then take the form of a spherical wave emanating from the origin

$$\underline{U}_{S_1} = \frac{Ae^{ikr}}{r}, \quad (1.32)$$

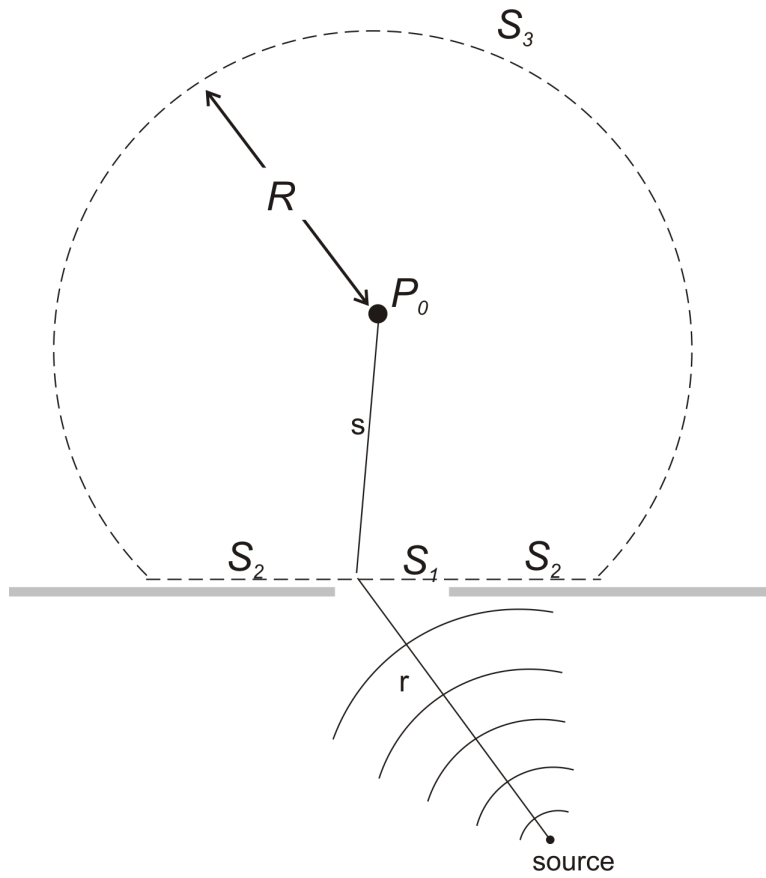


Figure 1.4: Application of the Helmholtz-Kirchhoff integral theorem to solve for the scalar disturbance at an observation point P_0 when an opaque screen with an opening is placed between a source and the observation point.

where A is a constant and r is the distance from the origin to an arbitrary point on the surface S_1 . This assumption is perhaps approximately true near the center of the opening but is questionable near the edges of the opening. We therefore restrict the size of the aperture to be greater than the wavelength in order to limit the relative contributions of fringing fields near the aperture edge. Altogether, these assumptions of the field and its derivative at the boundaries of the surface are known as *Kirchhoff's boundary conditions*. If we insert Eq. 1.32 into Eq. 1.31 and develop the derivatives, dropping terms that are second order in r and s (this implicitly assumes that the source and observation points are at distances from the aperture much larger than the wavelength), we arrive at the solution

$$\underline{U}(P_0) = -\frac{iA}{2\lambda_0} \iint_{S_1} \frac{e^{ik(r+s)}}{rs} \{\cos(n, s) - \cos(n, r)\} ds, \quad (1.33)$$

where $\cos(n, s)$ and $\cos(n, r)$ denote the cosines of the angles between the outward normal and the position vectors corresponding to s and r , respectively. This solution is known as the Fresnel-Kirchhoff diffraction formula, an approximate mathematical description of the transmission through an aperture in an opaque screen requiring that the dimension of the aperture exceed the wavelength (so that it does not strongly perturb the field exiting the aperture) and that the source and observation points are spaced from the aperture at distances that are much greater than the wavelength.

1.6 Fraunhofer diffraction and the Fourier transform

The Fresnel-Kirchhoff formula relates the scalar disturbance at a particular point due to the presence of an opening in an opaque screen placed between that point and a source of the disturbance. We can further simplify the expression by making two assumptions: first, the distance between the aperture to the source and observation points are much larger than the dimensions of the aperture (so far, they are only required to be much larger than the wavelength) and second, the source and observation points are nearly aligned (paraxial) to a line that intersects the center of the aperture and is normal to the plane of the screen. For convenience, we will also now shift the origin so that it coincides with the center of the aperture (labeled O') and align the $x'y'$ plane centered at O' to the plane of the screen and have the z' axis pointing into the observation half space, as shown in Fig. 1.5.

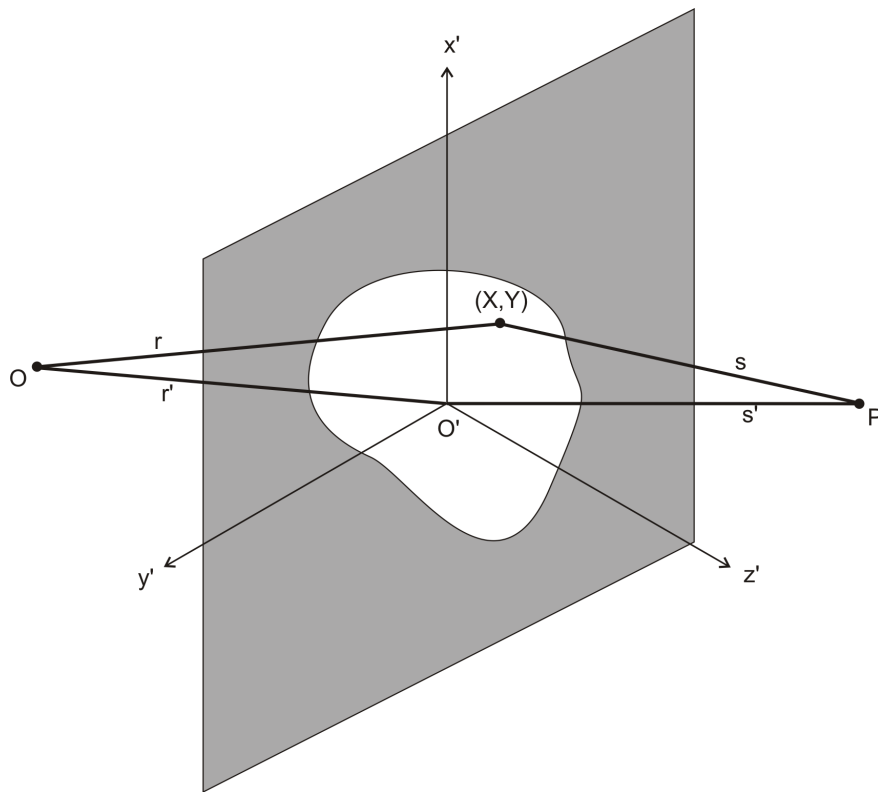


Figure 1.5: Configuration used to analyze scalar diffraction from an opening in an opaque screen.

1.6. Fraunhofer diffraction and the Fourier transform

To simplify the Fresnel-Kirchhoff formula in this configuration, let's carefully examine the terms in the integrand of Eq. 1.34 and see how each term varies with respect to the opening of the aperture. Since the aperture is large compared to the wavelength, the term $e^{ik(r+s)}$ varies over many cycles as we scan over the area of the aperture and must be left inside the integrand. On the other hand, the source and observation points are far from the aperture, meaning that the term $\cos(n, s) - \cos(n, r)$ does not vary appreciably over the area of the aperture. We can therefore replace the term $\cos(n, s) - \cos(n, r)$ by $-2\cos(\delta)$, where δ is the angle between the line connecting the source and observation points and the normal to the aperture, and take this factor outside of the integrand (note that for normal incidence illumination and observation, this factor becomes unity). If we also take the variables r and s - referenced with respect to an arbitrary position within the aperture - and replace them with r' and s' - referenced to the center of the aperture located at O' - we arrive at a simplified version of the Fresnel-Kirchhoff formula given by

$$\underline{U}(P_0) \simeq \frac{iA \cos(\delta)}{\lambda_0 r' s'} \iint_{S_1} e^{ik(r+s)} ds. \quad (1.34)$$

If we let (x'_0, y'_0, z'_0) and (x'_1, y'_1, z'_1) represent the coordinates of the source and observation points, respectively, with respect to O' and (X, Y) the coordinate at a point in the plane of the aperture, we have the geometrical relations

$$\begin{aligned} r^2 &= (x'_0 - X)^2 + (y'_0 - Y)^2 + z_0'^2 \\ s^2 &= (x'_1 - X)^2 + (y'_1 - Y)^2 + z_1'^2 \\ r'^2 &= x_0'^2 + y_0'^2 + z_0'^2 \\ s'^2 &= x_1'^2 + y_1'^2 + z_1'^2. \end{aligned} \quad (1.35)$$

These relations can be combined to yield

$$\begin{aligned} r^2 &= r'^2 - 2(x_0 X + y_0 Y) + X^2 + Y^2 \\ s^2 &= s'^2 - 2(x_1 X + y_1 Y) + X^2 + Y^2. \end{aligned} \quad (1.36)$$

Assuming that r' and s' are both much larger than the dimensions of the aperture, we can expand both r and s as power series in X/r' , Y/r' , X/s' , and Y/s' to yield

$$\begin{aligned} r &\simeq r' - \frac{x'_0 X + y'_0 Y}{r'} + \frac{X^2 + Y^2}{2r'^3} + \dots \\ s &\simeq s' - \frac{x'_1 X + y'_1 Y}{s'} + \frac{X^2 + Y^2}{2s'^3} + \dots \end{aligned} \quad (1.37)$$

The expressions in Eq. 1.37 can now be inserted into the exponential factor in Eq. 1.34 and be evaluated up to an arbitrary order in X and Y . When carried out to just the first order of X and Y , the integral describes Fraunhofer diffraction that is valid when the source and observation points are located at distances that are much larger than the aperture dimension. When the higher order terms are included, the integral describes Fresnel diffraction applicable when the source and observation points are located at distances comparable to or less than the aperture dimension.

The integral expression describing Fraunhofer diffraction (that is, keeping only terms to the first order of X and Y in the exponential factor in Eq. 1.34) can be cast into a form that is identical to the familiar Fourier transform if we allow the source to be located infinitely far away from the aperture (so that the aperture is illuminated by essentially a plane wave). Lumping all the constant factors into a common constant C and denoting the differential element as $ds = dXdY$, the disturbance at the observation point is proportional to

$$\underline{U}(P_0) \simeq C \iint_{S_1} e^{-ik(X+Y)/s'} dXdY, \quad (1.38)$$

which is, within a constant factor, the two-dimensional Fourier transform of the aperture function evaluated at spatial frequencies $\kappa_x = kX/s'$ and $\kappa_y = kY/s'$. Due to the imposition of Kirchhoff's boundary conditions and the assumption of plane-wave illumination, the aperture function in this case is a piecewise function that is unity over the aperture opening and zero everywhere else. In general, this aperture function can be any two-dimensional function.

1.7 Bethe's vectorial diffraction theory

Kirchhoff's scalar diffraction theory was limited because, fundamentally, it did not account for the vector nature of light as postulated in Maxwell's equations and could only be applied to describe diffraction through an aperture that was larger than the wavelength. In 1944, Hans Bethe [5] introduced a new theoretical formalism to describe diffraction through small holes (smaller than the wavelength) by solving Maxwell's equations in its full vector form. Bethe considered a sub-wavelength circular hole of radius a in a perfectly conducting, opaque and negligibly thick metal film and derived a complete solution that satisfied continuity conditions at the boundaries everywhere. His analysis made only two assumptions: the hole was small so

that retardation can be neglected in the aperture and the incident field was uniform over the opening of the hole. The famous result obtained by Bethe was that the transmitted power of light, P_{tr} , through a sub-wavelength hole is given by

$$P_{tr} = \frac{64}{27\pi} k^4 a^6 S_i, \quad (1.39)$$

where k is the wave number and S_i is the incident flux per unit of area, which can be written in terms of the incident electric field E_i as $S_i = c\epsilon_o E_i^2/2$. Due to the simplicity of the final result and its consistency with Maxwell's equations, Bethe's solution has been widely accepted and used as a theoretical benchmark (see, for example, Refs. [6–8] in which Bethe's formula is used as a standard against which experimental and simulation data on aperture transmission are compared).

1.8 Scalar wave equation for two-dimensional problems

A common critique of Kirchhoff's theory was that it solved the scalar wave equation, as opposed to the vector wave equation predicted by Maxwell's equations. Although this restricts the generality of Kirchhoff's theory, it is by no means a fatal flaw, since Maxwell's equations can condense into the scalar wave equation for a large number of electromagnetic problems, such as those which are fundamentally one- or two-dimensional in nature. Consider, for example, the case of a two-dimensional electromagnetic problem that is independent of the y coordinate. Assuming monochromatic complex electric and magnetic fields both proportional to $e^{-i\omega t}$, two of Maxwell's equations in free-space can be developed into the form

$$\vec{\nabla} \times \underline{H} = -ik\underline{E}, \quad (1.40)$$

and

$$\vec{\nabla} \times \underline{E} = ik\underline{H}, \quad (1.41)$$

where the relation $k = \omega/c$ has been used. If we develop the spatial derivatives and take all partial derivatives with respect to y to be zero, there are two independent sets of equations; one involving only \underline{E}_y , \underline{H}_x , and \underline{H}_z , and another involving only \underline{H}_y , \underline{E}_x , and \underline{E}_z . Because we can break an arbitrary solution into a linear combination of two solutions obtained by setting every component of each set, in turn, to zero, we can introduce two types of fields

obeying either

$$\begin{aligned}
 \underline{E}_x &= \underline{E}_z = \underline{H}_y = 0 \\
 -\frac{\partial \underline{H}_z}{\partial x} + \frac{\partial \underline{H}_x}{\partial z} &= -ik\underline{E}_y \\
 -\frac{\partial \underline{E}_y}{\partial z} &= ik\underline{H}_x \\
 \frac{\partial \underline{E}_y}{\partial x} &= ik\underline{H}_z
 \end{aligned} \tag{1.42}$$

or

$$\begin{aligned}
 \underline{H}_x &= \underline{H}_z = \underline{E}_y = 0 \\
 -\frac{\partial \underline{E}_z}{\partial x} + \frac{\partial \underline{E}_x}{\partial z} &= ik\underline{H}_y \\
 -\frac{\partial \underline{H}_y}{\partial z} &= -ik\underline{E}_x \\
 \frac{\partial \underline{H}_y}{\partial x} &= -ik\underline{E}_z.
 \end{aligned} \tag{1.43}$$

Alignment of the electric or magnetic field along the coordinate of independence can be used to classify the sets. We denote the set with non-zero \underline{E}_y as describing transverse-electric (TE) polarization and the set with non-zero \underline{H}_y as describing transverse-magnetic (TM) polarization. For transverse-electric polarization, combination of the equations in 1.42 yields a scalar wave equation completely in terms of \underline{E}_y , given by

$$\frac{\partial^2 \underline{E}_y}{\partial x^2} + \frac{\partial^2 \underline{E}_y}{\partial z^2} + k^2 \underline{E}_y = 0. \tag{1.44}$$

Similarly, combination of the equations in 1.43 yields a scalar wave equation completely in terms of \underline{H}_y , given by

$$\frac{\partial^2 \underline{H}_y}{\partial x^2} + \frac{\partial^2 \underline{H}_y}{\partial z^2} + k^2 \underline{H}_y = 0. \tag{1.45}$$

1.9 Angular spectrum representation

Given the scalar wave equations applicable to electromagnetic fields propagating in a two-dimensional plane, it becomes possible to introduce the powerful *angular spectrum representation* method to obtain and interpret solutions. Given the two-dimensional scalar wave equation

$$\frac{\partial^2 \underline{u}}{\partial x^2} + \frac{\partial^2 \underline{u}}{\partial z^2} + k^2 \underline{u} = 0, \tag{1.46}$$

1.10. Scalar diffraction through small slits

where \underline{u} represents either the transverse electric or magnetic field component, a fundamental solution takes the form

$$\underline{u} \propto e^{i(k_x x + k_z z)}, \quad (1.47)$$

where k_x and k_z are the spatial frequencies along the x and z directions, respectively, and constrained by the condition

$$k^2 = k_x^2 + k_z^2. \quad (1.48)$$

Let's now consider the complex field along the line $z = 0$. We know that any solution $\underline{u}(x, 0)$ can be represented as a linear combination of the fundamental solutions

$$\underline{u}(x, 0) = \int_{-\infty}^{+\infty} \underline{f}(k_x) e^{ik_x x} dk_x, \quad (1.49)$$

where $\underline{f}(k_x)$ is a function describing the spatial harmonic weighting in $\underline{u}(x, 0)$ and can be directly calculated through the one-dimensional Fourier transform of $\underline{u}(x, 0)$,

$$\underline{f}(k_x) = \int_{-\infty}^{+\infty} \underline{u}(x, 0) e^{-ik_x x} dx. \quad (1.50)$$

Here, we have chosen the $z = 0$ line out of convenience. In general, for an electromagnetic field confined to a two-dimensional plane, the field disturbance (described by the field component orthogonal to the plane) along any line in that plane can be decomposed into its spatial harmonics by the Fourier transformation along that line, providing a powerful method to analyze and interpret field distributions.

1.10 Scalar diffraction through small slits

The angular spectrum representation of two-dimensional fields was used by Marek Kowarz, a student of Emil Wolf, to analyze near-field diffraction from a small slit in an opaque screen [9]. As shown in Fig. 1.6, the slit geometry considered by Kowarz extends infinitely along one coordinate (the y coordinate), and is thus, a two-dimensional electromagnetic problem. Diffraction of a plane wave through the slit opening can be treated by first postulating the form of the fields at the exit of the slit located in the plane $z = 0$. For simplicity, Kowarz assumed a top-hat profile of the fields at the slit exit given by a constant value over the slit opening and zero everywhere

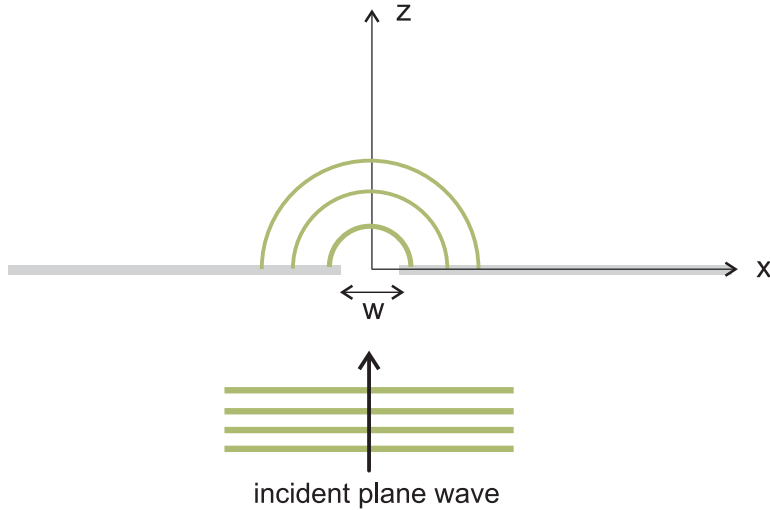


Figure 1.6: Configuration considered by Kowarz to analyze near-field diffraction from a slit.

else. The spatial harmonic distribution at the exit of the slit can then be deduced by taking the one-dimensional Fourier transform of the assumed field at the slit exit. Interestingly, Kowarz parsed the fields into two categories: a homogeneous contribution, in which k_x is less than the free-space wave vector (describing a propagating plane wave), and an inhomogeneous contribution in which k_x is greater than the free-space wave vector (describing an exponentially decaying evanescent wave). It was shown that when the slit width approached sub-wavelength dimensions, the near-field diffraction pattern at the exit of the slit is dominated by inhomogeneous wave components. We will refer to this simple and elegant depiction of the slit scattering problem in the subsequent sections of this thesis.

1.11 Computational solvers for Maxwell's equations

With the availability of abundant computing power, numerical simulators based on Maxwell's equations have become increasingly popular and widely used. The basic idea is to define a region of space in terms of a grid, place a source disturbance in the simulation space, implement appropriate boundary conditions, and then solve for the electric and magnetic fields over

the grid. This can be done in terms of real-valued fields that are solved in the time-domain or complex-valued fields that are solved in the frequency-domain. The former can be achieved using the finite-difference time-domain (FDTD) method [10–14], while the latter can be achieved using the finite-difference frequency-domain (FDFD) method [15, 16]. Numerical solvers like FDTD and FDFD are popular due to their versatility and ability to accurately model the electromagnetic response of structures with complicated geometries. Here, we will briefly go over some of the salient features of these solvers, as they will both be used in the thesis work.

1.11.1 Finite-difference time-domain method

The finite-difference time-domain (FDTD) technique solves the time-domain, instantaneous form of Maxwell's curl equations as written in Eqns. 1.3 and 1.4 [17]. The temporal and spatial partial derivatives in Maxwell's equations are discretized into difference equations using the central-difference approximation and implemented over a special type of spatial grid (that is either one-, two-, or three-dimensional) known as the Yee grid [18] (Figure 1.7). When solving for the fields over a finite geometry, it is common to place a reflection-less absorber [19, 20], known as a perfectly-matched layer (PML), around the simulation space to prevent unphysical back reflections into the simulation space. At a particular time step, the difference equations are solved for each grid point to determine the local amplitude of the field components at a particular moment in time. The grid resolutions must be sufficiently fine to accurately portray the electromagnetic fields. In practice, the grid spacing is commonly $\lambda_{min}/10$ to $\lambda_{min}/40$, where λ_{min} is the wavelength inside the highest refractive index found in the simulation space. Because the fields must be solved for all points in space and at every moment in time, FDTD simulations - especially those that are two- and three-dimensional - are known to be slow and time-consuming. It is important to note that since FDTD is a time-domain simulator, all constitutive parameters must be real and positive. Therefore, to simulate the response of materials known to have negative real parts of their permittivity (such as metals), a Drude constitutive relation is used, which will be discussed in the Appendix. Interested readers can find a comprehensive discussion on the FDTD method in the textbook *Computational Electrodynamics: The Finite-Difference Time-Domain Method* by Allen Taflov and Susan Hagness [21].

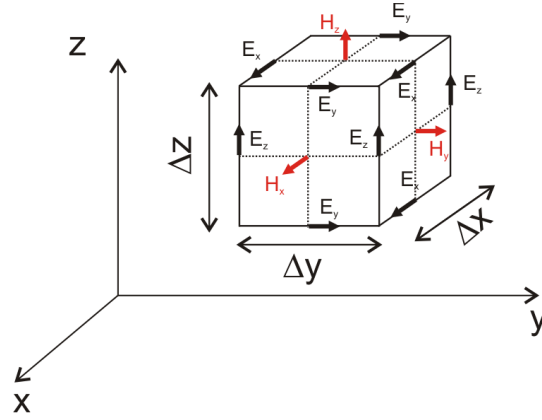


Figure 1.7: Three-dimensional Yee Grid depicting the electric and magnetic field components distributed over a discrete spatial grid.

1.11.2 Finite-difference frequency-domain method

The finite-difference frequency-domain (FDFD) technique solves the frequency-domain, harmonic form of Maxwell's curl equations. Assuming harmonic dependence in the complex fields $\underline{\vec{E}}$, $\underline{\vec{D}}$, $\underline{\vec{H}}$, and $\underline{\vec{B}}$, Maxwell's curl equations can be re-written as

$$\vec{\nabla} \times \underline{\vec{E}} = i\omega \underline{\vec{B}}, \quad (1.51)$$

and

$$\vec{\nabla} \times \underline{\vec{H}} = i\omega \underline{\vec{D}}, \quad (1.52)$$

where, in a linear medium, $\underline{\vec{D}}$ and $\underline{\vec{E}}$ are related by a complex permittivity $\underline{\epsilon}$ and $\underline{\vec{B}}$ and $\underline{\vec{H}}$ are related by a complex permeability $\underline{\mu}$. The advantage of FDFD over FDTD is that it can obtain solutions at a single frequency with greater efficiency [22] and the constitutive parameters are permitted to be any complex value. The basic implementation is similar to FDTD - a spatial grid is defined, a source is placed in the simulation space, boundary conditions are defined, and the fields are solved everywhere. Unlike the FDTD method, where the fields are obtained dynamically by iterating through time, the FDFD method obtains the steady-state distribution of the fields.

1.11.3 Application of FDTD and FDFD to model light transmission through a slit

Here, we will briefly demonstrate the power of FDTD and FDFD solvers for modeling the scattering of light through apertures. We select the geometry of a slit in a metallic film immersed in a dielectric (refractive index $n = 1.5$, as shown in Figure 1.8), a simple two-dimensional configuration which will be the focus of this thesis. The metal is Ag and its constitutive parameters have been fitted to values obtained in the literature. The slit is illuminated from below with a TM-polarized wave with a broad Gaussian profile. The width of the slit is 100 nm and the incident wavelength is 632.8 nm. A perfectly-matched layer is placed around the perimeter of the simulation space and the grid resolution is 1 nm. Figures 1.8 (b) and (c) depict the steady-state magnetic field distribution obtained from FDFD and FDTD, respectively, about the slit after illumination. Not surprisingly, the solvers illustrate similar field features - a highly confined electromagnetic mode within the slit, a quasi-cylindrical wave emanating from the slit exit, and a slight field enhancement on the film surface at the exit side of the slit (signatures of a surface electromagnetic wave that will be studied extensively here). Slight differences in the field distributions at the entrance side of the metal film are due to the inherent difference between the steady-state field profile visualized by FDFD, and the chosen instantaneous snap-shot of the field profile visualized by FDTD. Although the solvers are powerful because they completely solve Maxwell's equations without approximations (outside of linearity of the media), it should be warned that they provide very little physical insight and are time-consuming in that one simulation solves for just a single data point (as opposed to an analytical description written in terms of continuous variables). Nonetheless, they will provide a useful tool that will be used extensively in subsequent chapters.

1.12 Recent research interest in light transmission through aperture in metallic films

In 1998, Thomas Ebbesen and his colleagues [23, 24] demonstrated experimentally that an array of small holes in a metallic film could exhibit normal-incidence transmission several orders of magnitude greater than that predicted by Bethe's theory applied to the hole array. This report was shocking at the time because it dramatically contradicted Bethe's theory and

1.12. *Recent research interest in light transmission through aperture in metallic films*

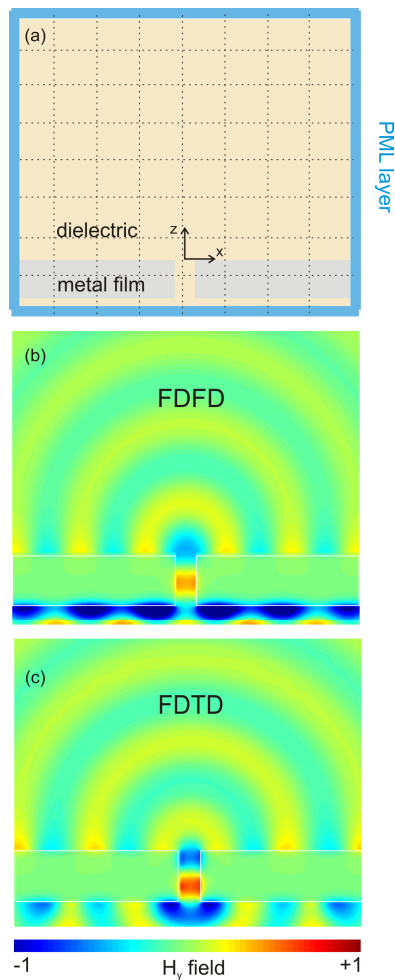


Figure 1.8: Application of the FDTD and FDFD method to solve the two-dimensional problem of TM-polarized plane-wave incident onto a slit in a metallic film. Figure (a) shows the schematic of the simulation grid consisting of a metallic film with a small opening, immersed in a dielectric. The simulation space is surrounded by a perfectly matched layer (PML). Figures (b) and (c) show the calculated magnetic field distribution about the aperture obtained using the FDFD and FDTD method, respectively.

suggested that light could “squeeze” through sub-wavelength openings with great efficiency. At the time, the enhancement was loosely attributed to the presence of surface plasmon polaritons (SPPs) excited on the metal film [25–29], a type of surface electromagnetic wave that was not considered in either Kirchhoff’s scalar diffraction theory or Bethe’s electromagnetic vector-field model, but a detailed physical picture was absent.

In subsequent years after the work of Ebbesen and colleagues, the role of SPPs in the enhanced transmission was confirmed and a clearer picture of the enhancement mechanism emerged. Using a simpler grating structure consisting of an array of slits in an optically thick film, Porto et al. [25] used the transfer matrix method to solve Maxwell’s equations in the vicinity of the slits and show that the excitation of SPPs on both the entrance and exit surfaces of the film and presence of wave guide resonances within the slits were the key factors responsible for the anomalously high optical transmission. It should be noted that a critical assumption of this model is that the slit sustains only its fundamental mode - a common approximation known as the single-mode approximation - which is valid as long as the wavelength of incident light is much greater than the width of the opening. The vital role of SPPs in the transmission enhancement through hole arrays - in addition other aperture systems, such as slit arrays, single holes, and single slits - was later confirmed by other numerical and experimental works [11, 14, 16, 30–38]. From these works, an approximate physical picture crystallized. When TM-polarized electromagnetic waves are incident onto a sub-wavelength aperture in a metallic film, SPPs are excited near the vicinity of the aperture. Due to the confined nature of SPPs (which will be described in the next section), they funnel electromagnetic energy through the aperture. When the SPPs arrive at the exit of the aperture, they scatter and radiate into the far field, resulting in transmission that is enhanced above and beyond what would be expected by Bethe’s formula.

1.13 Surface plasmon polaritons

In this section, we will show that surface plasmon polaritons are a valid solution to Maxwell’s equations, highlight the conditions under which these waves exist for a simple geometry, and derive an expression for the wave vector of SPPs as a function of frequency. Let’s start with the most basic geometry of a semi-infinite medium (“medium 1”) occupying the region $z > 0$ and another semi-infinite medium (“medium 2”) occupying the region $z < 0$, as shown in Fig. 1.9. Both media are non-magnetic. Medium 1 is

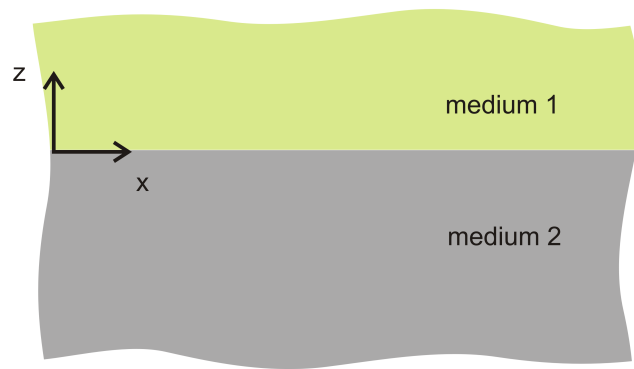


Figure 1.9: A single interface between two disparate media can, under certain conditions, sustain surface waves that obey Maxwell's equations.

1.13. Surface plasmon polaritons

characterized by a local complex relative permittivity ϵ_1 , and medium 2 is characterized by a local complex relative permittivity ϵ_2 . As this geometry is two-dimensional (independent of the y coordinate), we can analyze the wave solutions for TE and TM polarization independently. Let's begin with the case of TM polarization. We assume a general harmonic form of the electromagnetic fields about the interface consisting of a transverse-magnetic (TM) polarized wave propagating along the $+x$ -direction and decaying along the z directions given by

$$\underline{H}_y(z) = \begin{cases} \underline{H}_1 e^{i\mathbf{k}_x x} e^{\mathbf{k}_{z1} z} & z < 0 \\ \underline{H}_2 e^{i\mathbf{k}_x x} e^{-\mathbf{k}_{z2} z} & z > 0, \end{cases} \quad (1.53)$$

$$\underline{E}_x(z) = \begin{cases} -i\mathbf{k}_{z1} \underline{H}_1 e^{i\mathbf{k}_x x} e^{\mathbf{k}_{z1} z} / \omega \epsilon_0 \epsilon_1 & z < 0 \\ i\mathbf{k}_{z2} \underline{H}_2 e^{i\mathbf{k}_x x} e^{-\mathbf{k}_{z2} z} / \omega \epsilon_0 \epsilon_2 & z > 0, \end{cases} \quad (1.54)$$

and

$$\underline{E}_z(z) = \begin{cases} -\mathbf{k}_x \underline{H}_1 e^{i\mathbf{k}_x x} e^{\mathbf{k}_{z1} z} / \omega \epsilon_0 \epsilon_1 & z < 0 \\ -\mathbf{k}_x \underline{H}_2 e^{i\mathbf{k}_x x} e^{-\mathbf{k}_{z2} z} / \omega \epsilon_0 \epsilon_2 & z > 0. \end{cases} \quad (1.55)$$

where \underline{H}_1 and \underline{H}_2 are the complex amplitudes of the magnetic field in media 1 and 2, respectively, \mathbf{k}_x is the complex wave vector component along the x axis, and \mathbf{k}_{z1} and \mathbf{k}_{z2} are the complex wave vector components along the z axis in media 1 and 2, respectively. The allowable modes in the system can be described in terms of either the x or z components of the wave vector, but it is customary to use \mathbf{k}_x because it uniquely defines the mode in both media due to continuity of the fields across the interface. A map of allowable values of \mathbf{k}_x versus frequency is called the dispersion relation of the mode.

To solve for values of \mathbf{k}_x , we impose continuity of the tangential component of the electric and magnetic fields at $z = 0$, yielding

$$\frac{\mathbf{k}_{z1} \underline{H}_1}{\epsilon_1} + \frac{\mathbf{k}_{z2} \underline{H}_2}{\epsilon_2} = 0, \quad (1.56)$$

and

$$\underline{H}_1 - \underline{H}_2 = 0, \quad (1.57)$$

which has a solution only if the determinant is zero

$$\frac{\mathbf{k}_{z1}}{\mathbf{k}_{z2}} = -\frac{\epsilon_1}{\epsilon_2}. \quad (1.58)$$

If \mathbf{k}_{z1} and \mathbf{k}_{z2} are positive (to prevent runaway solutions far away from the interface) and strictly real, the existence of a surface bound wave requires

1.13. Surface plasmon polaritons

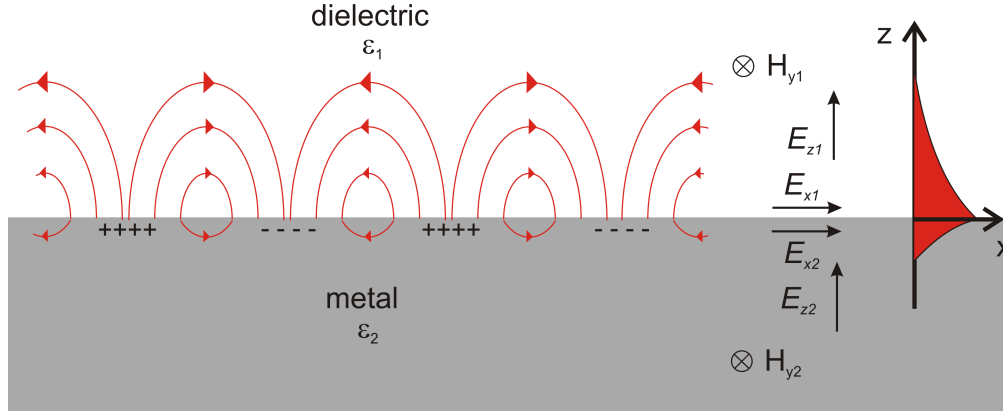


Figure 1.10: Schematic of the TM-polarized electromagnetic waves and surface charges associated with SPPs at the interface of a metal and dielectric.

that the real parts of the permittivities of media 1 and 2 have opposite signs, a condition that can be fulfilled if the interface is between a metal and a dielectric. When this condition is fulfilled, the fields of the SPP wave decay along both directions away from the interface. Typical electromagnetic field and surface charge density distributions associated with a SPP wave at an interface between a metal and dielectric are shown in Fig. 1.13.

A closed form expression for \underline{k}_x can be obtained if we develop the general wave equation in the two media using the postulated forms of the fields given above, resulting in

$$\underline{k}_{z1}^2 = \underline{k}_x^2 - k_0^2 \epsilon_1, \quad (1.59)$$

and

$$\underline{k}_{z2}^2 = \underline{k}_x^2 - k_0^2 \epsilon_2, \quad (1.60)$$

where k_0 is the free-space wave vector. Applying Eqs. 1.59 and 1.60 to Eq. 1.58, we obtain the dispersion relation for a single metal-dielectric interface

$$\underline{k}_x = k_0 \sqrt{\frac{\epsilon_1 \epsilon_2}{\epsilon_1 + \epsilon_2}}, \quad (1.61)$$

where \underline{k}_x represents the SPP wave vector, \underline{k}_{spp} and the Eq. 1.61 can be written as

$$\underline{k}_{spp} = k_0 \sqrt{\frac{\epsilon_1 \epsilon_2}{\epsilon_1 + \epsilon_2}}. \quad (1.62)$$

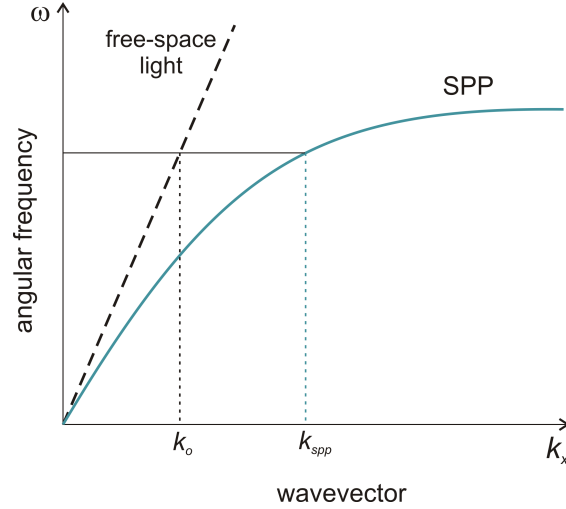


Figure 1.11: Dispersion relation of a SPP wave and a free-space plane wave. k_{spp} and k_0 are the wave vectors of a SPP wave and free-space plane wave, respectively. At any given frequency, k_{spp} is larger than k_0 .

Figure 1.11 shows typical dispersion curves for a SPP wave the interface between a metal and free-space and for a free-space plane wave. For a given frequency, the wave vector of the SPP wave (k_{spp}) is larger than the wave vector of a free-space plane wave (k_0), which results in wave vector mismatch.

The same exercise can be carried out for TE polarization. By postulating the existence of a TE-polarized, surface-bound electromagnetic wave and imposing continuity of the fields at the interface, the condition governing the existence of such surface waves is

$$\underline{E}_1 = \underline{E}_2, \quad (1.63)$$

and

$$\underline{E}_1(\underline{k}_{z1} + \underline{k}_{z2}) = 0, \quad (1.64)$$

where \underline{E}_1 and \underline{E}_2 are the complex amplitudes of the magnetic field in media 1 and 2, respectively. Again, if \underline{k}_{z1} and \underline{k}_{z2} are positive (to prevent runaway solutions far away from the interface) and strictly real, the only possible solution is that $\underline{E}_1 = \underline{E}_2 = 0$. In other words, surface electromagnetic waves cannot exist for TE-polarization at the interface of non-magnetic media.

1.13.1 Excitation of surface plasmon polaritons

A plane wave can excite SPPs when two conditions are satisfied: 1) the frequency of the incident plane wave and excited SPP are identical, and 2) the wave vector component of the plane wave along the metal-dielectric interface matches the SPP wave vector. The first condition is required to conserve energy, and the second condition is required to conserve momentum. When both conditions are fulfilled, the incident plane wave couples into SPPs with a high degree of efficiency. Classical methods to achieve SPP coupling involve discrete scattering elements, such as a prism or a grating, placed adjacent to a metal interface.

Prism coupling

The concept of prism coupling to SPPs was developed by the groundbreaking works of Otto, Kretschmann and Raether [39–41]. A prism coupling system requires at least three different systems: two dielectric systems with different refractive indices and a metallic system on which SPPs are sustained. Let us consider the case in which the higher-index dielectric is a prism and the lower-index dielectric is air. The goal in prism coupling is to boost the wave vector of an incident plane wave by having that plane wave go through the prism. When the prism is placed in close proximity to a metal-air interface, under certain conditions it becomes possible to match a wave vector component of the plane wave in the prism to that of the SPPs on the metal-air interface. When this matching is achieved, it is possible to couple the incident plane wave to the SPP wave with high efficiency (Fig. 1.12(a)).

In the Kretschmann-Raether configuration, a thin film of metal is deposited on one side of a prism and the metal film is illuminated through the prism by a beam of TM-polarized light. For a metal film that is sufficiently thin (on the order of tens of nanometres), it is possible to couple the incident beam across the metal film and interact with SPPs on the other side of the metal film. For a prism index $n > 1$, there exists a critical angle, θ_c , at which the following condition is satisfied

$$k_{spp} = nk_0 \sin \theta_c, \quad (1.65)$$

where k_{spp} is the SPP wave vector on the air-metal interface. At this critical angle, incident light couples optimally to the SPP wave.

In the Otto configuration, the prism is separated from the metal surface by a thin air gap. TM-polarized light is incident through the prism and

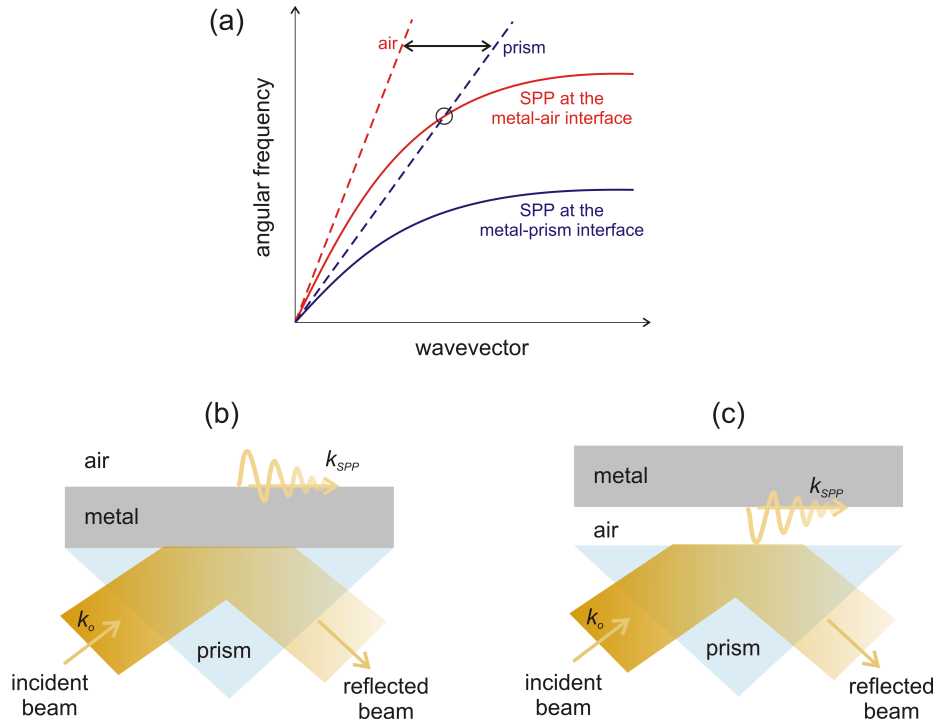


Figure 1.12: Schematic of light coupling to SPPs by using a prism. (a) Mechanism of wave vector matching by prism coupling, manifested in the (b) Kretschmann configuration and (c) Otto configuration.

directed at the air gap at sufficiently large angles so that light undergoes total internal reflection (TIR). Evanescent waves generated by TIR tunnel through the air gap and interact with SPPs at the air-metal interface. Similar to the Kretschmann-Raether configuration, there exists a certain critical angle when the wave vector component of the incident light along the metal-air interface matches the SPP wave vector on the air metal interface, satisfying the condition Eq. 1.65. SPP coupling is optimal at this critical angle. In both the Otto and Kretschmann-Raether configurations, the excitation of SPPs is detected and measured by observing a drop in the reflected light intensity. At the current state-of-the art, prism-coupled SPPs are used commercially for biochemical sensing [42].

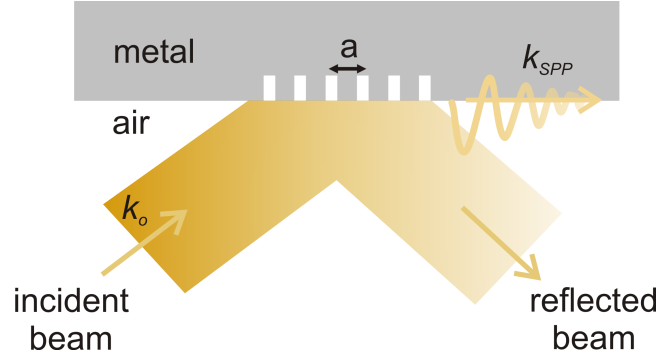


Figure 1.13: Schematic of free-space light coupling to SPPs using a grating immersed in free-space.

Grating coupling

It is also possible to couple incident light onto a metal surface by patterning the metal surface with a grating [41, 43]. Figure 1.13(b) shows a simple grating structure immersed in free-space with a grating constant (corresponding to the distance between two adjacent grooves) of a . TM-polarized light incident on the grating structure at a certain angle scatters into discrete diffraction orders, which boosts the wave vector component along the metal surface by an amount equal to an integer multiple of the grating spatial frequency $g = 2\pi/a$. At a critical angle θ_c , it is possible that one of the diffracted components has a wave vector component that matches the SPP wave vector at the metal interface, fulfilling the following condition

$$k_{spp} = k_0 \sin \theta_c \pm \nu g, \quad (1.66)$$

where ν is an integer corresponding to a particular diffracted component. At the critical angle, the diffracted component couples optimally to the SPP wave. Similar to prism coupling, SPP excitation in a grating structure is realized by observing a drop in the reflected light intensity.

Aperture coupling

Since the pioneering work of Ebbesen and colleagues [23], it has been realized that patterning a metal surface with small apertures can also excite SPPs. Figure 1.14 shows the schematic of aperture coupling. Similar to the scattering mechanism employed in grating coupling, small apertures

scatter incident light into a continuum of directions and it is believed that components of the scattered light can couple to SPPs when there is wave vector matching to the SPP wave vector. However, unlike grating coupling, the exact coupling mechanism in single apertures is not well established and there does not exist a well-defined succinct expression, such as that used to describe optimal SPP coupling using a prism or a grating, that can be used to predict when high efficiency coupling to SPPs is achieved. A major limitation of aperture coupling is that only a small portion of light near the aperture effectively couples to SPPs, making it much less efficient than prism or grating coupling in terms of the overall power carried by an incident beam. To the best of our knowledge, the maximum SPP coupling efficiency that has been experimentally achieved using an aperture is on the order of 20-30% (this is measured relative to the amount of light leaving the aperture). Prior to the work of this thesis, the highest SPP coupling efficiency achieved with a slit aperture was 22% [44], realized using a sub-wavelength slit in a gold film at a free-space wavelength of 785 nm. The highest SPP coupling efficiency achieved with a hole aperture is 28% [45], realized using a sub-wavelength hole in a gold film at a free-space wavelength of 800 nm. Although aperture coupling is less efficient than prism and grating coupling, their advantages include inherent insensitivity to the incident angle, compactness and ease of integration into complex photonic structures. These features make aperture-based SPP coupling a front-runner in the miniaturization of photonic devices.

With the advent and widespread availability of advanced nanofabrication techniques, the excitation and manipulation of SPPs near nano-structured metallic media has, for the past few decades, become a thriving area of modern optics research known as nano-photonics [30, 46–48]. In Figure 1.15, we highlight some representative, recent research work in which SPPs have been excited and manipulated on various nano-patterned surfaces or devices.

1.14 Understanding aperture coupling to surface plasmon polaritons

Although it is generally accepted that small apertures are efficient couplers to SPPs (relative to the amount of light incident onto the aperture), the precise microscopic mechanism underlying the excitation process remains a mystery and has been the subject of continuing research. Based on Kowarz's application of scalar diffraction theory to describe near-field diffraction patterns near small slits, Thio and Lezec [53] proposed that the

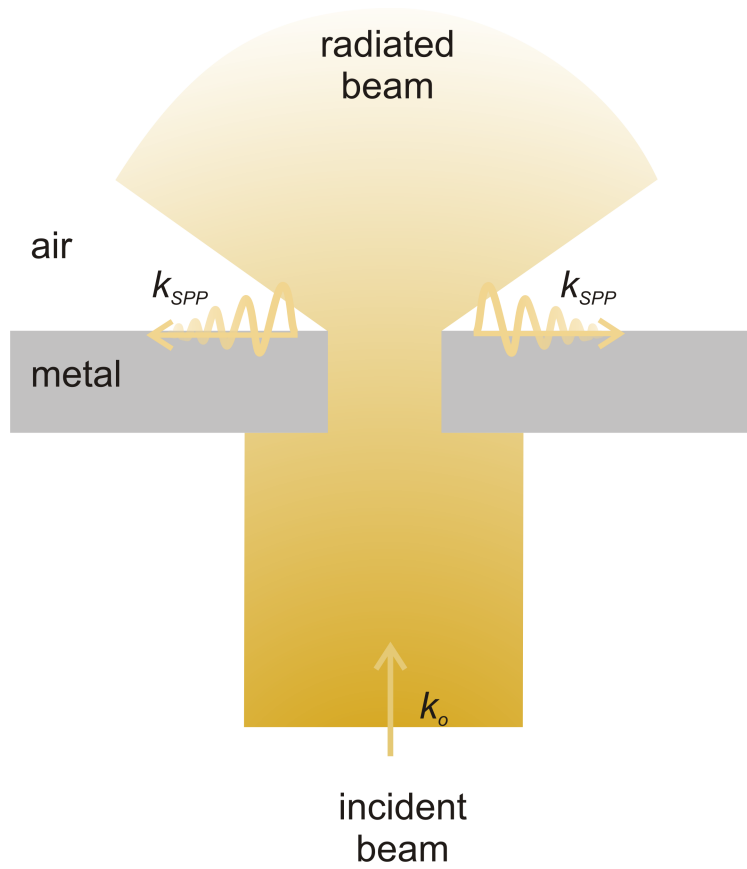


Figure 1.14: Schematic of the coupling of free-space light to SPPs by an aperture.

1.14. Understanding aperture coupling to surface plasmon polaritons

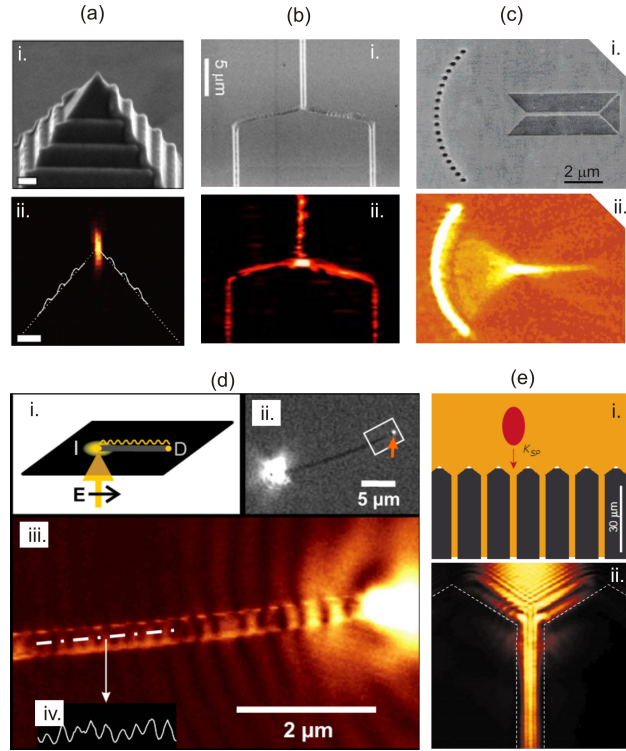


Figure 1.15: (a) Three-dimensional plasmonic nano-focusing of light with asymmetrically patterned silver pyramids [49] showing i) a scanning electron microscope (SEM) image of the device, ii) a side-view of the scanning confocal Raman image at an incident wavelength of 710 nm. (b) Splitting of surface plasmons into two channels [50], showing i) a SEM image and ii) a near-field optical image at an incident wavelength of 1600 nm. (c) Sub-wavelength focusing of surface plasmon to a 250-nm-wide Ag strip guide with a curved array of holes [51], showing i) a SEM image (light gray, Ag and dark gray, Cr) and ii) a near-field optical image of SPP focusing and guiding at a wavelength of 532 nm. (d) Surface plasmon propagation along a $18.6\ \mu\text{m}$ long silver nano-wire at an incident wavelength of 785 nm [52], showing i) a sketch of optical excitation where I is the input and D is the end of the wire, ii) a conventional optical microscopic image showing the bright spot to the left is the focused exciting light, iii) a near-field optical image corresponding to the white box in ii, and iv) a $2\text{-}\mu\text{m}$ -long cross-cut along the chain dotted line in iii. (e) Surface plasmon waveguiding [30], showing i) a SEM image and ii) photon scanning tunneling microscopy image at an wavelength of 800 nm.

exit of a small hole or slit consists of a spectrum of evanescent waves generated by diffraction from the aperture edges. The composition of the evanescent wave spectrum is determined by the Fourier transformation of the field profile along a plane at the exit of the aperture and it is the composite sum of these evanescent waves that defines the surface wave generated at the exit of a small aperture. Later works, from the same research group, concluded that surface waves near an aperture are formed by combining the composite evanescent wave and surface plasmon polaritons available at the metal surface [54, 55]. Although these works provided insights into the role of diffraction in aperture coupling to SPPs, they did not provide quantitative estimates of SPP coupling from apertures. Later, Lalanne and his colleagues theoretically examined SPP generation at the exit of a sub-wavelength slit [56, 57] by proposing a semi-analytical model that was used to quantitatively estimate SPP coupling efficiency. SPP excitation was described microscopically based on a two-stage scattering mechanism. The first stage describes the diffraction of light at the slit exit, which, like in the picture proposed by Thio and Lezec, forms a spectrum of rapidly decaying evanescent waves. The second stage describes the subsequent launching of relatively slowly decaying surface plasmon polaritons [37]. Like many other studies of light interaction with a sub-wavelength slit, Lalanne invoked the single-mode approximation to formulate the model. The model was used to calculate SPP excitation efficiency as a function of slit width, revealing an optimum ratio between the slit width and operating wavelength ratio where SPP coupling efficiencies were as high as 40% (the percentage light leaving the slit that converts to SPPs). The model was also validated against experimental data of the transmission through a two-slit system [58]. While Lalanne's model was restricted to sub-wavelength slit widths, Renger and colleagues were the first to conduct experimental and analytical research into SPP excitation efficiency as a function of slit width beyond the sub-wavelength regime [59]. This work revealed an oscillatory dependence of the SPP coupling efficiency on the slit width and that optimizing the slit width could result in SPP conversion efficiencies as high as 50%. Additional experimental evidence of the sensitivity of SPP coupling on the slit width was later investigated by several other researchers [44, 60], who used near-field scanning optical microscopy or far-field leakage radiation microscopy to detect the SPPs excited by slits of variable width.

While previous research has provided new insights into SPP coupling and hinted at the possibility of further enhancements in SPP coupling efficiency, some basic questions remain which will be addressed in this thesis. In all research conducted so far, the simplifying single-mode approximation was

used in which the field distribution in the aperture is restricted to be either that of the lowest-order mode or a simple top-hat profile. What is the role, if any, of higher order modes in the aperture on SPP coupling? Also, past investigations have been restricted to apertures immersed in semi-infinite dielectric media. What is the effect of loading the apertures with dielectric layers and what effect does this have on the SPP coupling efficiency? Can further SPP coupling efficiency gains be realized? The literature has also so far reported on SPP coupling measurements at single wavelengths - is it possible to excite SPPs over a broad range of wavelengths and how can this be achieved? In the next section, we will introduce our basic physical model of SPP coupling from a single slit which goes beyond the single-mode approximation. This model will be used to study optimal configurations to achieve high-efficiency SPP coupling from slits having both sub-wavelength width and super-wavelength width.

1.15 Improving the excitation efficiency of surface plasmon polaritons

In this work, we propose a basic physical model to analyze SPP excitation at the exit of a slit in a metallic film. Inspired by Lalanne's earlier work [56] describing SPP excitation as a two-step scattering process, we similarly describe the SPP coupling process by analyzing the electromagnetic response of two distinct segments: the slit and the adjacent metallic surface. To analytically describe the electromagnetic response of the slit, we approximate the slit structure to be an infinite metal-dielectric-metal (MDM) waveguide, where the dielectric region represents the slit opening and the semi-infinite metallic claddings represent the metallic walls of the slit. To describe the electromagnetic response of the adjacent metallic surface, we approximate the surface to be an infinite metal-dielectric (MD) waveguide. By conceptually dividing the slit geometry into two infinite waveguide segments, the complex two-dimensional problem of SPP coupling from a slit is simplified into two classical electromagnetic boundary value problems. The solutions of the boundary value problems yield the modes of the waveguide segments, described in terms of a two-dimensional wave vector. The component of the wave vector parallel to the axis of the waveguide describes the propagation constant and the component perpendicular to the axis describes the confinement of the mode. By mapping out the allowable wave vectors in the two waveguide segments, it is now possible to investigate the coupling of waves from one segment to the other by invoking the phase matching concept. We

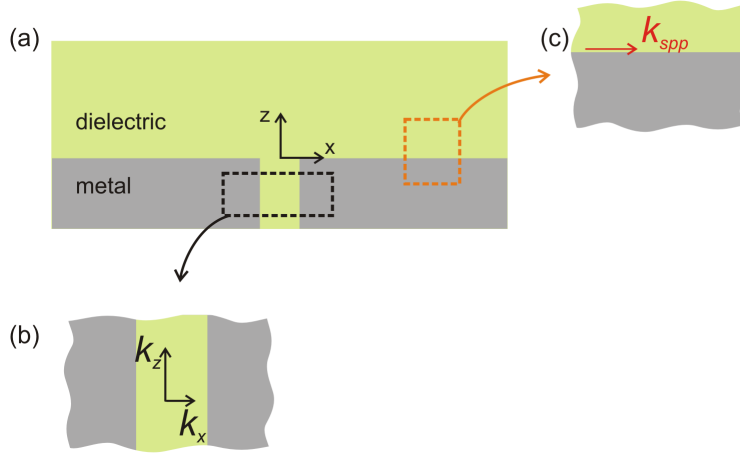


Figure 1.16: (a) Basic two-dimensional configuration to be studied consisting of a slit in a metallic film. The slit structure is conceptually divided into two uni-axial semi-infinite waveguides: (b) a vertical metal-dielectric-metal (MDM) waveguide, which sustains longitudinal and transverse wave vector components k_z and k_x , respectively, and (c) a horizontal metal-dielectric (MD) waveguide, which sustains a longitudinal wave vector component k_{spp} along the metal-dielectric interface. Wave vector matching is achieved when the transverse component of the wave vector in the MDM waveguide matches with the longitudinal component of the wave vector in the MD waveguide.

hypothesize that maximum coupling efficiency to SPPs is achieved when the mode in the MDM waveguide segment (approximating the slit) has a perpendicular wave vector component that matches the SPP wave vector component along the metal surface. By mapping the wave vectors of the modes in the wave guide segments as a function of wavelength, geometry, and material composition, conditions for optimal SPP coupling can be predicted. We will then use numerical simulations and experimental measurement to confirm the existence of maximal coupling under the conditions predicted by this model.

1.16 Thesis outline

The thesis is structured to present a new method to improve the excitation efficiency of surface waves near slits in metallic films. In Chapter 1, we have provided a detailed account of the rich history of the study of light transmission through apertures, introducing foundational concepts including Huygens' principle, Maxwell's equations, scalar diffraction theory, and Fraunhofer diffraction, in addition to more advanced concepts to be used later in the thesis such as angular spectrum representation and numerical solvers of Maxwell's equations. We have highlighted some recent research results that have sparked tremendous research interest in understanding the excitation of SPPs in the vicinity of apertures in metallic films. We have discussed the basic theory of SPPs on a metal-dielectric interface and have introduced a basic physical model that we will use in this thesis to improve and optimize SPP coupling near slit apertures. The next two chapters will provide detailed discussions of the application of our model to optimize SPP coupling from a slit and give numerical and experimental results that verify the predictions made by the model. Chapter 2 will consider the geometry of a slit that has sub-wavelength dimensions and is coated with a thin dielectric layer. Portions of this chapter have been published in [61, 62]. Chapter 3 will consider the geometry of a slit that has super-wavelength dimensions and is immersed in a high-index dielectric medium. Portions of this chapter have been published in [63]. For both sub-wavelength and super-wavelength slit geometries, it is shown that the proposed physical model is capable of accurately predicting conditions for optimal SPP coupling. In Chapter 4, we conclude the thesis by summarizing the assumptions made throughout the work, highlighting the key findings, and providing future directions of the work. Appendix A describes commonly used plasmonic materials and their electromagnetic properties over a broad range of frequencies. Appendix B provides a brief description of the equipment used to fabricate the devices used in the experiments of Chapter 2 and Chapter 3.

Chapter 2

Improving the SPP Coupling Efficiency Near a Sub-wavelength Slit

We begin our investigation of SPP coupling near an aperture by considering the simplest case of a slit in a metallic film having sub-wavelength dimension. The slit geometry has been chosen, as opposed to a more complex aperture shape such as a hole, because it provides the simplest configuration whose electromagnetic response can be analyzed in two dimensions. We have specifically focused on slits with sub-wavelength width because we are permitted in this regime to invoke the single-mode approximation to describe the distribution of light in the slit. It should be noted that SPP coupling from sub-wavelength slits immersed in air has been studied extensively, with typical SPP coupling efficiencies (percentage of light leaving the slit that couples to an adjacent surface wave) reported in the literature to be around 20% (experiment) [60], 22% (experiment) [44] and 40% (calculation) [56] at visible frequencies. In this Chapter, we will show that coating a sub-wavelength slit with an ultra thin layer of dielectric can result in SPP coupling efficiencies around 70% at visible frequencies. We will first develop this idea by considering a simple physical picture of the SPP coupling process: light is scattered by the exit of the slit, generating a distribution of evanescent waves of which a portion couples to an adjacent SPP mode. We conceptually divide the slit structure into two regions — the near-field region at the slit exit and the dielectric-coated region above the metal surface — and then match the wave vector of the scattered light and that of the SPP mode. In general, the wave vector of light in the near-field of a slit is indeterminate. Diffraction of light at the slit exit yields a near-field light distribution describable by a distribution of wave vector values oriented along a continuum of directions. For initial design considerations, however, we make the simplifying assumption that a large fraction of light at the slit exit possesses wave vector values equal to that of light in a dielectric, nk_0 ,

where n is the refractive index of the dielectric, with a component oriented along the metal surface that is amenable to SPP coupling. Due to the presence of the thin dielectric layer, the wave vector of the SPP mode can be continuously tuned over a wide range of values. We hypothesize that there is an optimal dielectric layer thickness that leads to wave vector matching between the SPP mode and the light scattered from the slit exit. This hypothesis is initially tested by conducting a series of numerical simulations using the FDTD method in which the SPP coupling efficiency is quantified as a function of the dielectric layer thickness. The simulation results reveal the existence of an optimal dielectric layer thickness resulting in peak efficiencies about four times greater than the efficiency without the dielectric layer. We next experimentally test the hypothesis by fabricating a series of slit structures coated with dielectric layers of varying thickness and measure the SPP coupling efficiencies from the slits. The experimental results also indicate a marked enhancement of the SPP coupling efficiency by coating the slit with thin dielectric layers. Based on the evidence, we conclude that adding a thin dielectric layer to a slit provides a simple method to improve the SPP coupling efficiency from slits. The added benefit of the addition of the dielectric layer is that the metallic film is passivated, naturally prolonging the lifetime of the metal as a SPP-sustaining surface.

2.1 SPP coupling from a coated slit

Figure 2.1(a) depicts the geometry of the SPP coupling structure to be studied consisting of a slit in a semi-infinite metal film with relative permittivity ϵ_m is immersed in a dielectric medium with relative permittivity ϵ_d . The film extends infinitely in the x - and y -directions and occupies the region $-t < z < 0$. A slit of width w oriented parallel to the z -axis and centred at $y = 0$ is cut into the metal film. A TM-polarized electromagnetic plane wave of wavelength λ_0 and wave vector nk_0 , where $n = \sqrt{\epsilon_d}$ is the refractive index of the dielectric, is normally incident onto the bottom surface of the film located at $z = -t$. A fraction of the electromagnetic plane-wave mode incident onto the slit couples into a guided mode in the slit. According to the scalar diffraction picture put forward by Kowarz [9], light exiting the slit in the region $z > 0$ consists of radiating and evanescent modes with wave vector magnitude $k_i \simeq nk_0$; coupling to the SPP mode on the metal surface is not perfect because k_i is less than the wave vector of the SPP mode on

2.1. SPP coupling from a coated slit

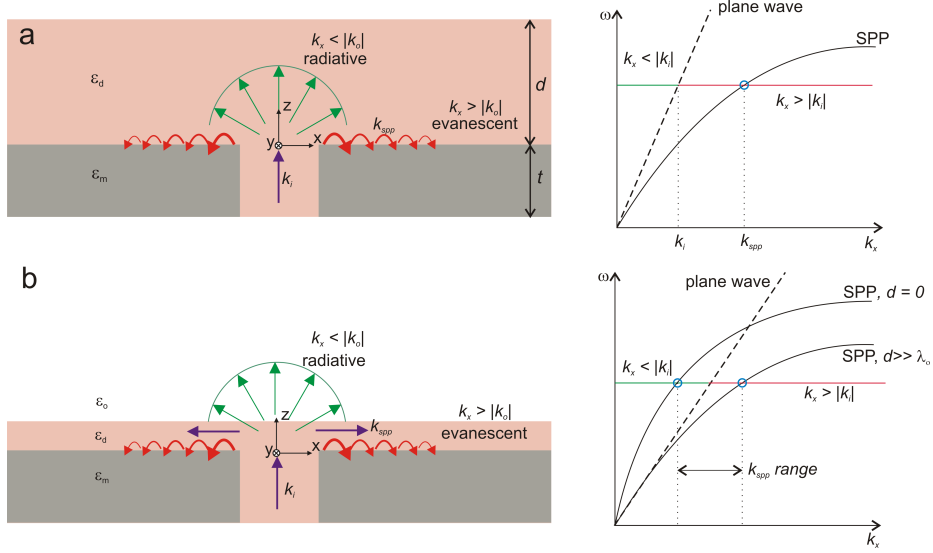


Figure 2.1: (a) Real-space (left) and k -space (right) depictions of the modes scattering from the exit of a slit in a metal film when the metal film is completely immersed in a dielectric. (b) Real-space (left) and k -space (right) depictions of the modes scattering from the exit of a slit in a metal film when the slit is filled with a dielectric and the metal film is coated with a dielectric layer.

the metal surface, k_{spp} , given by

$$k_{spp} = k_0 \sqrt{\frac{\epsilon_m \epsilon_d}{\epsilon_m + \epsilon_d}}. \quad (2.1)$$

Diffraction at the slit exit disperses the modes at the slit exit into a continuum of directions described by $\vec{k} = k_x \hat{x} + k_z \hat{z}$. Assuming the Kirchhoff boundary conditions at the exit of the slit (which can be considered the original single-mode approximation), field distribution in the plane $z = 0$ has the form

$$E(x, 0) = \begin{cases} E_i & |x| < w/2 \\ 0 & |x| > w/2 \end{cases} \quad (2.2)$$

where E_i is a constant. As the geometry is two-dimensional, we can decompose the field distribution at the plane of the slit exit into a diffraction

2.1. SPP coupling from a coated slit

spectrum given by

$$f(k_x) = \frac{E_i}{\pi} \frac{\sin(k_x w/2)}{k_x}. \quad (2.3)$$

Diffracted modes that assume a real wave vector x -component $k_x < k_i$ possess a real wave vector z -component

$$k_z = (k_i^2 - k_x^2)^{1/2}, \quad (2.4)$$

corresponding to radiative modes that propagate away from the slit exit. On the other hand, diffracted modes that assume a real wave vector x -component $k_x > k_i$ possess an imaginary wave vector z -component

$$k_z = i (k_x^2 - k_i^2)^{1/2}, \quad (2.5)$$

corresponding to evanescent modes confined to the slit region. A fraction of the evanescent modes with values of k_x matching the wave vector of the SPP mode on the air-silver interface couple from the slit exit to the $\pm x$ -directed SPP modes.

The total intensity radiated from the slit, I_r , is obtained by a summation, weighted by the squared amplitude distribution of the diffraction spectrum, of the intensities of the radiated modes [9]

$$I_r = \frac{4|E_i|^2}{\pi k w^2} \int_0^{k_i} \frac{\sin^2(k w/2)}{k^2} dk. \quad (2.6)$$

Likewise, the total intensity confined to the slit-exit plane, I_e , is obtained by a summation of the intensities of the evanescent modes

$$I_e = \frac{4|E_i|^2}{\pi k w^2} \int_{k_i}^{\infty} \frac{\sin^2(k w/2)}{k^2} e^{-2\sqrt{k_x^2 - k_i^2} z} dk. \quad (2.7)$$

A fraction of I_e constitutes the SPP mode intensity I_{SPP} and the remainder constitutes the intensity of decaying modes I_d . The observable coupling efficiency of the radiating light from the slit to the SPP mode on the metal surface can be expressed as

$$\eta = \frac{I_{SPP}}{I_r + I_{SPP}} \times 100\%, \quad (2.8)$$

which assumes a value in the range $0\% \leq \eta \leq 100\%$.

In contrast to SPP coupling efficiency calculations based on the total incident beam, which is used for SPP couplers based on prisms and gratings, we define the SPP coupling efficiency of a slit by considering the light

2.1. SPP coupling from a coated slit

leaving the slit. There are two reasons for this approach. First, it is a well-established method in the literature [44, 56, 60]. Second, this definition is independent of the incident beam size. If the SPP coupling efficiency from a slit were to be taken with respect to the incident beam, then in the limit of an infinite plane wave, the SPP coupling efficiency would approach zero. Thus, normalization of the SPP coupling efficiency by the light leaving the slit ensures that the calculated efficiency depends only on physics at the slit exit. Note that we are using intensities to define the SPP coupling efficiency. It is also possible to define the coupling efficiency in terms of field quantities, which are accessible through simulations, but an intensity-based definition of coupling efficiency enables more direct comparison with intensity-based experimental measurements to appear later in the chapter.

To enhance the SPP coupling efficiency from a slit, the configuration depicted in Figure 2.1(b) is proposed. A semi-infinite metal film with a slit of width w is immersed in free-space with permittivity ϵ_o . The slit in the film is completely filled with a lossless dielectric of relative permittivity ϵ_d . A semi-infinite dielectric layer, also of relative permittivity ϵ_d , is placed on the metal film such that it occupies the region $0 < z < d$. In the limits where $d \rightarrow \infty$ and $d \rightarrow 0$, the SPP wave vector approaches

$$k_{spp} = k_0 \sqrt{\frac{\epsilon_m \epsilon_d}{\epsilon_m + \epsilon_d}}, \quad (2.9)$$

and

$$k_{spp} = k_0 \sqrt{\frac{\epsilon_m}{\epsilon_m + 1}}, \quad (2.10)$$

respectively. Thus, the thickness of the dielectric layer on the metal film now enables the continuous tuning of the SPP wave vector over a range that spans nk_0 . At this point, we assume that the magnitude of the wave vector of the radiating and evanescent modes at the slit exit in the region $z > 0$ is $k_i \simeq nk_0$; in reality, the light radiating from the slit consists of a distribution of wave vector magnitudes, of which a large fraction corresponds to nk_0 [9, 53]. By varying the thickness of the dielectric layer, d , the effective wave vector of the SPP mode can be tuned such that the wave vector matching condition $k_{spp} \simeq k_i$ is achieved, enabling efficient coupling of light from the slit into the SPP mode on the adjacent metal surface. The dielectric layer has an added practical benefit of passivation of the underlying metal surface; this is especially important for the case of silver, which is an excellent plasmonic material but tarnishes rapidly in atmosphere.

2.2 Numerical investigation of enhanced SPP coupling

To test the hypothesis of enhanced SPP coupling, we use the two-dimensional FDTD method to study the SPP-coupling efficiency as a function of the slit width ranging from 50 nm to 300 nm, the thickness of the dielectric layer ranging from 0 nm to 700 nm, and the incident wavelength ranging from 400 nm to 700 nm and determine a set of optimal parameters that yield maximum coupling. We will show in this section that judicious selection of the dielectric layer thickness and the slit width can yield coupling efficiency $\eta \simeq 77\%$ extending over the visible wavelength range $400 \text{ nm} \leq \lambda_0 \leq 700 \text{ nm}$; the achieved efficiency is $\simeq 4$ times more efficient than that observed for a slit without the dielectric layer. Design guidelines established by FDTD in this section could potentially be used to assist the experimentalist in realizing coupling geometries that yield optimal SPP coupling.

2.2.1 Simulation design

We select the two-dimensional FDTD method to map out the electromagnetic response of the structure. The simulation grid has dimensions of 4000×1400 pixels with a resolution of 1 nm/pixel and is surrounded by a perfectly-matched layer to eliminate reflections from the edges of the simulation space. We consider a structure consisting of an optically thick (300-nm-thick) silver film with a slit of width w ; the dielectric in the slit and the dielectric layer on the metal film consist of dispersion-less glass with refractive index $n = 1.5$. The permittivity of silver is modeled using the Drude model, which is in good agreement with the experimental data over the visible frequency range, as will be discussed in the Appendix. The corners of the slit are chamfered with a chamfer radius of 3 nm. This was done to eliminate perfectly sharp edges of the slit which can result in highly localized electric dipoles that affect the slit throughput [10]. We use a TM-polarized incident beam, which is centered in the simulation space at $x = 0$ and propagates in the $+z$ -direction, with a full-width-at-half-maximum (FWHM) of 1200 nm and a waist located at $z = 0$. The beam width is selected many order larger than the slit so that the electromagnetic wave incident on the slit can be approximated as plane wave incidence. The incident electromagnetic wave has a wavelength of 500 nm and is TM-polarized such that the magnetic field, H_y , is aligned along the y -direction.

The control variables are the incident polarization (TM), the metal type (silver), the dielectric type (dispersion-less glass), and the thickness of the

2.2. Numerical investigation of enhanced SPP coupling

metal layer ($t = 300$ nm). The independent variables are the slit width w , which is varied from 50 nm to 300 nm in increments of 50 nm, the dielectric layer thickness d , which is varied from 0 nm to 700 nm in increments of 50 nm, and the free-space wavelength λ_0 , which is varied over the visible frequency regime from 400 nm to 700 nm in increments of 100 nm. The dependent variables are the intensity of the SPP modes coupled to the exit surface of the metal film, I_{SPP} , and the intensity of the radiated modes leaving the slit region, I_r , which will both be used to compute the SPP coupling efficiency, η .

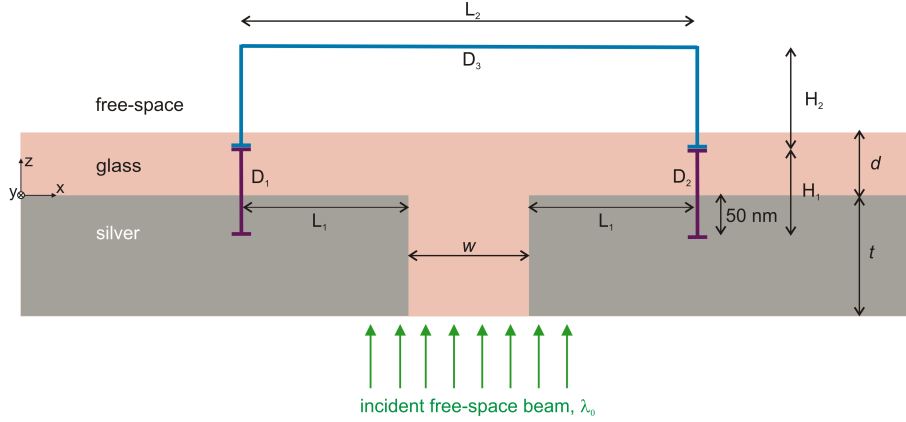


Figure 2.2: Simulation geometry used to study SPP coupling from an illuminated slit. The detectors D_1 and D_2 capture the SPP modes, and the detector D_3 captures the radiating modes.

The dependent variables are quantified in the simulations by placing line detectors, D_1 , D_2 , and D_3 , in the simulation space to integrate the instantaneous magnitude squared of the magnetic field crossing the plane of the detectors (as shown in Figure 2.2). The detectors, D_1 , D_2 , and D_3 , capture different components of the intensity pattern radiated from the exit of the slit. The line detectors D_1 and D_2 straddle the metal/dielectric interface and are situated adjacent to the slit exit a length $L_1 = \lambda_0$ away from the edges of the slit. D_1 and D_2 have identical heights $H_1 = \lambda_0/4 + 50$ nm, of which 50 nm extends into the metal and $\lambda_0/4$ nm extends into the dielectric region above the metal. The extension of the line detectors into the metal surface has been selected to be larger than the skin depth, and the extension above the metal surface has been selected based on observed decay scales of the SPP mode. D_1 and D_2 capture the intensity of the left- and right-

propagating SPP modes that are coupled from the slit and flow on the metal surface. The line detector D_3 is centered on the slit and extends over the dielectric region above the metal surface with a height of $H_2 = 3\lambda_0/4$ and a length of $L_2 = 2\lambda_0 + w$. D_3 captures the intensity of light radiated away from the slit that is not coupled to the surface of the metal.

Because the detectors indiscriminately capture the intensity crossing the detector plane, I_r captured by D_1 and D_2 and I_{SPP} captured by D_3 constitute sources of error. The fraction of I_r captured by D_1 and D_2 is estimated by calculating the acceptance angle formed by the line detectors D_1 and D_2 with respect to the exit of the slit and integrating Eqn. 2.6 over this angle. At $\lambda_0 = 500$ nm, $< 3\%$ of I_r is captured by D_1 and D_2 . The fraction of I_{SPP} captured by D_3 is estimated from the attenuation of the SPP fields in the z -direction. At $\lambda_0 = 500$ nm, $< 8\%$ of I_{SPP} is captured by D_3 . It should be noted that the placement of the detectors and our definition of efficiency ignores the effects of reflection of the incident beam, propagation loss through the slit, and absorption loss of SPPs propagating on the metal-dielectric interface to the detectors. The detectors placement here has been largely influenced by later experimental configurations and measurements. It is also possible, for example, to measure I_r and I_{SPP} by placing a horizontal detector across the exit of the slit; however, this detection scheme suffers from near-field resonance effects within the slit which yields efficiency values inconsistent with far-field measurements.

The time-averaged intensities of the SPP mode and the radiated modes are quantified by

$$I_{SPP} = \langle \int_{D_1} |H_y|^2 d\ell + \int_{D_2} |H_y|^2 d\ell \rangle, \quad (2.11)$$

and

$$I_r = \langle \int_{D_3} |H_y|^2 d\ell \rangle, \quad (2.12)$$

where the angled brackets indicate time-averaging of the quantity within the brackets.

2.2.2 Control studies

Three control simulations are performed to establish baseline SPP coupling efficiency values. As summarized in Table 2.1, the control structures consists of a silver film of thickness $t = 300$ nm having a slit width of $w = 150$ nm, where 1) the film is surrounded by free-space and the slit is filled with free-space, 2) the film with one side is attached to glass, while

2.2. Numerical investigation of enhanced SPP coupling

the other side is open to free-space and the slit is filled with glass, and 3) the film is surrounded by and the slit is filled with glass. The slits are illuminated with a wide gaussian beam, which can be approximated as a plane wave at the slit, with a wavelength $\lambda_0 = 500$ nm, when the light is incident at the bottom of the structures. Each geometry represents different situations in which the magnitude of the wave vector (or equivalently, wavelength) of the light radiating in the immediate vicinity of the slit exit is mismatched with the SPP wave vector (or wavelength) on the metal surface. The wavelength of the emanating light, λ_i , and of the SPP mode, λ_{spp} , are given in Table 2.1.

Simulation Geometry	λ_i	λ_{spp}	η
	500 nm	473 nm	20%
	500 nm	473 nm	21%
	333 nm	292 nm	25%

Table 2.1: Control simulation geometries and results. Fixed parameters include $w = 150$ nm, $d = 100$ nm, $t = 300$ nm, and $\lambda_0 = 500$ nm.

Shown in Figure 2.3 is a snap-shot of the instantaneous $|H_y|^2$ distribution for illumination of the silver film immersed in free-space. The slit sustains a field-symmetric mode that carries electromagnetic energy across the extent of the slit. A significant portion of the fields radiating from the slit exit propagates in free-space away from the metal surface (captured by the D_3 detector), and a lesser portion of the fields couple into confined left- and right-propagating modes on the metal surface (captured by the detectors D_1 and D_2). The wavelength of the confined mode on the metal surface is $\lambda_{spp} = 480 \pm 10$ nm, where the error corresponds to the observed variation of the SPP mode wavelength as a function of distance from the slit. An SPP coupling efficiency of $\simeq 20\%$ is measured for the slit immersed in free-space. SPP coupling efficiencies of $\simeq 21\%$ and $\simeq 25\%$ are measured, respectively, for the dielectric-filled slit immersed in free-space and the slit immersed in

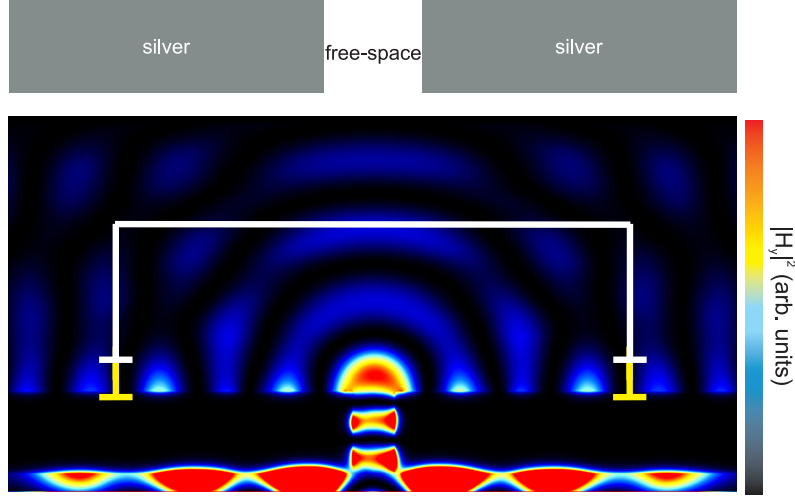


Figure 2.3: Image of the FDTD-calculated instantaneous $|H_y|^2$ distribution for a slit of width $w = 150$ nm illuminated by a quasi-plane-wave of wavelength $\lambda_0 = 500$ nm. The simulation geometry is depicted by the above graphic. Lines indicating the position of detectors D_1 , D_2 , and D_3 have been superimposed on the image.

dielectric (see Table 2.1).

2.2.3 Results

Variations in the thickness of the dielectric layer on the metal film enable tuning of the SPP wave vector, k_{spp} , and hence, the effective refractive index of the SPP mode, $n_{spp} = k_{spp}/k_0$. The dispersion curves for n_{spp} as a function of λ_0 and d are determined by iteratively solving the complex eigenvalue equation for the wave vector k_{spp} of the mode sustained by an asymmetric, three-layer silver-glass-air waveguide, where the thickness of the glass layer is d . As shown in Figure 2.4(a), n_{spp} increases asymptotically as λ_0 decreases from 1900 nm to 400 nm. For finite d , the n_{spp} dispersion curves are bound between the curves corresponding to $d = 0$ (air-silver interface) and $d \gg \lambda_0$ (glass-silver interface). As shown in Figure 2.4(b), at a fixed $\lambda_0 = 500$ nm, n_{spp} as a function of d can assume a continuum of values in the range $1.05 < n_{spp} < 1.72$. The phase matching condition $n_{spp} \simeq n = 1.5$ is predicted to occur for a dielectric layer thickness $d \simeq 75$ nm.

Figure 2.5 displays the instantaneous $|H_y|^2$ distributions for the illumi-

2.2. Numerical investigation of enhanced SPP coupling

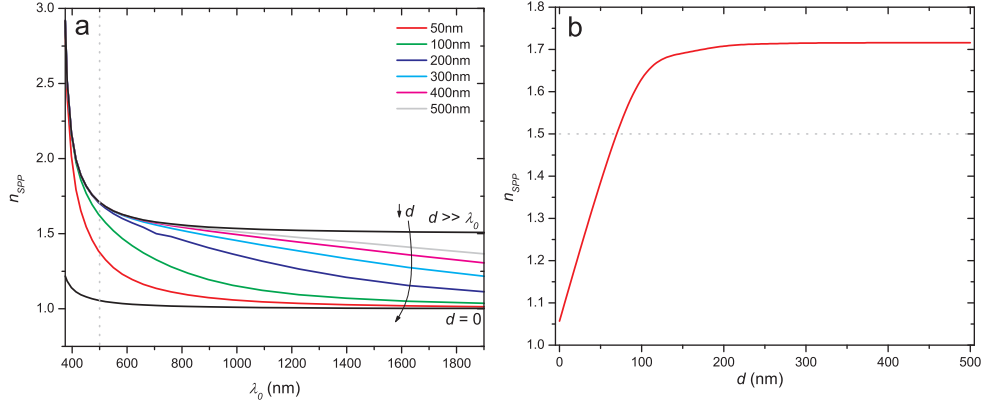


Figure 2.4: Basic principle used to enhance slit-coupling to SPP modes near a sub-wavelength slit in a metallic film. (a) Dispersion curve of n_{spp} as a function of λ_0 for various d calculated from the roots of the eigenvalue equation for the SPP mode on an asymmetric, three-layer silver-glass-air waveguide. (b) n_{spp} as a function of d for $\lambda_0 = 500$ nm. The dotted gray line corresponds to the refractive index of a plane-wave mode in glass, $\sqrt{\epsilon_d}$.

nation of silver films with dielectric layer thicknesses of $d = 100$ nm and $d = 500$ nm. The slit width $w = 150$ nm is held constant. High-efficiency SPP coupling is evident for $d = 100$ nm; the presence of the $d = 100$ nm dielectric layer on the metal film yields negligible radiated intensity and relatively high SPP intensity. SPP coupling efficiency drops as the dielectric layer thickness increases to $d = 500$ nm; the $|H_y|^2$ distribution reveals an increase in the radiated intensity and a reduction in the SPP intensity relative to that for $d = 100$ nm.

Figure 2.6 displays the time-averaged radiated intensity I_r and time-averaged SPP intensity I_{SPP} as a function of d , along with the corresponding SPP coupling efficiency, η . Appropriately selecting the dielectric layer thickness can yield both enhanced SPP coupling and reduced radiation from the slit. For values of d in the range $50 \text{ nm} < d < 150 \text{ nm}$, I_{SPP} is near-maximum and I_r is near-minimum, yielding an SPP-coupling efficiency $\approx 77\%$. For values of $d > 150$ nm, the efficiency curve drops and flattens. In the limits where $d \rightarrow 0$ nm and $d \rightarrow 700$ nm, the SPP-coupling efficiencies approach $\eta \rightarrow 20\%$ and $\eta \rightarrow 31\%$, respectively.

The layer thickness corresponding to high coupling efficiency approximately coincides with the layer thickness where the SPP wavelength, λ_{spp} ,

2.2. Numerical investigation of enhanced SPP coupling

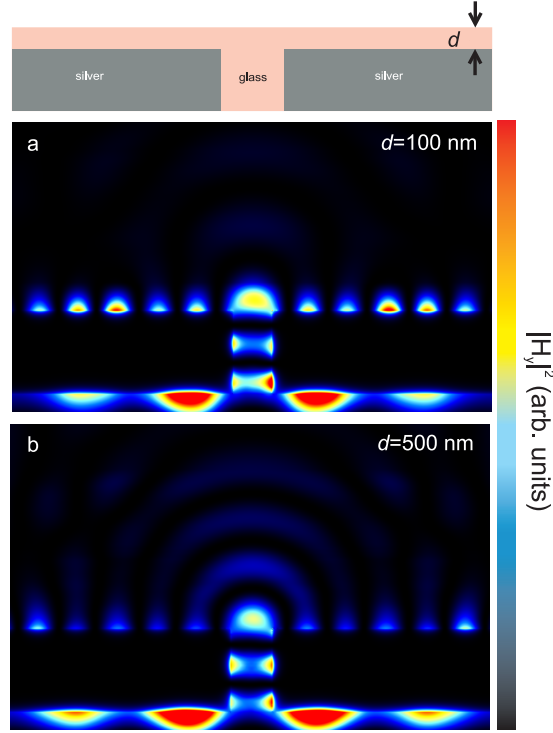


Figure 2.5: Image of the FDTD-calculated instantaneous $|H_y|^2$ distribution for a slit of width $w = 150$ nm illuminated by a quasi-plane-wave of wavelength $\lambda_0 = 500$ nm when a dielectric layer of thickness (a) 100 nm and (b) 500 nm is placed on the metal film. The simulation geometry is depicted by the above graphic.

matches the wavelength of light at the slit exit $\lambda_i = \lambda_0/n$. Figure 2.7 plots the SPP wavelength as a function of the dielectric layer thickness d . The SPP wavelength has been obtained by two methods: direct measurement from the FDTD-calculated $|H_y^2|$ distributions and calculation via the SPP modal solutions of the asymmetric silver-glass-air waveguide. There is a good match between the SPP wavelength values obtained by the FDTD simulations and the modal solutions. As d increases from 0 to 500 nm, the SPP wavelength reduces from 480 to 300 nm. At the layer thickness $d \simeq 100$ nm, yielding maximum SPP coupling efficiency, k_{spp} nearly matches k_i , which has been assumed to be nk_0 (although this is not generally true, as the modes at the exit of the slit assume a distribution of wave vector magnitudes, it has been

2.2. Numerical investigation of enhanced SPP coupling

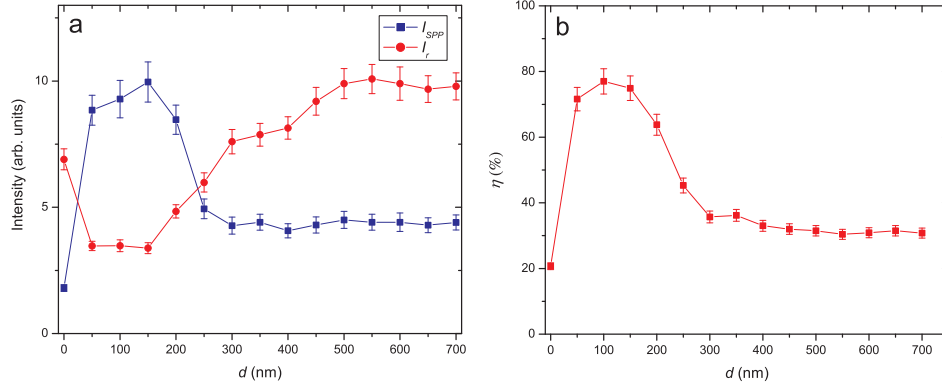


Figure 2.6: (a) The time-averaged SPP intensity, I_{SPP} (blue squares), and time-averaged radiated intensity, I_r (red circles), and (b) the corresponding SPP coupling efficiency, η , as a function of d . The error bars describe the uncertainties in the measurement of I_{SPP} and I_r due to, respectively, the finite amount of I_r captured by D_1 and D_2 and the finite amount of I_{SPP} captured by D_3 .

so far a useful and accurate approximation). The correlation between the high coupling efficiency and wavelength similarity between the SPP mode and the plane-wave mode in the dielectric suggest that phase-matched coupling is the primary culprit in the efficiency enhancement.

Changing the slit width affects the distribution of the modes at the exit of the slit, which in turn affects the SPP coupling efficiency. Figure 2.8 displays the instantaneous $|H_y|^2$ distributions for illumination of silver films with slit widths of $w = 150$ nm and $w = 300$ nm. The dielectric layer thickness $d = 100$ nm is held constant. The narrower slit shows weaker overall transmission through the slit, with the majority of the transmitted field coupled into the bounded SPP modes on the metal surface at the exit side of the slit. The wider slit exhibits greater overall transmission, with a significant portion of the transmission radiating from the metal surface. As w increases, a greater percentage of the modes at the slit exit are propagating modes that radiate away from the metal surface. In the limit where the slit width is very large ($w \gg \lambda_0$), a ray picture can be used where the majority of the incident light rays propagate directly through the slit and away from the slit exit.

Increasing the slit width generally reduces the efficiency of SPP coupling from the slit structure. The influence of the slit width on I_{SPP} , I_r , and η

2.2. Numerical investigation of enhanced SPP coupling

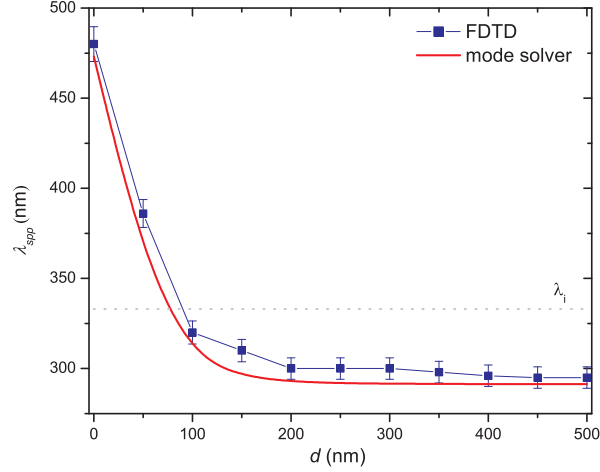


Figure 2.7: SPP wavelength measured from the FDTD simulations (blue squares) and predicted from the mode solver (red line) as a function of dielectric layer thickness d . The dotted gray line indicates the value of $\lambda_i = \lambda_0/\sqrt{\epsilon_d}$. The error bars describe the uncertainty in the measurement of λ_{spp} from the FDTD simulations due to variation in λ_{spp} as a function of distance from the slit exit.

is plotted in Figure 2.9. As w increases from 50 nm to 300 nm, I_r increases monotonically, while I_{SPP} peaks at $w = 250$ nm and then decreases at $w = 300$ nm. The corresponding SPP coupling efficiency monotonically decreases from $\simeq 83\%$ to $\simeq 18\%$ as the slit width increases from 50 nm to 300 nm.

To investigate the wavelength-sensitivity of the coupling structure, the electromagnetic response of a coupling structure with slit width $w = 200$ nm and dielectric layer thickness $d = 100$ nm is studied over free-space wavelengths ranging from 400 to 700 nm, in increments of 100 nm. SPP-coupling efficiencies of 66%, 67%, 66%, and 65% are observed at wavelengths of 400, 500, 600, and 700 nm, respectively. The coupling efficiency is largely insensitive to wavelength because the condition $k_{spp} \simeq k_i$ is achieved via near-field perturbation of the SPP mode using a $d \ll \lambda_0$ layer. That is, the dielectric layer shifts the k_{spp} wave vector commensurately throughout the visible frequency range and quasi-phase matching is obtained over a large spectral range.

To conclude this section, the FDTD results show that it is possible to enhance the efficiency of slit-coupling from a free-space plane-wave mode

2.2. Numerical investigation of enhanced SPP coupling

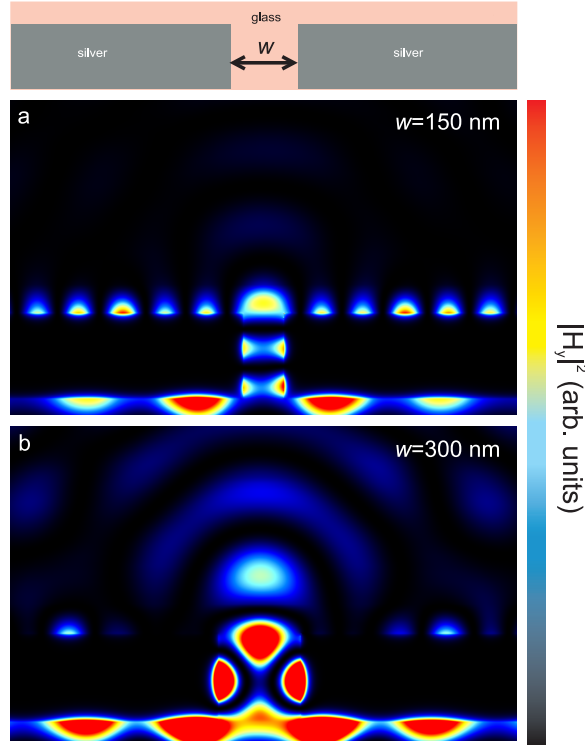


Figure 2.8: Image of the FDTD-calculated instantaneous $|H_y|^2$ distribution for a slit illuminated by a quasi-plane-wave of wavelength $\lambda_0 = 500$ nm when the slit width is (a) 150 nm and (b) 300 nm. The dielectric layer thickness $d = 100$ nm is held constant. The simulation geometry is depicted by the above graphic.

into a SPP mode on a metal film by filling the slit and placing an ultra-thin dielectric layer on the exit side of the metal film. Varying the thickness of the dielectric layer enables tuning of the SPP wave vector. When the SPP wave vector is matched with the wave vector magnitude of the modes exiting the slit, coupling efficiencies $\simeq 80\%$ can be achieved, $\simeq 4$ -times enhancement relative to the case without the dielectric layer. In the next section, we will describe the experimental implementation of this concept and validation of the SPP coupling enhancements predicted by simulations.

2.3. Experimental investigation of enhanced SPP coupling

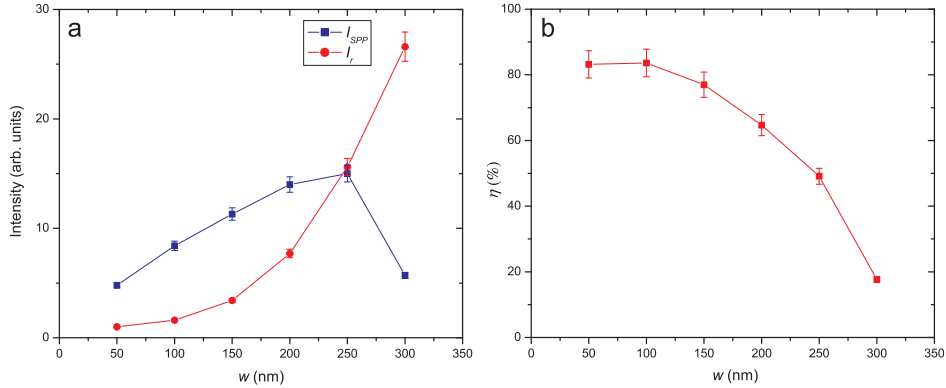


Figure 2.9: a) The time-averaged SPP intensity, I_{SPP} (blue squares), and time-averaged radiated intensity, I_r (red circles), and (b) the corresponding SPP coupling efficiency, η , as a function of w . The error bars describe the uncertainties in the measurement of I_{SPP} and I_r due to, respectively, the finite amount of I_r captured by D_1 and D_2 and the finite amount of I_{SPP} captured by D_3 .

2.3 Experimental investigation of enhanced SPP coupling

We next conduct a series of experiments to verify SPP coupling enhancement conferred by the addition of a dielectric layer. The experimental design is based on slit structures fabricated in an opaque silver film. The slits are flanked by two parallel grooves, placed at a distance s from the slit on the top surface of the silver film. The slit is illuminated from below using TM-polarized visible-light, and the top of the slit is viewed under an optical microscope. SPPs excited by the slit are incident onto the grooves and scattered from the metal surface into the far field. The SPPs scattered by the grooves are then captured and detected in the far field by an optical microscope. Other methods used in the literature to measure SPPs include leakage radiation microscopy and near-field optical microscopy [64–69]. Leakage radiation microscopy works by providing a pathway for SPPs to radiate from a metal surface, which is commonly achieved by surrounding one side of a thin metal film with a dielectric of higher refractive index than on the other side. SPPs radiated in a characteristic emission cone away from the metal surface are then captured by an oil-immersion optical microscope and identified by distinctive features in the Fourier plane of the microscope

image. Near-field optical microscopy, on the other hand, uses a nano-scale tip to locally sample the SPP fields and generates a SPP image by rastering the tip over a region near the defect site. We have chosen the slit-groove detection method here because it is simpler than the other methods and is feasible with the available equipment.

2.3.1 Fabrication

We build the devices by sequentially evaporating a 5- nm-thick chromium adhesion layer and then a 300- nm-thick, optically-opaque silver layer onto a glass substrate that is 200 μm thick. We use a mechanical surface profiler (Tencor P10 profiler), with a vertical resolution of 1 \AA , to verify the targeted thickness of the silver films and quantify surface roughness. The measured thickness of the silver films is 300 ± 5 nm and the average surface roughness is $R_a \leq 3$ nm. We fabricate a series of slits having a fixed length of 3 μm and widths ranging between $100 \text{ nm} \leq w \leq 300 \text{ nm}$ using a FEI Dual Beam Strata-235 focused ion beam (FIB) system. The FIB system is a high-vacuum particle microscope/mill that uses Ga^+ ions with high kinetic energy to locally bombard the sample and ablate material. The lower bound of the slit width is set by the milling resolution of the FIB tool and the upper bound is set by the restriction that the dielectric-filled slit sustains only the lowest order mode (which was confirmed by performing FDTD simulations of plane-wave, normal incidence illumination of the slit having a variable width and then visually corroborating that the simulated field structure in the slit was consistent with that of the lowest order mode; see for example, the simulations depicted in Fig. 2.10). Each slit is flanked by two parallel grooves placed 1 μm on both sides from the edges of the slit. The grooves have a depth of $\simeq 100$ nm, a width of $\simeq 200$ nm, and a length of 2 μm . We create 6 identical sets of slits and grooves, each on its own separate glass substrate. Five of the substrates are spin-coated with a layer of PMMA ($n = 1.49$), with layer thicknesses varying from 60 nm to 140 nm in increments of 20 nm. The remaining substrate is left uncoated and serves as an experimental control. Based on surface profiler (Tencor P10 profiler) measurements, we find that the achieved PMMA layer thicknesses are within ± 4 nm of their nominal thickness.

2.3.2 Experimental design

The optical response of the structure is characterized by illuminating the bottom of the structure through the glass slide with TM-polarized col-

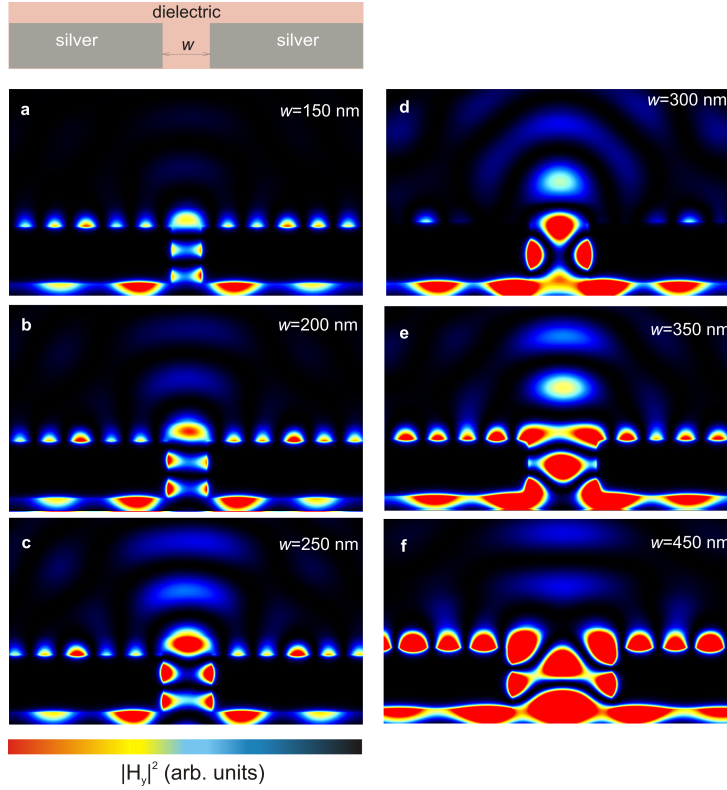


Figure 2.10: Simulation procedure to determine an upper bound for the slit width, for an arbitrary set of parameters, when the slit is filled with a dielectric and loaded with a dielectric layer. Image of the FDTD-calculated instantaneous $|H_y|^2$ distribution for a slit illuminated by a quasi-plane-wave of wavelength $\lambda_0 = 500$ nm when the slit width is (a) 150 nm, (b) 200 nm, (c) 250 nm, (d) 300 nm, (e) 350 nm, and (f) 450 nm. Dispersion-less glass with the refractive index of 1.5 is used as the dielectric. The dielectric layer thickness $d = 100$ nm is held constant. Note the transition of the field profile in the slit as the slit width increases.

limited He-Ne laser beam at a wavelength $\lambda_0 = 632.8$ nm and viewing the top of the structure under an optical microscope (Zeiss Axio Imager) with a $100\times$ objective lens, as shown in Fig. 2.11(b). At the chosen visible wavelength, the experimental range of dielectric layer thickness values is expected to yield a range of SPP momentum values that spans the momentum of light in the dielectric (shown in Fig. 2.11(a)). The complex k_{spp} values are calculated by solving the dispersion relation of a semi-infinite three-layer silver-glass-air waveguide, where the permittivity of silver is fitted to experimental data [70]. We examine the structure under illumination with light that is TM- or x-polarized (electric field perpendicular to the slit axis) and TE- or y-polarized (electric field along the slit axis). Due to the natural TM polarization of SPPs as discussed in Chapter 1, a slit illuminated with TE-polarized light does not sustain SPP coupling, whereas a slit illuminated with TM-polarized light produces a SPP beam emanating from the slit perpendicular to the slit axis. The experiment is designed so that SPPs scattered by the grooves produce a bright spot in the resulting microscope image at the groove location. Due to the placement of the grooves on the transmission side of the optically-opaque metal film, the grooves should be visible only when they are illuminated by SPPs propagating along the metal surface and are otherwise invisible. It is noted that the detection of radiated SPPs from isolated grooves is fundamentally different than the detection methodology used in leakage radiation microscopy, which allows SPPs to freely radiate from the metal surface at any location.

2.3.3 SPP measurement

One of the immediate challenges of measuring SPPs coupled from a slit using transmission-mode optical microscopy is the isolation of weak SPP signatures from light diffracted through the slit. In the absence of the polymer layer, the microscope image of the slit region [Fig. 2.12(a)] under x-polarized illumination is dominated by a diffraction pattern from the slit consisting of a bright main lobe centered on the slit with subsidiary lobes spanning several microns to the side of the slit. Any light scattered from the groove locations is disguised by the side lobes of the diffraction pattern, precluding unambiguous identification of SPPs by direct observation. The overwhelming diffraction from the slit can be mitigated by adding a polymer layer, which is predicted to better match the momentum of SPPs with the momentum of light and enhance SPP coupling efficiency. With the addition of a 80-nm-thick polymer layer, the microscope image of the slit region [Fig. 2.12(b)] now reveals distinctive SPP signatures as bright spots at the

2.3. Experimental investigation of enhanced SPP coupling

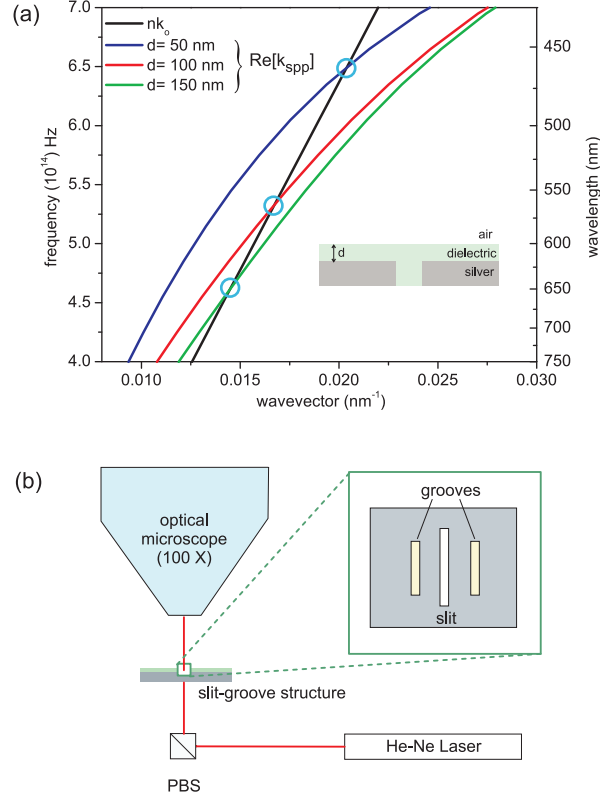


Figure 2.11: (a) $\text{Re}[k_{spp}]$ corresponding to SPP modes propagating along a silver metal surface coated with a dielectric layer of refractive index $n = 1.5$ and surrounded by air, for various layer thickness values, along with the nk_0 line. Complex k_{spp} values are calculated by solving the dispersion relation of a semi-infinite three-layer silver-glass-air waveguide, where the permittivity of silver is fitted to experimental data. The circles highlight, for a given dielectric layer thickness, the frequency at which the momentum matching condition $\text{Re}[k_{spp}] = nk_0$ is satisfied. It should be noted that the momentum matching condition is an approximation and provides only a first-order procedure to estimate the optimal dielectric layer thickness. (b) Schematic of the experimental set-up. Polarized light from a He-Ne laser ($\lambda_0 = 632.8$ nm) illuminates the sample and the far-field transmission image is captured by an optical microscope (Zeiss Axio Imager) using a $100\times$ objective lens with a numerical aperture of 0.90 in air ambient and recorded using a Si CCD camera.

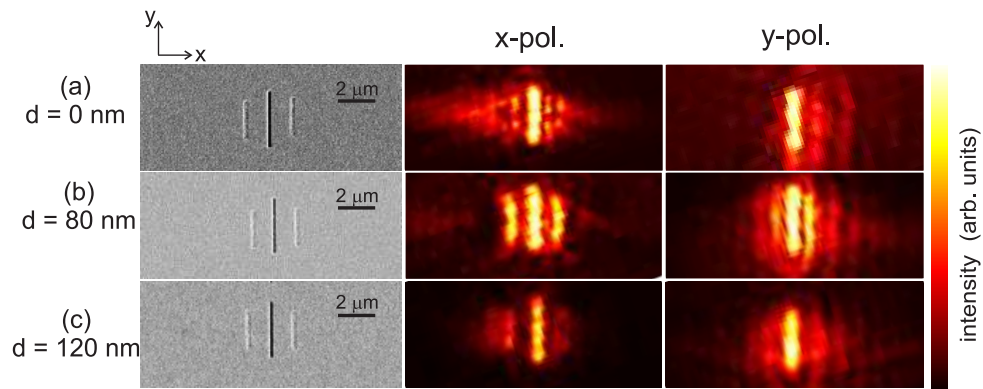


Figure 2.12: Representative microscope images of the slit and grooves for (a) an uncoated sample, (b) a coated sample with PMMA layer thickness $d = 80$ nm, and (c) a coated sample with PMMA layer thickness $d = 120$ nm. The width of the slits is $w = 150$ nm. The left column shows scanning electron microscope (SEM) images, and the middle and right columns show optical microscope images under x-polarized and y-polarized illumination, respectively. The color of the optical microscope images has been modified for clarity, but the images are otherwise unprocessed.

groove locations. The bright spots have an intensity comparable to that of the main lobe of the diffraction pattern from the slit, indicating that a significant portion of the light in the slit couples into SPPs. The momentum matching conferred by the polymer layer is highly sensitive to the layer thickness. As the polymer layer thickness increases to 120 nm, the intensity of the bright spots at the groove locations reduces and it again is difficult to distinguish the diffraction pattern from SPP signatures at the groove locations [Fig. 2.12(c)]. Comparative microscope images under y-polarized illumination show similar diffraction patterns, albeit without any SPP signatures at the groove location, regardless of the presence of the polymer layer or its thickness.

We next quantitatively determine the SPP coupling efficiency. A comparative experiment is designed consisting of two identical slits of width $w = 150$ nm and length $3 \mu\text{m}$, aligned and off-set along the direction of the slit axis so that the transmission through the slits are independent. Grooves are created on both sides of slit 1 [top slit in Fig. 2.13(a)], spaced $s = 1 \mu\text{m}$ from the center of the slit, while the metal surface adjacent to slit 2 [bottom slit in Fig. 2.13(a)] is left pristine. Figure 2.13(b) shows a microscope image of the slits under x-polarized illumination. By comparing the images of the slits, image artifacts due to diffraction from the slit and SPP scattering from the grooves can be separated. For example, subtraction of the region of the microscope image encompassing the slit without the grooves (R2) from the region encompassing the slit and the grooves (R1), yields a resulting image in which the diffraction from the slit is suppressed and SPP signatures from the grooves are isolated. Under y-polarized illumination, the same subtraction procedure yields an image without any observable SPP signatures [Fig. 2.13(c)].

We use the brightness of different portions of the microscope image of the slit and grooves to measure the SPP coupling efficiency. The brightness of the slit is proportional to the amount of light that diffracts and radiates from the slit exit. The brightness of the grooves is proportional to the amount of light that has converted into SPPs at the slit exit and radiates upon striking the grooves. We define the quantities $I_{g,L}$ and $I_{g,R}$ as the integrated intensity over a region encompassing the left and right grooves, respectively, the quantities $I_{ng,L}$ and $I_{ng,R}$ as the integrated intensity over a region spaced $s = 1 \mu\text{m}$ to the left and right of slit 2, respectively, and the quantity I_s as the integrated intensity over a region encompassing exit side

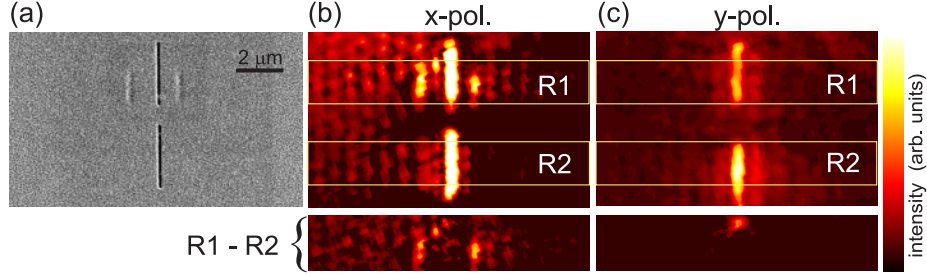


Figure 2.13: Experiment to distinguish diffraction from a slit and SPP scattering from adjacent grooves. (a) SEM image of a representative sample consisting of two identical slits of width $w = 150$ nm, one of which is flanked by grooves. The sample is coated with a PMMA layer of thickness $d = 80$ nm. Optical microscope image of the sample under (b) x-polarized illumination and (c) y-polarized illumination. We apply a subtraction procedure to images (b) and (c) in which the region R2 is subtracted from R1. The resulting subtracted image derived from (b) show bright spots at the groove location indicative of SPP scattering. These bright spots are absent in the subtracted image derived from (c), suggesting the absence of SPPs.

of slit 2. The SPP coupling efficiency is now defined as

$$\eta = \frac{I_{g,L} + I_{g,R} - I_{ng,L} - I_{ng,R}}{I_s + I_{g,L} + I_{g,R} - I_{ng,L} - I_{ng,R}} \times 100\%, \quad (2.13)$$

where the numerator describes the intensity contributions to the image due to SPP scattering from the grooves and the denominator describes the intensity contributions to the image due to both SPP scattering from the grooves and diffraction from the slit. The efficiency as defined in Eq. (2.13) describes, to a good approximation, the fraction of light at the slit exit that couples into SPPs. The intensities used in the Eq. (2.13) to experimentally measure the SPP coupling efficiency are consistent with the time average intensities Eq. (2.11 and 2.12), which are used for the calculation of SPP coupling efficiency in the simulation. For the representative case depicted in Fig. 2.13 where $w = 150$ nm and $d = 80$ nm, an efficiency of $\eta = 52 \pm 6\%$ is measured, considerably higher than the efficiency value (20%) previously reported for nano-slits [44, 60], which do not use the dielectric coating technique described here.

2.3.4 SPP coupling efficiency measurements

The measured results of SPP coupling efficiency as a function of the polymer layer thickness yields the efficiency curve shown in Fig. 2.14(a). The coupling efficiency has a sharp peak at a layer thickness of 80 nm, nearly six times higher than the efficiency without the layer. The measurements are compared with numerical two-dimensional FDTD simulations of x-polarized illumination (at $\lambda_0 = 632.8$ nm) of a slit in a metal film for discrete d values ranging from 0 to 200 nm. For fair comparison, we conduct another set of simulations for a simulation structure that is identical to the experiments consisting of a slit flanked by two grooves.

We extract η from the simulations by directly measuring the SPP intensity at the metal surface and light intensity radiated from the slit. Similar to the experimentally-measured efficiency, the FDTD-calculated efficiency peaks at a layer thickness of 80 nm. Two observations suggest that the enhanced coupling is due to momentum matching. First, the experimental and simulated efficiency plots both peak at a d value that agrees, within a factor of 2, to the d value predicted to satisfy $\text{Re}[k_{spp}] \simeq nk_0$ using the simplistic design procedure described in Fig. 2.11(a), which assumed a momentum of light in the slit describable by nk_0 . Second, the experimental and simulated efficiency plots both drop-off for d values slightly off the optimal value. The drop-off in the simulated η for $d > 80$ nm is not as sharp as that observed in the experiments. We attribute this discrepancy to surface roughness present in the experiment but absent in the simulations. Due to the tighter confinement of SPPs near the surface for increasing d (which can be inferred from the dispersion diagrams in Fig. 2.11(a)), losses due to surface roughness should be more pronounced for thicker polymer layers and is evident in the efficiency plots. Over the range from $150 \text{ nm} \leq w \leq 300 \text{ nm}$, we observe good agreement between the experimentally-measured and FDTD-calculated SPP coupling efficiencies as a function of the slit width (Fig. 2.14(b)). Over this slit width range (which corresponds to a normalized range of $0.24 \leq w/\lambda_0 \leq 0.47$), similar reductions in the SPP coupling efficiency as a function of slit width were theoretically predicted in Ref. [56] using a semi-analytical model of geometrical diffraction from a slit in an infinitely thick Au medium followed by SPP launching on an adjacent flat Au surface. It should be noted that the error in the experimentally-measured SPP coupling efficiency for the thinnest slit width $w = 100$ nm is larger due to weak transmission through the slit.

2.3. Experimental investigation of enhanced SPP coupling

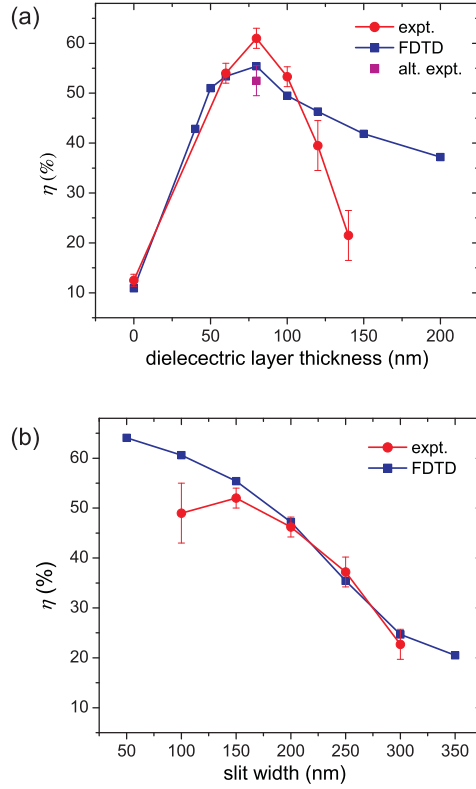


Figure 2.14: (a) SPP coupling efficiency, η , as a function of the PMMA layer thickness, for a fixed slit width of $w = 150$ nm. η is measured using two methods. In the first method, labeled “expt-1”, η is calculated by using $I_{ng,L}$ and $I_{ng,R}$ derived from the image of the slit and grooves under y-polarized illumination and then using Eq. (2.13) (red circles). In the second method, labeled “expt-2”, η is calculated by using $I_{ng,L}$ and $I_{ng,R}$ derived from the image of the slit with no grooves under x-polarized illumination and then using Eq. (2.13) (magenta diamond). We calculate η from two-dimensional FDTD simulations modeling x-polarized plane-wave illumination of a coated slit for various d values (blue squares). We also calculate, for the optimal case of $d = 80$ nm, the SPP coupling efficiency when a 20-nm-deep dimple is present in the dielectric layer above the slit (cyan square), which emulates possible non-planarity of the polymer layer due to conforming to the slit walls. (b) shows the SPP coupling efficiency measured using the method “expt-1” (red circles) and calculated using FDTD simulation (blue squares) as a function of the slit width. The error bars in (a) and (b) correspond to the variance of five independent measurements.

2.3. Experimental investigation of enhanced SPP coupling

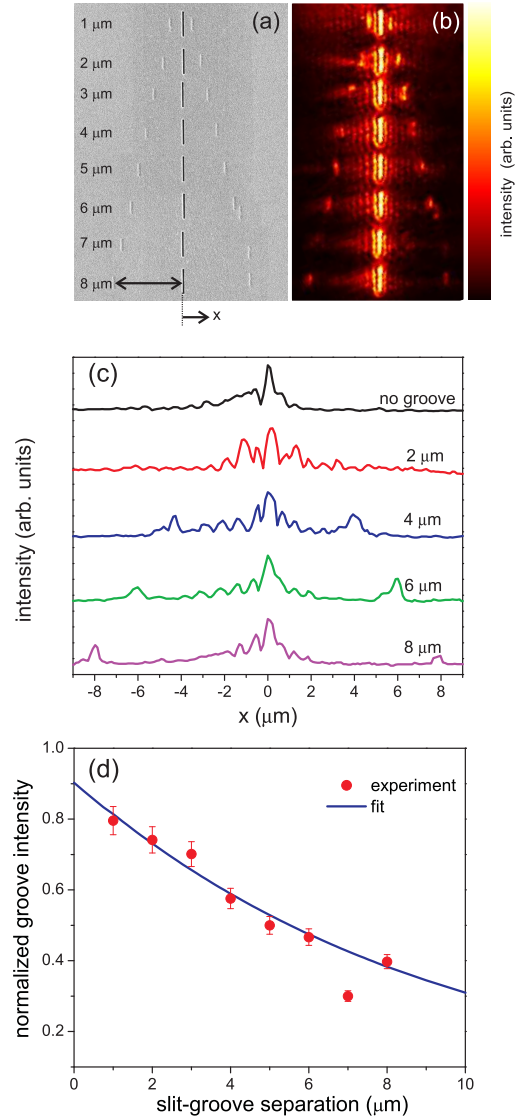


Figure 2.15: (a) SEM image of an array of identical $w = 150$ nm slits where the groove spacing from the slits is varied from $s = 1 \mu\text{m}$ to $s = 8 \mu\text{m}$ in $1 \mu\text{m}$ increments. The array is coated with a PMMA layer of thickness $d = 80$ nm. (b) shows the corresponding microscope image of the array. (c) depicts profiles of the image intensity along horizontal lines intersecting the slit and grooves for various slit-groove separation values. (d) The integrated SPP intensity normalized to the integrated intensity of the slit as a function of the slit-groove separation (red circles), where the blue line corresponds to an exponential fit.

2.3.5 SPP propagation distance measurements

Next, we measure SPP propagation distance to reassure that the groove brightness is resulted due to the scattering of the SPP modes. We use a single snapshot in the vicinity of the slit under the optical microscope to calculate the SPP propagation distance. We demonstrate this by creating a linear array of 8 identical slits [shown in Fig. 2.15(a)] of width $w = 150$ nm and length $3 \mu\text{m}$, again aligned and off-set along the direction of the slit axis so that the transmission through the slits are non-interfering. Pairs of grooves are then milled next to the slits, where the slit groove spacing, s , varies from 1 to $8 \mu\text{m}$ in $1 \mu\text{m}$ increments. A 80 nm-thick polymer layer is then applied to the device. The entire array encompasses an area of approximately $20 \mu\text{m} \times 50 \mu\text{m}$, well within the field of view of laboratory-grade microscopes using a $100\times$ objective lens. The array is illuminated by x-polarized light and a microscope image of the entire array is captured [Fig. 2.15(b)]. In addition to the expected diffraction pattern emerging from the slits, the array image contains bright spots at the groove locations, which diminish as s increases but are still visible for the largest ($s = 8 \mu\text{m}$) slit-groove separations. Analysis of the image yields line plots, shown in Fig. 2.15(c), of the intensity distribution along the x direction, from which SPP signatures can be clearly identified as intensity spikes amidst a background diffraction pattern. An exponential fit to the intensity of the SPP signature as a function of slit-groove separation [Fig. 2.15(d)] yields an intensity decay constant of $9.35 \mu\text{m}$, which is in good agreement with the expected intensity decay constant $\alpha = 1/(2\text{Im}[k_{spp}]) = 9.26 \mu\text{m}$ extracted from the imaginary part of the SPP wave vector for $d = 80$ nm, $n = 1.5$, and $\lambda_0 = 632.8$ nm. This agreement reinforces that the groove brightness arises from groove illumination by SPP modes, rather than by higher-order guided modes in the polymer layer (which are expected to be cutoff at $\lambda_0 = 632.8$ nm for $d = 80$ nm).

Massively-parallel SPP measurements can potentially be performed by imaging large two-dimensional arrays, composed of hundreds or thousands of slit-groove structures, under a conventional microscope. The maximum number of slit-groove structures that can be accommodated using this technique is dependent on the field-of-view of the microscope, the length of the slits, and the minimum separation distance between slits, which must be greater than the SPP decay constant to ensure minimal cross-talk. For example, a microscope with a $100 \mu\text{m}$ field-of-view could image approximately 250 slits, assuming a slit length of $2 \mu\text{m}$ and a separation distance between slits of $20 \mu\text{m}$, chosen to accommodate a SPP decay constant of $10 \mu\text{m}$.

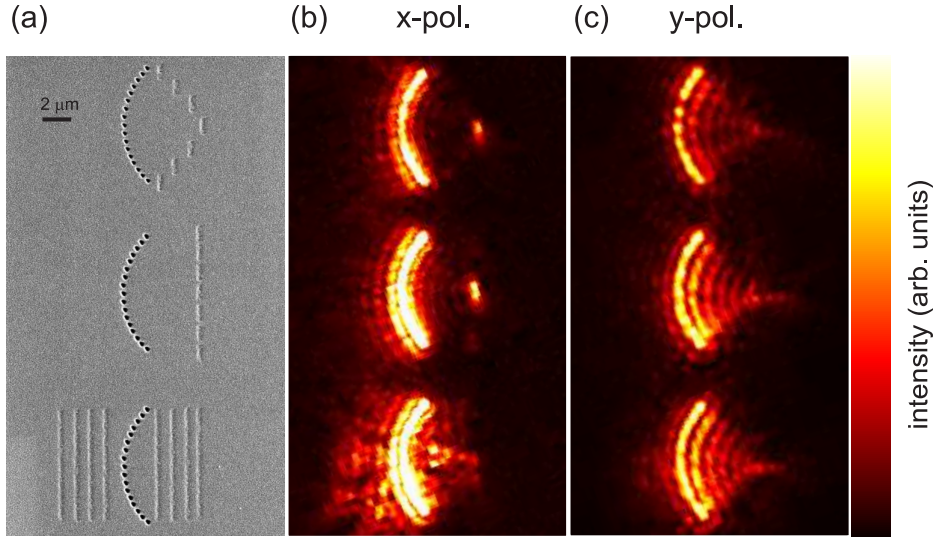


Figure 2.16: Measurement of a focused SPP beam emitted from a curved array of sub-wavelength holes using optical microscopy. (a) SEM image of three plasmonic lenses consists of a curved array of holes, with different groove patterns milled adjacent to the lenses. The lenses consist of 17 holes, each of diameter $\simeq 200$ nm, milled into a semi-circle of radius $5 \mu\text{m}$. Optical microscope image of the three lenses under (b) x-polarized illumination and (c) y-polarized illumination.

2.3.6 SPP lensing using an array of holes

We next use optical microscopy to revisit the SPP lensing experiment described in Ref. [51], in which a focused SPP beam emitted from a curved array of subwavelength holes is measured using near-field scanning optical microscopy. Assuming that the momentum of light in a dielectric-filled sub-wavelength hole is the same as in a dielectric-filled sub-wavelength slit (that is, describable by nk_0), the aforementioned principles of momentum matching should also apply here. We fabricate three identical, off-set semi-circular lens arrays consisting of 17 holes, each with a diameter of $200 \text{ nm} < \lambda_0$, arranged into a semi-circle of radius $5 \mu\text{m}$. To enhance SPP coupling from the holes to SPPs, the entire array is coated with an 80-nm-thick polymer layer. As shown in Fig. 2.16(a), we create different groove patterns next to the arrays to probe different aspects of the SPP beam. The groove pattern next to the top lens probes the confinement of the SPP beam within

the cone defined by the arc angle of the array; the groove pattern next to the middle lens measures the SPP distribution at the focal plane; the groove pattern next to the bottom lens is expected to disrupt any SPP lensing effects. The image of the top and middle lens arrays under x-polarized illumination reveals a single sharp, bright spot at the groove located at the focus (Fig. 2.16(b)). The absence of SPP signatures at any of the other grooves means that the SPP beam from the lens array is confined within the cone and focused onto a single point in the focal plane, consistent with the results from Ref. [51]. As expected, SPP focussing is absent from the image of the bottom lens array. Under y-polarized illumination, the three lens arrays produce similar diffraction patterns, with no pronounced groove signatures to indicate SPP focussing (Fig. 2.16(c)).

2.4 Broadband enhancement of SPP coupling

Although metallic surfaces can generally support SPPs at frequencies below the plasma frequency, it is challenging to efficiently and compactly couple to SPPs at the same time over a broad frequency range. This capability, however, would be potentially useful for the development of integrated plasmonic devices, broadband photovoltaic devices, and optical information processing devices that use wavelength multiplexing. In recent years, there has been several research reports [71–79] of SPP excitation in devices designed specifically to enable coupling over a broad frequency range. This has been achieved, for example, using periodic or aperiodic slit arrays [72, 73, 79] or a single dielectric coated asymmetric nano-slit [77]. Similar to the observations by Chen et al. (this work was conducted in the near-infrared showing a 100 nm SPP coupling bandwidth ranging from 710 nm to 810 nm while considering just a single dielectric layer thickness), we have observed in our FDTD simulations previously shown that broadband SPP excitation in the visible is possible by coating a sub-wavelength slit with a thin dielectric layer. In this section, we will experimentally verify this prediction by measuring the broadband SPP coupling from slit-groove structures illuminated with incoherent white light spanning approximately a 200 nm bandwidth from 480 nm up to 680 nm.

2.4.1 Fabrication

Test samples are fabricated by successive sputtering of a 5-nm-thick adhesion layer of Cr followed by an optically opaque 300-nm-thick layer of Ag at a deposition rate of 1 Å/s onto a glass microscope slide. For each

sample, two 20- μm -long slits of identical width ($w = 100\text{ nm}$) are milled into the metallic film using focused ion beam (FIB) milling. The extra long slits are employed in these studies to facilitate spectral measurements using the spectrometer. In the region adjacent to the slits, we mill two grooves, each with a length of 22 μm and depth of 100 nm, parallel to the slit edges placing them each side of the slit. The grooves are placed to scatter SPPs from the metal surface into the far-field, which provides a measurable signal to quantify SPPs. For one slit (labeled “sample 1”), the groove spacings from the edges of the slit are $s = 3\ \mu\text{m}$ and $s = 6\ \mu\text{m}$, and for the other slit (labeled “samples 2”), the groove spacings are $s = 8\ \mu\text{m}$ and $s = 10\ \mu\text{m}$. We create three identical sets of each sample: one of each sample is left uncoated and serves as an experimental control, another of each sample is spin-coated with a 160-nm-thick layer of PMMA, and the last of each sample is spin-coated with a 300-nm-thick layer of PMMA. Based on additional simulations, which are not shown, it is predicted that the slits coated with a 160 nm thick PMMA layer will exhibit broadband SPP coupling enhancement over the visible. This enhancement is predicted to be absent when the slits are coated with the thicker 300 nm PMMA layer.

2.4.2 Experimental design

Broadband SPP coupling from the slits is measured using the setup shown in Fig. 2.17 (a). We illuminate the structures at normal incidence with incoherent white light provided by a tungsten lamp and polarized into the TM configuration using a broadband linear polarizer. Note that the incoherence of the incident light is not modeled by our previous FDTD simulations, which assume a perfectly coherent incident wave. The light incident on the slit generates SPPs, which propagate along the silver/PMMA interface and are scattered by the grooves. The top of the slit structure is then imaged using a far-field optical microscope (Zeiss Axioimager) with a 100 \times objective lens with a numerical aperture of 0.9. Color images of the slit structures are captured by a camera in the image plane. To make spectra measurements, the camera is removed and a fibre-optic collector of a visible-frequency spectrometer (sensitive to a wavelength range from 400 nm to 800 nm) samples a portion of the image plane. Figure 2.17 (b, top) shows the spectrum of the beam sampled by the spectrometer when the slit structure is removed, providing a good representation of the light spectrum incident onto the slit. With a slit structure mounted on the microscope stage, positioning the fibre collector at the location of the image of the slit yields the spectra shown in Figure 2.17 (b, bottom). Similar slit transmission spectra are

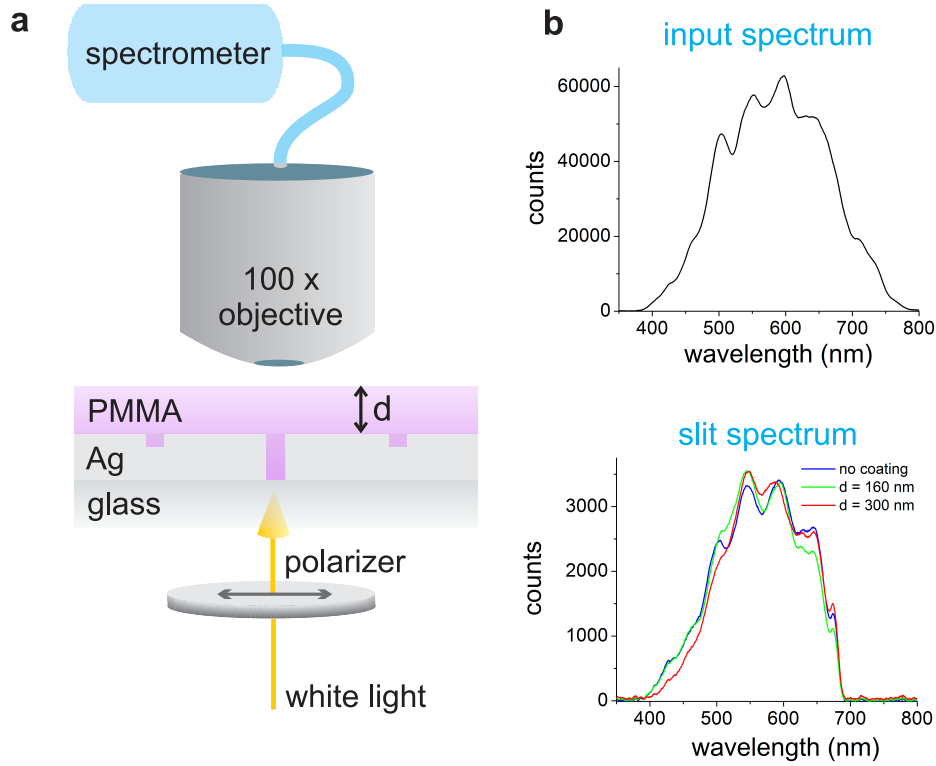


Figure 2.17: (a) Experimental setup to characterize broadband SPP coupling using a slit-groove structure. Light from a tungsten light source is directed through a polarizer and is incident onto the slit structure. An image of the top of the slit structure is collected by a $100\times$ objective lens with numerical aperture of 0.9. The spectral data are collected by a spectrum analyzer, which is placed in the image plane of the microscope. (b, top) Spectrum of the light that is supplied from the tungsten source and (b, bottom) transmitted through the various slit structures.

measured for the coated and uncoated slits.

2.4.3 Results

The experimental results collected for coated and uncoated versions of sample 1 and sample 2 are summarized in Figures 2.18 and 2.19, respectively. We first extract the intensity profiles across the slit-groove structures from color images taken with the microscope, normalizing the peak intensities to unity (shown in panel (b) of Figures 2.18 and 2.19). The profiles reveal a consistent variation of the groove brightness between the various coated and uncoated samples; for any given groove location on either of the samples, the groove brightness is highest for samples coated with a 160-nm-thick PMMA layer, followed by uncoated samples, and then samples coated with a 300-nm-thick layer. We next analyze the spectral distribution of the SPP signal collected from the grooves (shown in panels (c) and (d) of Figures 2.18 and 2.19). For spectral measurement, we subtract the baseline noise signal from the raw spectral data. The measured SPP spectra span from approximately 420 nm to 680 nm, encompassing nearly the entire visible range. Adding a 160-nm-thick PMMA layer provides a uniform, broadband enhancement of the SPP signal compared to control measurements for the uncoated samples. This enhancement is observed for both samples at all sampled distances from the slit. Increasing the PMMA layer thickness to 300 nm significantly reduces the SPP signal compared to the control measurements, confirming that the thickness of the PMMA layer must be carefully tailored to achieve SPP enhancement over a large spectral range. To quantify the effect of the PMMA coating on the SPP intensity coupled from the slit, we take the ratio of the SPP spectra with and without the coating and plot the spectral ratio for the various groove locations (shown in panels (e) and (f) of Figures 2.18 and 2.19). We consistently observe that the presence of the 160 nm PMMA layer leads to an increase in the SPP intensity by a factor ranging approximately from 1.2-2.0 over most of the visible spectrum. On the other hand, adding the 300 nm PMMA layer results in a general reduction of the SPP intensity.

2.5 Summary

We have proposed and demonstrated a simple method for enhancing the efficiency of slit-coupling from a free-space plane-wave into SPPs on a metal film. The key element of the coupling scheme involves an ultra-thin

2.5. Summary

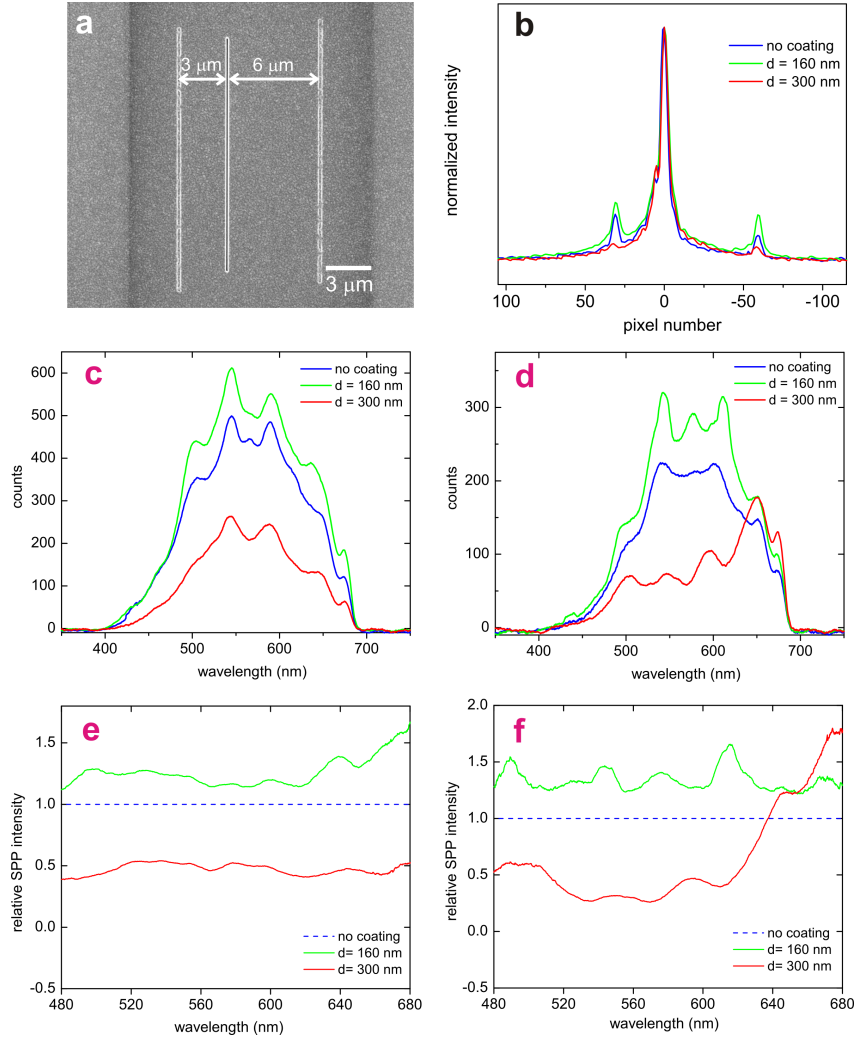


Figure 2.18: (a) SEM image of a slit-groove structure with slit-to-groove separation distances of $3\ \mu\text{m}$ and $6\ \mu\text{m}$. (b) Normalized intensity profile measured in the horizontal direction across the slit and grooves extracted from a transmission-mode microscope image of the structure shown in (a). (c) and (d) show the spectra collected by sampling at slit-to-groove separation distances of $3\ \mu\text{m}$ and $6\ \mu\text{m}$. (e) and (f) plot the ratio of the groove spectra of the coated samples to that of the uncoated samples for measurements taken at slit-to-groove separation distances of 3 and $6\ \mu\text{m}$.

2.5. Summary

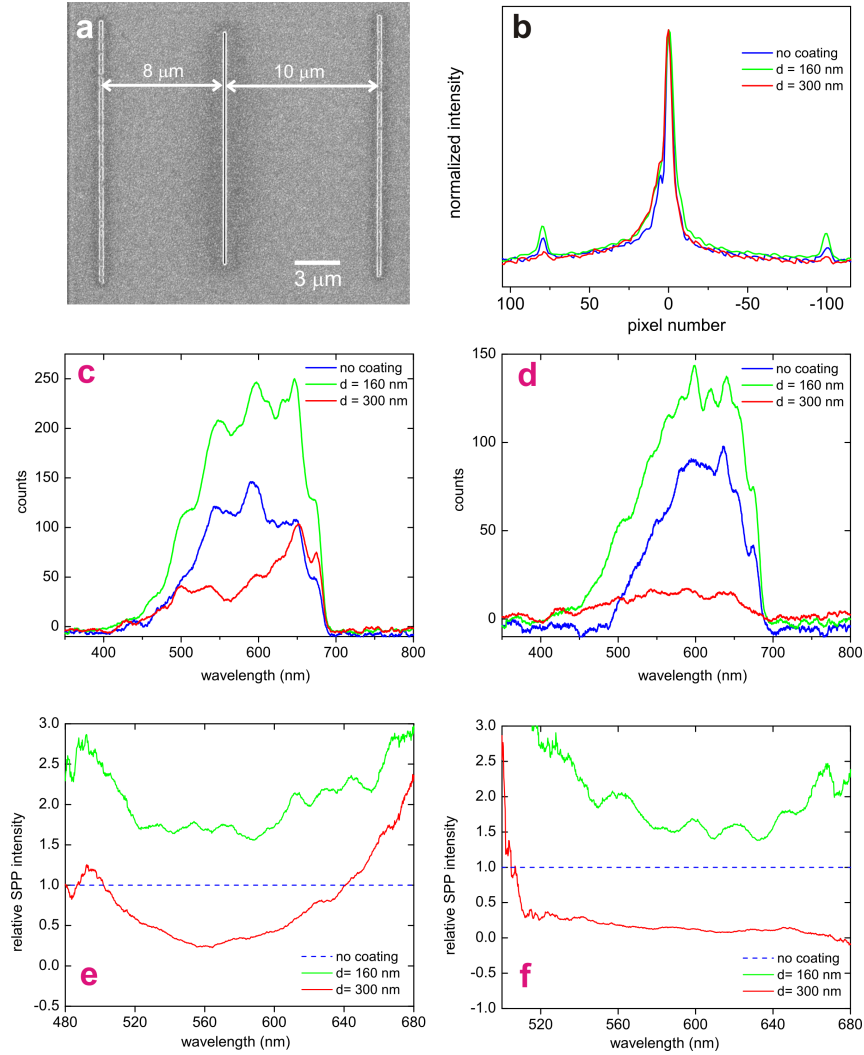


Figure 2.19: (a) SEM image of a slit-groove structure with slit-to-groove separation distances of $8 \mu\text{m}$ and $10 \mu\text{m}$. (b) Normalized intensity profile measured in the horizontal direction across the slit and grooves extracted from a transmission-mode microscope image of the structure shown in (a). (c) and (d) show the spectra collected by sampling at slit-to-groove separation distances of $8 \mu\text{m}$ and $10 \mu\text{m}$, respectively. (e) and (f) plot the ratio of the groove spectra of the coated samples to that of the uncoated samples for measurements taken at slit-to-groove separation distances of 8 and $10 \mu\text{m}$, respectively.

2.5. Summary

dielectric layer placed on the exit side of the metal film. Varying the thickness of the dielectric layer enables tuning of the SPP wave vector. When a thickness is selected which yields wave vector matching, the SPP coupling efficiency is enhanced by several times relative to that without the layer. This has been demonstrated both through numerical simulations using the FDTD method and experimental measurements. The experiments were implemented by fabricating slit-groove structures and visualizing their optical response under a microscope. The enhanced coupling efficiency conferred by the addition of the layer results in SPP signatures that are visible under naked-eye inspection through an optical microscope and appear as distinctive bright spots located at the groove scatterers. This method can be used to perform parallel SPP measurement, which we have demonstrated using a linear array of slits and grooves, and can be extended for massively-parallel SPP measurement using larger two-dimensional arrays accommodating the entire microscope field-of-view. A SPP lensing experiment previously performed using near-field optical microscopy has also been re-visited here using optical microscopy. We have also experimentally shown that broadband enhancement of SPP coupling from a sub-wavelength slit can be achieved over most of the visible spectrum with the same technique. In addition to enhancing SPP coupling efficiency, the method of using a thin dielectric layer has the added benefit of passivation and protection of the SPP-sustaining metal surface. The enhanced SPP excitation through a sub-wavelength slit can be useful to realize nanoscale integration of photonic structures. The results also show the potential of miniaturization of SPP bio-chemical sensor in nano-scale.

Chapter 3

Improving the SPP Coupling Efficiency Near a Super-wavelength Slit

Nearly all studies of surface plasmon polariton (SPP) coupling from apertures have restricted the aperture size to less than the wavelength of light in the surrounding dielectric. Why is this so? One reason may be that smaller apertures offer greater potential for miniaturization, which supports the long-term goal of making compact information devices based on SPPs. Another, more practical reason is that smaller apertures are easier to analyze. Since the original diffraction theories of Kirchhoff and Bethe [5, 80], it has been widely assumed that the fields in a small aperture can be described as a constant - an assumption now known as the single-mode approximation [13, 31, 32, 56, 81]. With the majority of efforts thus far focused on the study of sub-wavelength apertures, it may be worth questioning if small aperture dimensions are a necessary condition for efficient SPP generation and whether or not bigger apertures, for the purpose of SPP coupling, can be better.

Previous studies on SPP excitation from large apertures suggest that efficient SPP coupling can be achieved even when the aperture size exceeds the wavelength [59]. Renger et al. theoretically calculated the SPP scattering cross section in the vicinity of isolated grooves and slits as a function of aperture size spanning sub-wavelength and super-wavelength regimes and found an oscillatory dependence. For aperture sizes exceeding the wavelength, this behavior was correlated to the presence of higher order modes in the aperture, although no causal mechanism linking higher order modes to the SPP scattering cross section was offered in this work. Later, Kihm et al. [60] experimentally measured the SPP coupling efficiency from small and large slits in air using a near-field scanning optical microscope and also found an oscillatory slit-width dependence. The authors applied a simple scalar diffraction model using the single-mode approximation – which precludes

the possibility of higher order modes – and found qualitative agreement with their experimental data, despite the questionable validity of the single mode approximation for super-wavelength slit values.

The goal of this chapter is to investigate SPP coupling from large apertures to reveal how higher order modes in the aperture interact with SPPs, by using the simple model of SPP coupling in which the slit and surrounding metallic surface are treated like independent, semi-infinite waveguides. We adopt the standard configuration consisting of a single slit in a metal film immersed in a dielectric with refractive index n , illuminated with transverse-magnetic polarized light. As in Chapter 2, we adopt a slit configuration, as opposed to a hole, because it can be analyzed in two dimensions and provides the most basic system to understand the physics of SPP coupling. Our hypothesis is that the onset of higher order modes in a slit - brought on by increasing the slit width w beyond the wavelength - boosts the lateral spatial frequency components in the slit, so that a larger portion of light directly couples to SPPs by wave vector matching [63]. Intuitively, the boost in the spatial frequency components for larger slit widths is associated with the transition of the least-attenuated mode in the slit from the lowest order TM_0 mode, which has no nodes across its field profile, to the higher order TM_1 mode, which has two nodes, as shown in Fig. 3.1. It is interesting to note that the TM_0 mode in a metal-dielectric-metal waveguide converges to the transverse electromagnetic (TEM) mode of a parallel plate perfect electric conductor in the limit that the conductivity of the metal approaches infinity [82]. In this Chapter, we will show that by judicious selection of the surrounding refractive index, a super-wavelength slit can couple to SPPs with efficiency comparable to or even greater than that of a sub-wavelength slit.

3.1 Hypothesis: enhanced SPP coupling due to higher-order modes

Consider a semi-infinite layer of metal (silver) with relative permittivity ϵ_m that extends infinitely in the x - and y -directions and occupies the region $-t < z < 0$. A slit of width w oriented parallel to the z -axis and centred at $x = 0$ is cut into the metal film. The metal film is immersed in a homogeneous dielectric medium with relative permittivity ϵ_d and refractive index $n = \sqrt{\epsilon_d}$. The slit is illuminated from the region below it with a TM-polarized electromagnetic plane wave of wavelength $\lambda = \lambda_0/n$ and wave vector $\vec{k}_p = k\hat{z}$, where $k = 2\pi/\lambda$. The $+z$ -axis defines the longitudinal

3.1. Hypothesis: enhanced SPP coupling due to higher-order modes

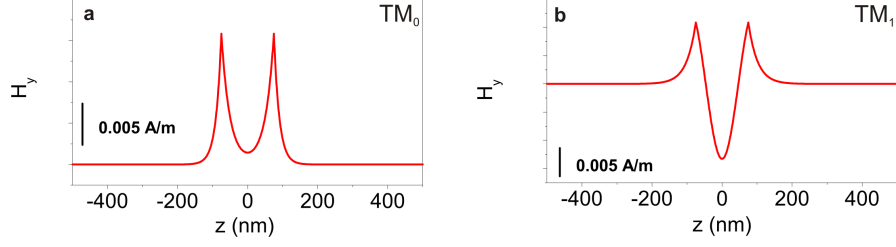


Figure 3.1: Magnetic field profiles of the (a) TM_0 and (b) TM_1 modes at $\omega_0 = 6.0 \times 10^{14}$ Hz in an infinite metal-dielectric-metal (MDM) waveguide having a dielectric core thickness $w = 150$ nm. Silver is used as the metal and the core consists a dielectric of index 2.5. The field profiles are normalized so that the modes carry unit power in the upward direction.

direction, and the x -axis defines the transverse axis. The electromagnetic wave couples into a guided mode in the slit having complex wave vector $\underline{k}_x = \underline{k}_z \hat{z} + \underline{k}_x \hat{x}$, where \underline{k}_z and \underline{k}_x are the longitudinal and transverse components of the complex wave vector, respectively. The attenuation of the guided mode in the slit can be characterized by a figure of merit (FOM) defined as

$$\text{FOM} = \frac{|\text{Re}[\underline{k}_z]|}{|\text{Im}[\underline{k}_z]|}, \quad (3.1)$$

where $\text{FOM} \gg 1$ describes a propagating mode. When the guided mode exits the slit, electromagnetic energy is coupled into plane-wave modes and $\pm x$ -propagating SPP modes. The SPP modes have complex wave vector $\pm \underline{k}_{spp} \hat{x}$, where $\text{Re}[\underline{k}_{spp}]$ and $\text{Im}[\underline{k}_{spp}]$ describe the spatial periodicity and attenuation, respectively, of the SPP field along the transverse direction.

The slit structure can be conceptually divided into two regions - (a) the region before the slit exit can be approximated as an infinite metal-dielectric-metal (MDM) waveguide along the x -direction, and (b) the dielectric region above the metal surface. A SPP coupling scheme based on the slit structure is designed by first mapping \underline{k}_z and \underline{k}_x of the TM_0 and TM_1 modes sustained in the slit for varying slit width. The longitudinal wave vector components \underline{k}_z of the TM_0 and TM_1 modes in the slit are calculated by solving the exponential and oscillatory forms of the complex eigenvalue equation [60], respectively, for an infinite MDM waveguide using the Davidenko method with an iterative solving scheme [83]. Details of this procedure as used in this work can be found in the Master's thesis of Waqas Maqsood, a colleague with whom I collaborated [84]. The parameter ϵ_m is modeled by fitting to

3.1. Hypothesis: enhanced SPP coupling due to higher-order modes

experimental data of the real and imaginary parts of the permittivity of silver [70], and ϵ_d is assumed to be real and dispersion-less. Figure 3.2(a) shows FOM curves for TM₀ and TM₁ modes in slits of varying width for the representative case where the slit is immersed in a dielectric with a refractive index $n = 1.75$. The FOM values for the TM₀ modes are largely insensitive to variations in the slit width and gradually decrease as a function of increasing frequency. FOM curves for the TM₁ modes are characterized by a lower-frequency region of low figure of merit and a higher-frequency region of high figure of merit, separated by a knee located at a cutoff frequency. The cutoff slit width w_c for the TM₁ mode at a given frequency ω is the threshold slit width value below which the TM₁ mode is attenuating. At a fixed visible frequency $\omega = 6.0 \times 10^{14}$ Hz ($\lambda = 285$ nm), $w_c \sim 300$ nm. The least attenuating mode in the slit can be identified at a particular frequency and slit width by the mode with the largest FOM. The TM₀ mode is dominant for $w < w_c$, and the TM₁ mode is dominant for $w > w_c$.

The real part of the transverse wave vector component, $\text{Re}[\underline{k}_x]$, of the guided mode in the slit describes the component of electromagnetic momentum in the transverse plane parallel to the plane of the metal surface and exists in the dielectric core of the slit. Values of \underline{k}_x are obtained from the relation

$$\underline{k}_x = \sqrt{k^2 - \underline{k}_z^2}, \quad (3.2)$$

where $k = nk_0$ is the magnitude of the wave vector in the dielectric core of the slit. Note that \underline{k}_x assumes a different value in the metallic portions of the slit. Figure 3.2(b) shows $\text{Re}[\underline{k}_x]$ values over the visible-frequency range for the TM₀ mode in a slit of width $w = 200$ nm and for the TM₁ mode in slits of widths $w = 350$ nm and $w = 500$ nm. At the frequency $\omega = 6.0 \times 10^{14}$ Hz, $\text{Re}[\underline{k}_x]$ for the TM₀ mode in the $w = 200$ nm slit is nearly two orders of magnitude smaller than $\text{Re}[\underline{k}_x]$ for the TM₁ mode in the $w = 350$ nm and $w = 500$ nm slits. Values of $\text{Re}[\underline{k}_x]$ for the TM₁ mode generally increase for decreasing slit width. Given the parameters in Fig. 3.2(b) and for a fixed $\omega = 6.0 \times 10^{14}$ Hz, $\text{Re}[\underline{k}_x]$ for the TM₁ mode increases from 8.5×10^6 m⁻¹ to 1.3×10^7 m⁻¹ as the slit width decreases from 500 nm to 350 nm.

At this point, we propose a simple physical picture of SPP excitation by a slit aperture in terms of a three-step process (similar, in principle, to the theoretical work proposed in Ref. [56, 57]): 1) guided modes carry electromagnetic energy through the slit, 2) when the guided modes encounter the slit edges, they diffract into a continuum of spatial frequencies (extrapolated to the far-field, the propagating parts of this spatial frequency continuum produce a characteristic far-field diffraction pattern), and 3) some of these

3.1. Hypothesis: enhanced SPP coupling due to higher-order modes

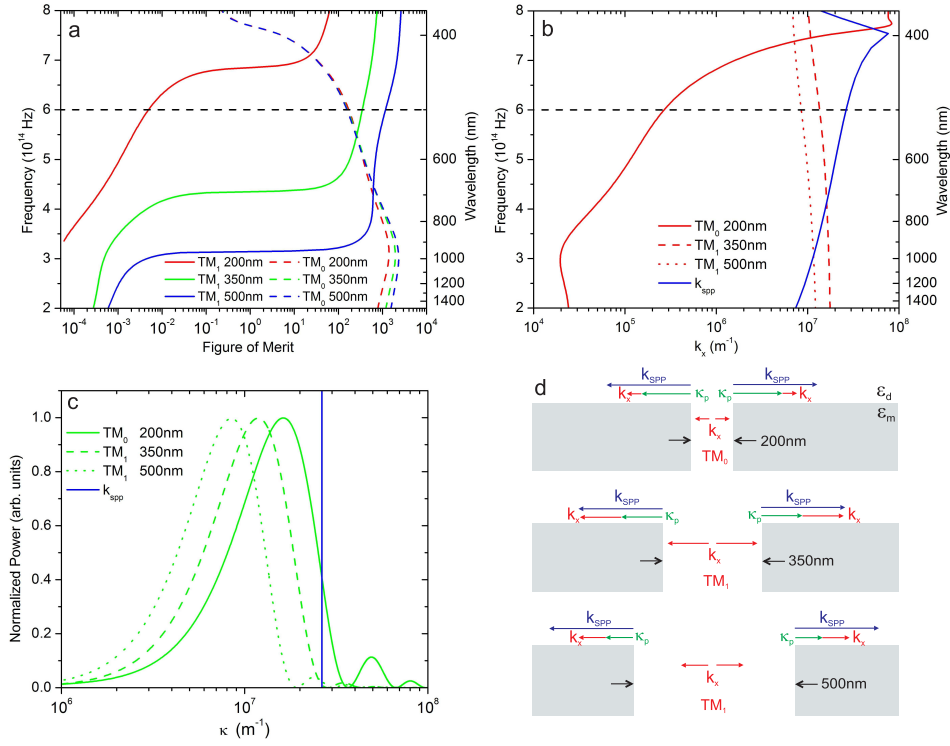


Figure 3.2: Formulation of a hypothesis for diffraction-assisted SPP coupling by a super-wavelength slit aperture. (a) Figure-of-merit and (b) the real transverse wave vector component versus frequency and wavelength for TM_0 and TM_1 modes sustained in slits of different widths. (c) Diffraction spectrum corresponding to the TM_0 mode in a 200-nm-wide slit and the TM_1 modes in 350 nm-wide and 500 nm-wide slits. (d) Wave vector-space depiction of diffraction-assisted SPP coupling from slits of width $w = 200$ nm, $w = 350$ nm, and $w = 500$ nm, immersed in a uniform dielectric of refractive index $n = 1.75$

3.1. Hypothesis: enhanced SPP coupling due to higher-order modes

diffracted modes are phase-matched to the SPP wave vector and excite SPPs at the surface adjacent to the slit exit. In the previous paragraphs, we have already discussed the guided modes and their wave vector components $\text{Re}[\underline{k}_x]$ and $\text{Re}[\underline{k}_z]$. Next, we examine the diffraction process at the slit exit, which generates a distribution of transverse spatial frequency components, κ , commonly called the diffraction spectrum. Relying on scalar diffraction theory and the work of Kowarz [9], we can approximate the diffraction spectrum by Fourier transformation of the transverse field profiles of the guided mode right at the slit exit. Figure 3.2(c) shows the normalized diffraction spectrum for slit widths $w = 200$ nm, $w = 350$ nm, and $w = 500$ nm, at a fixed frequency $\omega = 6.0 \times 10^{14}$ Hz. The peak transverse spatial frequency component, κ_p , is the spatial frequency at which the diffraction spectrum peaks, which is close to, but does not exactly match $\text{Re}[\underline{k}_x]$ of the guided mode. For the parameters in Fig. 3.2(c), κ_p shifts from 1.6×10^7 m⁻¹ to $\kappa_p = 8.3 \times 10^6$ m⁻¹ as the slit width increases from $w = 200$ nm to $w = 500$ nm, indicating a spatial frequency boost due to diffraction as the slit width increases. It is noteworthy that $\kappa_p < \text{Re}[\underline{k}_{spp}]$ for all slit width values.

We propose a simple picture of diffraction-assisted SPP coupling in which SPP coupling at the slit exit is mediated by diffraction of the guided mode, yielding a net real transverse wave vector component $\text{Re}[\underline{k}_x] + \kappa_p$. Coupling from the diffracted mode at the slit exit to the SPP mode adjacent to the slit exit is optimized when the wave vector-matched condition $\text{Re}[\underline{k}_x] + \kappa_p = \text{Re}[\underline{k}_{spp}]$ is satisfied. This proposed phase matching condition is similar to the more-established (and experimentally verified) equation governing SPP coupling from a grating, which is given by $k_0 n \sin(\theta) \pm mg = \text{Re}[\underline{k}_{spp}]$, where n is the index of the dielectric, θ is the angle of incidence, m is an integer corresponding to the diffraction order, and g is the grating spatial frequency. The proposed equation for coupling through a large slit is similar to the equation for grating coupling because both take into account contributions from a wave vector component of an incident wave and a spatial frequency contribution due to scattering. There are, however, some subtle differences. Whereas the grating coupling equation considers an incident plane wave, we now have an incident guided mode. Moreover, whereas the grating coupling equation considers scattering from a periodic grating, which produces a discrete spectrum of spatial frequencies spaced by g , we now have mode scattering from the slit exit, which produces a continuous spectrum that can be described, by good approximation, through scalar diffraction theory applied to an aperture.

Let's examine why this picture is particularly suitable to describe SPP coupling from a larger slit. Because $\text{Re}[\underline{k}_{spp}]$ is generally larger than both

3.1. Hypothesis: enhanced SPP coupling due to higher-order modes

$\text{Re}[k_x]$ and κ_p , large and commensurate contributions from both $\text{Re}[k_x]$ and κ_p are required to fulfill wave vector matching. In a sub-wavelength slit, the TM_0 mode has $\text{Re}[k_x] \ll \kappa_p$ and SPP coupling at the slit exit requires a sufficiently small slit width to generate large diffracted spatial frequency components to match with $\text{Re}[k_{spp}]$. On the other hand, a super-wavelength slit sustains a TM_1 mode with $\text{Re}[k_x] \simeq \kappa_p$. The large contributions of $\text{Re}[k_x]$ to the net real transverse wave vector component reduces the required contributions from κ_p needed for wave vector matching. As a result, wave vector matching with the SPP mode adjacent to the slit exit can be achieved with a relatively large slit aperture. This proposed SPP coupling process is presented in Fig. 3.2(d) based on the data in Figs. 3.2(a)-(c) for $w = 200$ nm, $w = 350$ nm and $w = 500$ nm at a fixed $\omega = 6.0 \times 10^{14}$ Hz.

It is important to note that the proposed hypothesis of SPP coupling from a slit provides a plausible physical interpretation that is easy to understand but highly approximate in nature. Here, SPP excitation is the result of two contributions, one from the transverse wave vector component of the incident guided modes and another from the transverse spatial frequency component, κ_p , associated with the diffracted guided mode after it encounters the slit edges. At first glance, it may appear that there is double counting of the contribution of $\text{Re}[k_x]$ - it is relied upon to describe both the intrinsic lateral momentum of the guided mode and also contributes in the calculation of the diffraction spectrum of the diffracted mode. However, the intrinsic lateral momentum of the guided mode and momentum due to scattering are physically independent effects - one arises from the nature of the guided mode and the other from the interaction of that mode with a structural discontinuity. In this case, the structural discontinuity is an abrupt termination of the waveguide which allows the guided mode profile itself to be used to approximate the diffraction process. In the case of a grating, for example, the structural discontinuity is a periodic spatial function which gives rise to a discrete diffraction spectrum. It is also possible to estimate the spatial frequencies of the diffracted guided mode by numerically calculating the field profile after the guided mode has scattered from the slit edges, but this relies on numerical simulation and provides less physical insight. In the absence of any work to provide a meaningful physical interpretation of slit coupling to SPPs in the super-wavelength regime, we should keep in mind that our goal here is to formulate a plausible, physically insightful hypothesis that can be analytically calculated and tested. Going forward, it is now possible to evaluate the coupling condition and then measure or simulate the SPP coupling efficiency to determine if the coupling condition succeeds in predicting SPP coupling maxima.

3.2 Simulation design

We postulate that enhanced SPP coupling efficiency provides evidence of wave vector matching between the SPP wave vector and the wave vector of the incident guided mode, boosted by diffraction from the slit exit.. SPP coupling efficiency of a slit immersed in a dielectric is modeled using finite-difference-time-domain (FDTD) simulations. The simulation grid has dimensions of 4000×1400 pixels with a resolution of 1 nm/pixel and is surrounded by a perfectly-matched layer to eliminate reflections from the edges of the simulation space. The incident beam is centered in the simulation space at $x = 0$ and propagates in the $+z$ -direction, with a full-width-at-half-maximum of 1200 nm and a waist located at $z = 0$. The incident electromagnetic wave has a free-space wavelength $\lambda_0 = 500$ nm and is TM-polarized such that the magnetic field, H_y , is aligned along the y -direction.

Control variables of this study include the type of metal (chosen as silver), the thickness of the metal layer (set at $t = 300$ nm), the polarization of the incident electromagnetic wave (TM), the angle of incidence of the incident electromagnetic wave (normal), and the wavelength of the incident electromagnetic wave ($\lambda_0 = 500$ nm). The independent variables include the width of the slit, w , which varies from 100 to 800 nm, and the refractive index of the surrounding dielectric n , which varies from 1.0 to 2.5. The dependent variables are the time-averaged intensity of the SPP modes coupled to the metal surface at the slit exit, I_{SPP} , the time-averaged intensity of the radiated modes leaving the slit region, I_r , and the SPP coupling efficiency, η . The dependent variables are quantified by placing line detectors in the simulation space to capture different components of the intensity pattern radiated from the exit of the slit, similar to the method employed in Chapter 2. The I_{SPP} detectors straddle the metal/dielectric interface, extending 50 nm into the metal and $\lambda_0/4$ nm into the dielectric region above the metal, and are situated adjacent to the slit exit a length λ_0 away from the edges of the slit. The I_r detector captures the intensity radiated away from the slit that is not coupled to the surface of the metal. The coupling efficiency is then calculated by the equation

$$\eta = \frac{I_{SPP}}{I_{SPP} + I_r} \times 100\%. \quad (3.3)$$

3.3 Simulation results

The numerical simulations provide evidence of high-throughput and high-efficiency SPP coupling from a slit of super-wavelength width. Figure 3.3

3.3. Simulation results

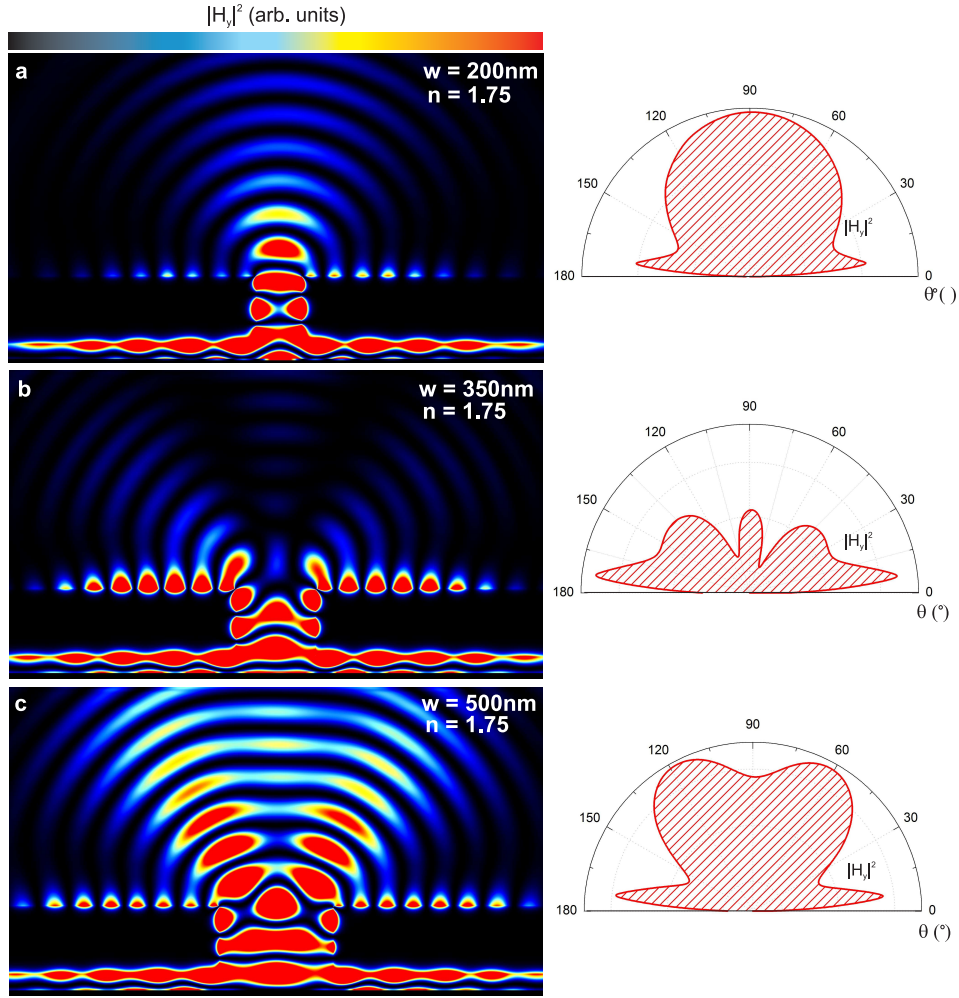


Figure 3.3: Images of the FDTD-calculated instantaneous $|H_y|^2$ distribution (left) and the time-averaged $|H_y|^2$ angular distribution (right) for a slit of width values (a) $w = 150\text{ nm}$, (a) $w = 350\text{ nm}$, and (a) $w = 500\text{ nm}$ immersed in a dielectric ($n=1.75$) and illuminated by a quasi-plane-wave of wavelength $\lambda_0 = 500\text{ nm}$. A common saturated color scale has been used to accentuate the fields on the exit side of the slit.

3.3. Simulation results

displays representative snap-shots of the instantaneous $|H_y|^2$ intensity and time-averaged $|H_y|^2$ angular distribution calculated from FDTD simulations for plane-wave, TM-polarized, normal-incidence illumination of a slit immersed in a dielectric ($n = 1.75$) for slit width values $w = 200$ nm, $w = 350$ nm, and $w = 500$ nm. Radiative components of the field in the dielectric region above the slit propagate away from the metal-dielectric interface, and plasmonic components propagate along the metal-dielectric interface. For $w = 200$ nm [Fig. 3.3(a)], the incident plane wave couples into a propagative TM_0 mode in the slit, which is characterized by intensity maxima at the dielectric-metal sidewalls. Diffraction of the TM_0 mode at the exit of the slit yields a relatively strong radiative component with an angular intensity distribution composed of a primary lobe centred about the longitudinal axis and a relatively weak plasmonic component. For $w = 350$ nm [Fig. 3.3(b)] and $w = 500$ nm [Fig. 3.3(c)], the incident plane wave couples primarily into the TM_1 mode in the slit, which is characterized by an intensity maximum in the dielectric core of the slit. The high-throughput SPP coupling is evident by the large SPP intensities observed for $w = 350$ nm. Diffraction of the TM_1 mode at the $w = 350$ nm slit exit yields a relatively weak radiative component with an angular intensity distribution skewed at highly oblique angles and a relatively strong plasmonic component. Further increasing the slit width to $w = 500$ nm increases the total throughput through the slit, but reduces the efficiency of SPP coupling. Diffraction of the TM_1 mode at the $w = 500$ nm slit exit yields a strong radiative component with an angular intensity distribution composed of two distinct side lobes and a relatively weak plasmonic component.

Trends in the SPP coupling efficiencies calculated from the FDTD simulations are compared to qualitative predictions from the model of diffraction-assisted SPP coupling described in Fig. 3.2. Figure 3.4(a) plots the FDTD-calculated SPP coupling efficiencies as a function of the optical slit width nw for dielectric refractive index values ranging from $n = 1.0$ to $n = 2.5$. For sub-wavelength slit width values $nw < \lambda_0$, highest SPP coupling efficiency is observed for the smallest optical slit width. This trend is consistent with diffraction-dominated SPP coupling predicted to occur for sub-wavelength slit widths, in which small slit width is required to yield large diffracted spatial frequencies to achieve wave vector matching. For super-wavelength slit width values $nw > \lambda_0$, the SPP coupling efficiencies exhibit periodic modulations as a function of optical slit width, qualitatively agreeing with the general trends observed in experimental data measured for a slit in air [60] and theoretical predictions based on an approximate model for SPP coupling from a slit [57]. The data in Fig. 3.4 reveals that the magnitude of

3.3. Simulation results

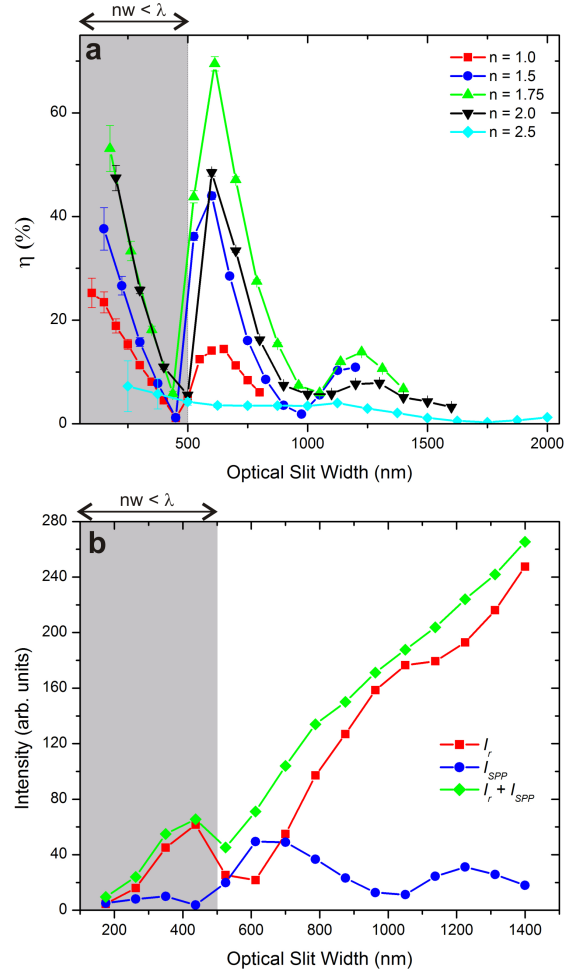


Figure 3.4: (a) SPP coupling efficiency as a function of optical slit width for dielectric refractive index values $n = 1.0$ (squares), $n = 1.5$ (circles), $n = 1.75$ (upright triangles), $n = 2.0$ (inverted triangles), $n = 2.5$ (diamonds). (b) The measured SPP intensity (circles), radiative intensity (squares), and total intensity (diamonds). The shaded region indicates the sub-wavelength-slit-width regime.

3.3. Simulation results

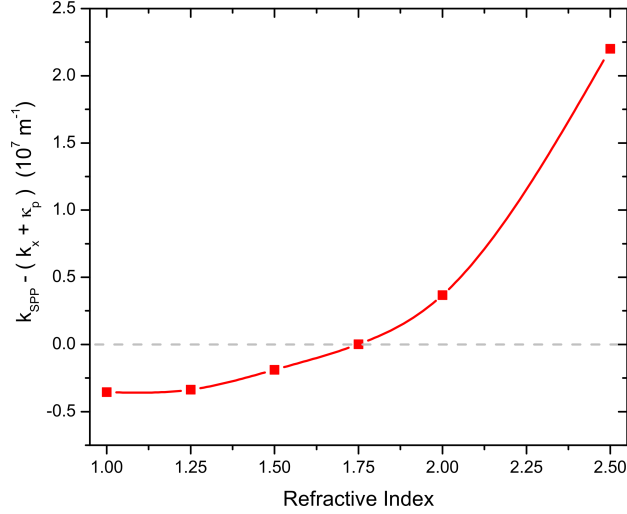


Figure 3.5: Wave vector mismatch as a function of refractive index of the dielectric region for a fixed optical slit width $nw = 600$ nm and free-space wavelength $\lambda_0 = 500$ nm.

the fluctuations in the SPP coupling efficiencies are highly sensitive to the dielectric refractive index. For refractive index values $n = 1.0, 1.5, 1.75,$ and 2.0 , the SPP coupling efficiency rises as nw increases above λ_0 and reaches local maxima of $\eta = 14\%, 44\%, 68\%$, and 48% at a super-wavelength optical slit width $nw \simeq 600$ nm, respectively. The rapid increase η as the slit width increases from sub-wavelength slit width values to super-wavelength slit width values is attributed to the disappearance of the TM_0 mode in the slit and the emergence of the TM_1 mode in the slit, which boosts the net real transverse wave vector component at the slit exit to enable wave vector matching. It is interesting to note that the SPP coupling efficiency peak at $nw = 600$ nm observed for lower refractive index values is absent for $n = 2.5$.

Figure 3.4(b) displays the time-averaged radiative intensity I_r , SPP intensity I_{SPP} , and total intensity $I_t = I_{SPP} + I_r$, as a function of the optical slit width for $n = 1.75$. Although the smallest optical slit width generally yields high SPP coupling efficiency, the total throughput and the SPP throughput is low. As the optical slit width increases to $w \simeq \lambda_0$ from sub-wavelength values, an increase in I_r and a decrease in I_{SPP} yield low SPP coupling efficiency. In the super-wavelength range of optical slit width values, $520 \text{ nm} < nw < 700 \text{ nm}$, concurrently high SPP throughput and high

3.4. Experimental design

SPP coupling efficiency ($\eta > 50\%$) are observed. For the optical slit width value $nw \simeq 600$ nm, I_{SPP} is about an order of magnitude larger than I_{SPP} for the smallest slit width value $nw = 175$ nm. As the optical slit width is further increased $nw > 700$ nm, I_r is significantly greater than I_{SPP} , resulting again in low SPP coupling efficiencies.

Variations in the peak SPP coupling efficiency at a fixed optical slit width $nw = 600$ nm for varying n can be qualitatively explained by the mismatch between the net real transverse wave vector component $\text{Re}[\underline{k}_x] + \kappa_p$ and the real SPP wave vector $\text{Re}[\underline{k}_{spp}]$. Figure 3.5 plots the transverse wave vector mismatch $\text{Re}[\underline{k}_{spp}] - (\text{Re}[\underline{k}_x] + \kappa_p)$ as a function of the dielectric refractive index at a constant optical slit width value $nw = 600$ nm. The wave vector mismatch increases monotonically from $-0.4 \times 10^7 \text{ m}^{-1}$ to $2.4 \times 10^7 \text{ m}^{-1}$ as the refractive index increases from $n = 1.0$ to $n = 2.5$, crossing zero at $n = 1.75$. Coincidence between the n value that yields peak SPP coupling efficiency at $nw = 600$ nm and that which yields zero wave vector mismatch supports the hypothesis that optimal SPP coupling efficiency occurs when $\text{Re}[\underline{k}_{spp}] = (\text{Re}[\underline{k}_x] + \kappa_p)$, and that this condition can be achieved using a super-wavelength slit aperture immersed in a dielectric. The relatively large wave vector mismatch for $n = 2.5$ is also consistent with the noted absence of a SPP coupling efficiency peak at $nw = 600$ nm.

3.4 Experimental design

In the previous section, it was shown through numerical simulations that a super-wavelength slit immersed in a dielectric can achieve SPP coupling efficiencies on the order of 60% by immersing the slit in a high-index dielectric medium $n \simeq 1.7 - 1.8$. The SPP coupling enhancement is highly sensitive to the width of the slit and the wavelength, and is believed to occur due to wave vector matching between the higher order modes in the slit and the adjacent SPP mode. Here, we pursue further validation of this concept by designing experiments, performing measurements, and running additional numerical simulations to quantify SPP coupling efficiency from large slit apertures and to understand the physical mechanism underlying this enhancement.

In contrast to the previous section which employed silver as the metallic surface, the experiment and simulations performed in this section will employ gold as the SPP-sustaining surface. It was discovered in early experimentation that silver reacts vigorously with the high-refractive index fluids to be used and severely tarnishes. Gold, on the other hand, remained inert. We expect that a super-wavelength slit in a gold film will show similar

3.4. Experimental design

SPP coupling enhancement as was previously shown for silver. Figure 3.6 highlights the frequency dependence of the wave vector components of the two lowest-order TM modes in a semi-infinite MDM waveguide (where the metal regions are gold and the dielectric is glass with $n = 1.5$). Note that the first order mode, which becomes dominant when the slit width is comparable to and larger than the wavelength, has a significantly larger lateral wave vector component compared to that of the lowest order mode. This lateral wave vector boost in the slit conferred by the first order mode is hypothesized to enable wave vector matching to the adjacent SPP mode and thus, high SPP coupling efficiency.

To experimentally verify this hypothesis, we fabricate test samples by first evaporating a 5-nm-thick adhesion layer of Cr followed by an optically opaque 300-nm-thick layer of Au onto a glass microscope slide. Pairs of 3- μm -long slits of identical width, aligned and off-set along the direction of the slit axis, are milled into the metallic film using focused ion beam (FIB) milling (using a FEI Strata Dual Beam 235). In the region adjacent to one of the slits, parallel, 2- μm -long, 200-nm-wide and 100-nm-deep grooves are milled 1 μm from the edges of the slit. The region adjacent to the other slit is kept pristine and serves as a local control. The width of the slit pairs is designed to range from 100 nm to 600 nm in steps of 50 nm. We vary the refractive index of the medium surrounding the slits over the range from 1.5 to 1.7, in steps of 0.1, by placing one of four transparent index fluids (Cargille Liquids) between the patterned Au film and a cover slip.

To measure the SPP coupling efficiency, we use an experimental configuration shown in Figure 3.7 consisting of a He-Ne laser, a polarizer and an optical microscope. The sample is illuminated by a TM-polarized (polarized with the electric field oriented perpendicular to the slit axis) beam ($\lambda_0 = 632.8 \text{ nm}$) from the transparent substrate side of the structure. We employ immersion microscopy in which a cover slip is placed on top of the high index liquid coating the slit structure and the gap between the cover slip and the objective lens is filled with silicone oil ($n = 1.4$). The slit-groove structures are then imaged with a 100 \times oil immersion lens with a numerical aperture of 1.3. SPPs excited near the slit apertures propagate along the Au-fluid interface and are scattered by the grooves, producing a tell-tale optical signal that is imaged in the far-field. Due to placement of the grooves on the transmission side of the optically-opaque metal film, the grooves should be visible only when they are illuminated by SPPs propagating along the metal surface and are otherwise invisible. The SPP coupling efficiency can be quantified, to good approximation, by analyzing the relative brightness of the region adjacent to the slits with and without grooves.

3.4. Experimental design

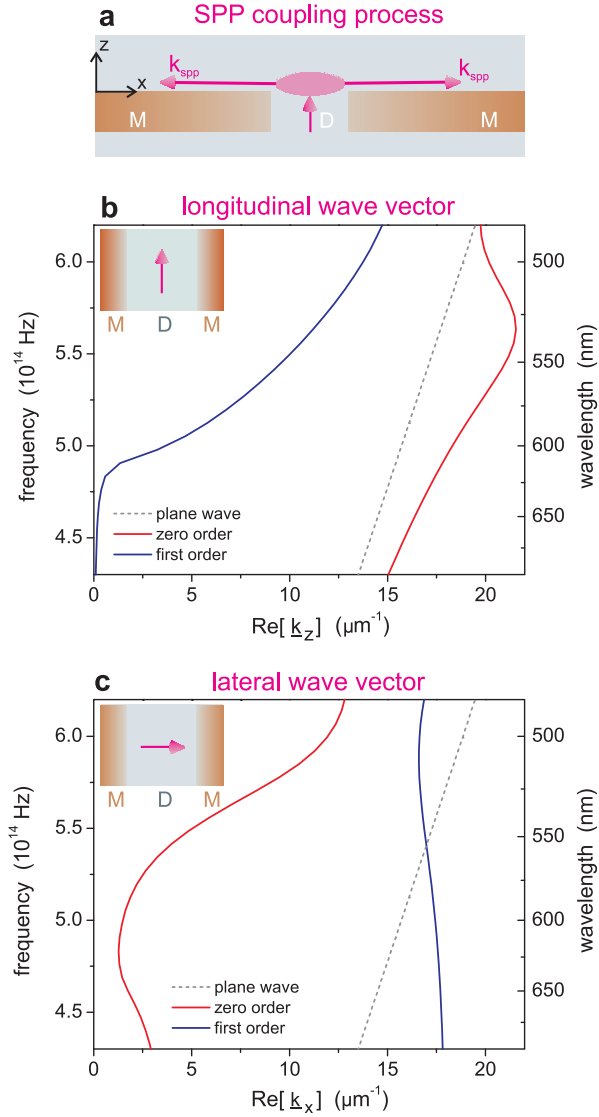


Figure 3.6: (a) SPP coupling from a slit in an opaque gold film. High-efficiency SPP coupling is achieved when the wave vector of light leaving the slit is wave vector matched with the SPP mode. Frequency dependence of the real parts of the (b) longitudinal and (c) lateral wave vector of the lowest-order modes in a Au-dielectric-Au waveguide, which approximates the slit structure. The refractive index of the dielectric is assumed to be 1.4. Note the large increase in the lateral wave vector of the first-order mode relative to that of the zero-order mode, which provides a wave vector boost needed for SPP coupling.

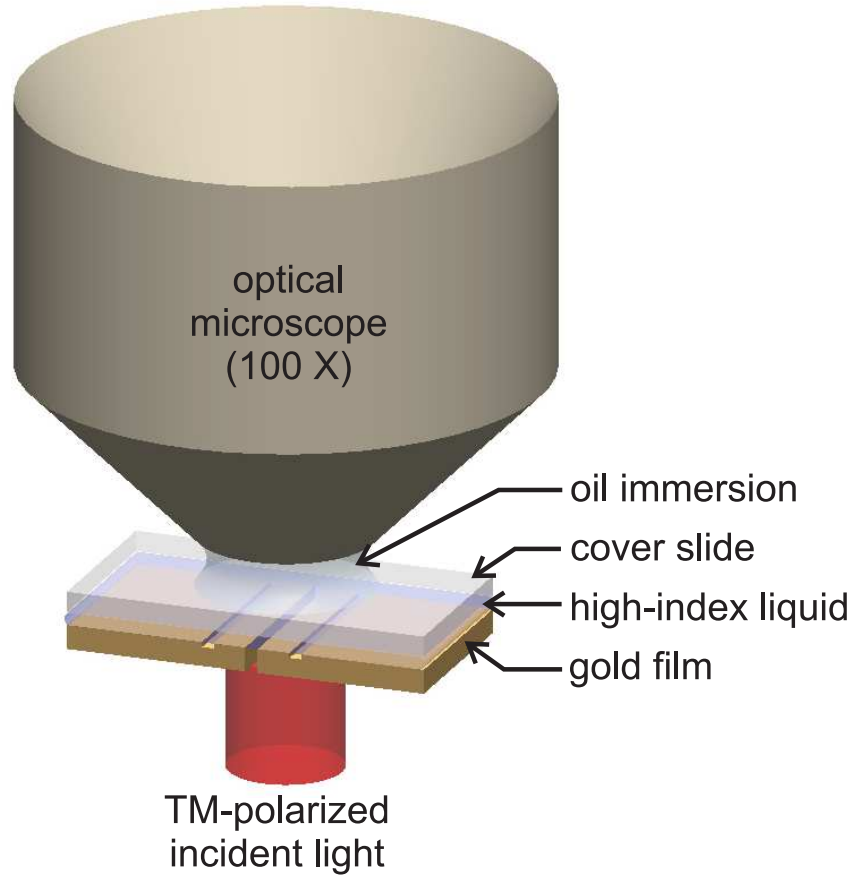


Figure 3.7: Schematic of the experimental set-up. The slit-groove structures etched into a gold film are immersed in a high-index fluid. TM-polarized light from a He-Ne laser ($\lambda_0 = 632.8$ nm) illuminates the sample and the far-field transmission image is captured using a CCD camera by oil immersion microscopy (100x objective lens and numerical aperture of 1.3). We place a cover slide and silicone oil successively on top of the high index fluid to avoid the possible damage of the eye-piece (as most of the high index fluid reacts).

3.4. Experimental design

Due to the spherical beam profile of the FIB, the fabricated slits acquire a tapered profile, as illustrated in a representative scanning electron microscope image of a slit in Figure 3.8. The width of the tapered region can be estimated from the high-brightness region of the SEM image of the slit edge [31]. For each of the fabricated slit pairs, we quantify the actual slit widths w_1 and w_2 corresponding to the width at the bottom and top of the metal film, respectively. As we are considering SPP coupling at the top surface of the metal film, we use w_2 as the true measurement of the slit width.

Figure 3.9 highlights the experimental analysis used to quantify the SPP coupling efficiency. Slits of identical width are fabricated on top of each other, where only one of the slits possesses adjacent grooves. The slits are then illuminated by TM-polarized laser light and an image of the slits is captured. We use the brightness of different portions of the microscope image of the slit and grooves to measure the SPP coupling efficiency. The brightness of the slit image is proportional to the amount of light that diffracts and radiates from the slit exit. The brightness of the image of the grooves is proportional to the amount of light that has converted into SPPs at the slit exit and radiates upon striking the grooves. We define the quantity I_g as the integrated intensity over a region encompassing the left and right grooves, respectively, the quantity I_{ng} as the integrated intensity over a region spaced $s = 1 \mu\text{m}$ to the left and right of slit 2, respectively, and the quantity I_s as the integrated intensity over a region encompassing exit side of slit 2. The SPP coupling efficiency is now defined as

$$\eta = \frac{I_g - I_{ng}}{I_s + I_g - I_{ng}} \times 100\%, \quad (3.4)$$

where the numerator describes the intensity contributions to the image due to SPP scattering from the grooves and the denominator describes the intensity contributions to the image due to both SPP scattering from the grooves and diffraction from the slit. The efficiency as defined in Eqn. 3.4 provides a reasonable approximation about the fraction of light at the slit exit that couples into SPPs.

Figure 3.10 highlights the simulation analysis used to quantify the SPP coupling efficiency. Here, we employ the FDFD method to model the electromagnetic response of the slits in a gold film. The FDFD method is used, as opposed to the FDTD method, because the Drude model used in FDTD does not accurately predict the imaginary part of the permittivity of gold at the operating wavelength of $\lambda_0 = 632.8 \text{ nm}$ (see Appendix for a comparison between the Drude model of the permittivity of gold and experimental

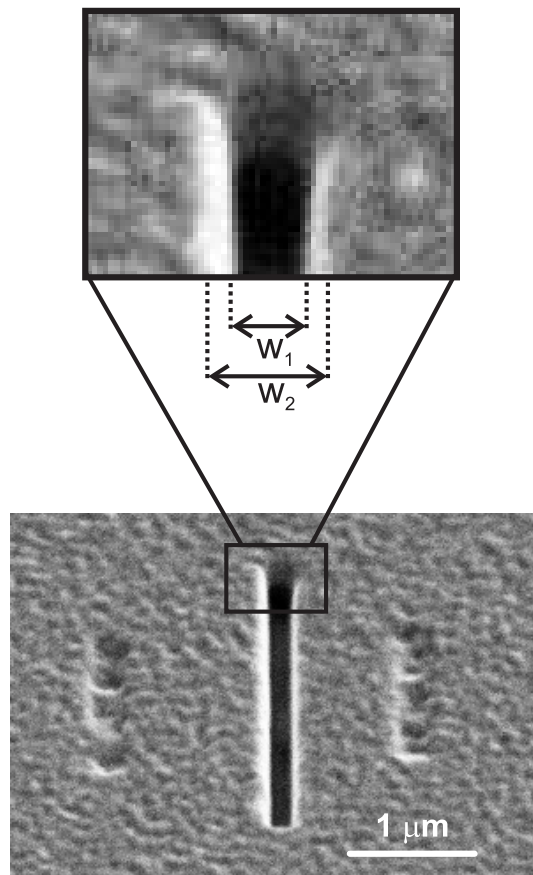


Figure 3.8: Scanning electron microscope of a typical slit structure etched into a 300-nm-thick Au film by focused ion beam milling. The whitish boundary at the edge of the slit represents the blunted slit edges resulting from bombardment of a spherical ion beam.

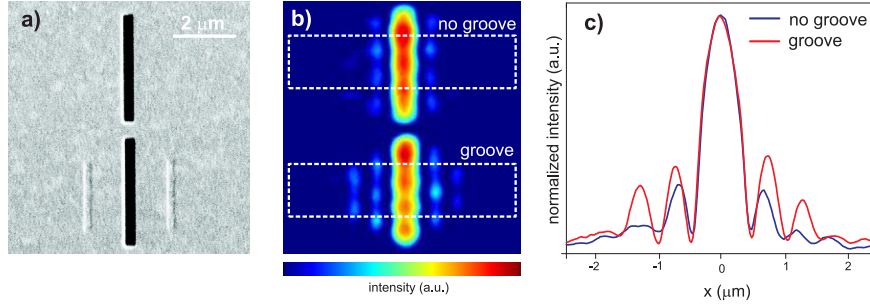


Figure 3.9: (a) Representative SEM image of a sample of two identical slit structures ($w = 450$ nm) where the bottom slit is flanked by two grooves. (b) The far field image of the sample when it is immersed in a high index fluid ($n = 1.7$). The color map of the optical microscope images has been modified for clarity, but the images are otherwise unprocessed. (c) The normalized intensity profile obtained from the area bounded by dotted boxes in (b). Note the enhanced light intensity of the side lobes next to the slit due to the presence of the grooves.

measurements). To measure the SPP coupling efficiency, we simulate the electromagnetic response of the slits (having identical tapered geometries as measured for the fabricated slits) under two conditions: one in which the metal region adjacent to the slit has grooves and another in which the metal region does not have grooves. To mimic the experimental measurement, we extract the time-averaged energy density across a plane that is 300 nm above the metal surface and approximates the object plane imaged by the microscope. A plot of the energy density profile is shown in Figure 3.10(c), which reveals increased intensity of the side lobe features adjacent to a primary peak due to the presence of the grooves. The observed side-lobe enhancement is similar to the experimental results shown in Figure 3.9(c). The SPP coupling efficiency is quantified from the simulated energy density profiles in a manner analogous to Eqn. 3.4.

3.5 Experimental SPP coupling efficiency measurements

The evolution of the SPP coupling efficiency as a function of slit width is shown in Figure 3.11, for three different values of the surrounding refrac-

3.5. Experimental SPP coupling efficiency measurements

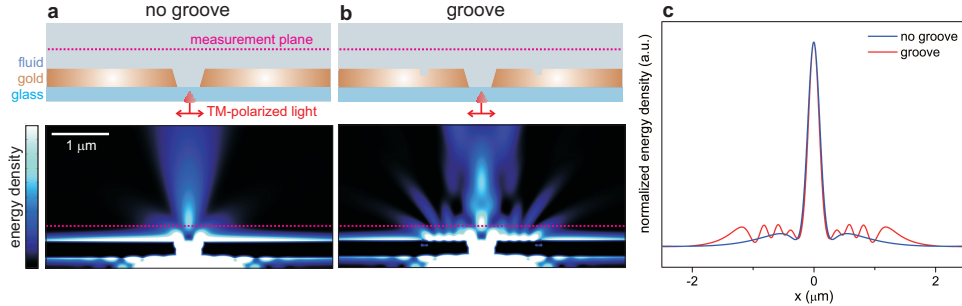


Figure 3.10: FDTD simulations of TM-polarized illumination ($\lambda_0 = 632.8$ nm) of a set of tapered slits (with parameters matching slit pairs with a nominal width of $w = 350$ nm used in the experiments) immersed in a dielectric medium where $n = 1.6$. (a) Energy density distribution for the case where the slit is (a) without grooves and (b) with grooves. (c) Normalized energy density profiles extracted from the simulations along the magenta line shown in (a) and (b), which approximates the object plane imaged by the microscope.

tive index. For convenience, the plots have been divided into shaded and unshaded areas denoting the sub-wavelength and super-wavelength regimes, respectively. In general, there is good quantitative agreement between the SPP coupling efficiency values measured through experiment and predicted through simulation. The SPP coupling efficiency in the sub-wavelength regime decreases as a function of increasing slit width, consistent with many previous observations reported in the literature [56, 60]. As the slit width transitions into the super-wavelength regime, the SPP coupling efficiency rises sharply, reaches a tell-tale peak just above the wavelength threshold, and then drops. This feature in the SPP coupling efficiency is observed for all values of the surrounding refractive index, but is most pronounced for the highest refractive index value of $n = 1.7$. It should be noted that the peak SPP coupling efficiencies are lower than that predicted for silver in the previous section due to the intrinsically higher losses in gold and the fact that groove scattering into the far-field under-estimates the SPPs present on the surface. In reality, the grooves do not perfectly scatter SPPs into the far-field and a portion of SPPs remain on the surface after interacting with the grooves. Nonetheless, the observation of a local peak in the SPP coupling efficiency as the slit width increases to super-wavelength values

supports the hypothesis that there is increased wave vector matching to the adjacent SPP mode due to the onset of higher order modes.

Can we confirm that the enhanced SPP coupling efficiency for super-wavelength slit values is due to a boost in the lateral wave vector component in the slit? Experimentally, it is not possible to locally access the near-fields associated with the interior of the slit without also perturbing the fields. Our best approach, perhaps, is to use the local field distribution in the slit calculated through simulation. As discussed in Chapter 1, the field distribution in a two-dimensional electromagnetic problem can be decomposed into its spatial frequency components by Fourier transformation. We apply this technique here, by using the FDFD method to calculate the field distribution in the vicinity of the slit and then applying a fast Fourier transform to the magnetic field in a region encompassing the slit opening, as shown in Figure 3.12. As shown in Figure 3.12(c), the Fourier amplitude of the fields along the x -axis at a spatial frequency of k_{spp} is boosted at the same super-wavelength slit width values which undergo an enhancement in coupling efficiency. This indicates a correlation between the coupling efficiency and the spatial Fourier amplitude at k_{spp} and supports the original hypothesis that higher SPP coupling efficiency in super-wavelength slits is due to the boost in the lateral wave vector component.

3.6 Summary

In this Chapter, we have proposed and validated a method to achieve high-efficiency SPP coupling method from a super-wavelength slit aperture. The crux of this method is to exploit the onset of higher-order modes in the slit when the aperture is larger than the wavelength. This work is the first to explore SPP coupling from super-wavelength slits by explicitly treating the interaction between the higher-order modes (which become non-evanescent when the slit width is increased) and SPP modes. The conclusions will assist in the continued development of SPP devices by providing a new high-efficiency and high-throughput methods for coupling to SPP modes.

3.6. Summary

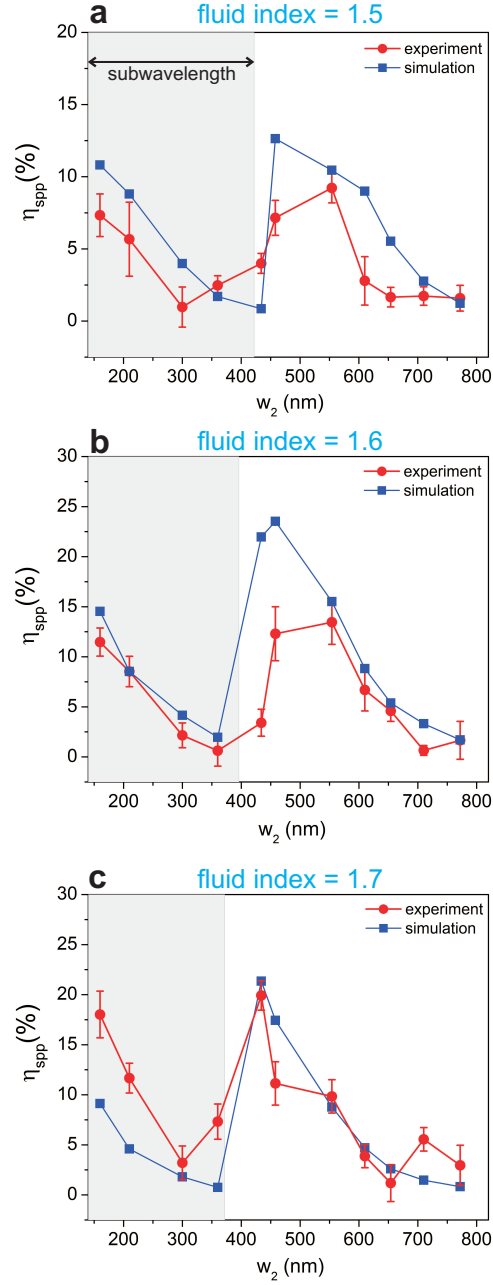


Figure 3.11: SPP coupling efficiency (η) as a function of the exit slit width (w_2) when immersed in index fluids of refractive index (a) 1.5, (b) 1.6, and (c) 1.7.

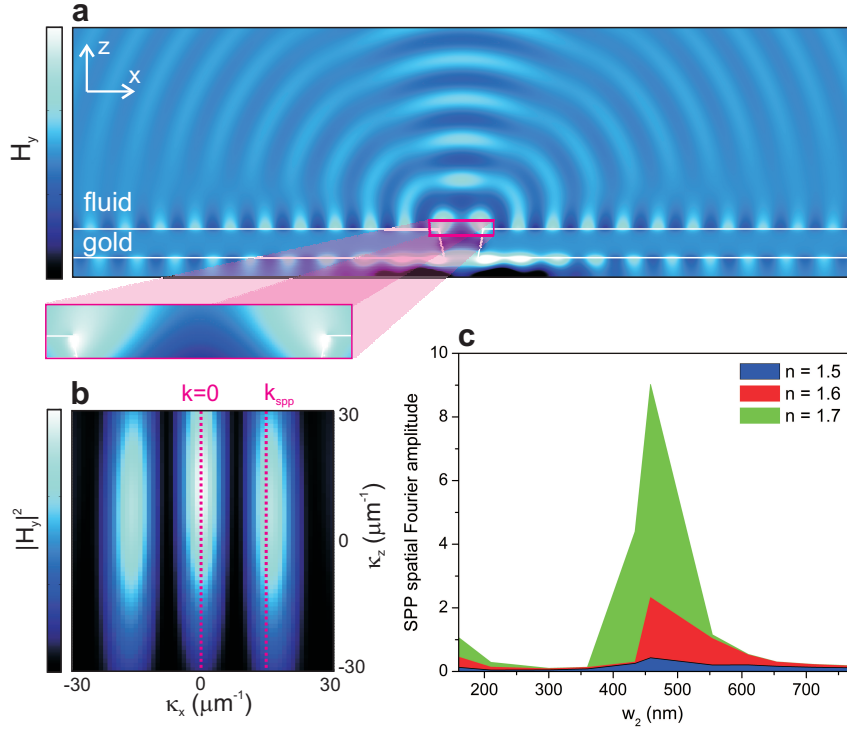


Figure 3.12: FDFD simulation of the electromagnetic response of a slit structure with a nominal width of $w = 350$ nm at $\lambda_0 = 632.8$ nm, with a zoomed-in section highlighting the fields at the slit exit. (b) Two-dimensional Fourier transformation applied to the fields at the slit exit, revealing large spatial frequency components along the horizontal (x) axis. (c) Plot of Fourier amplitude at the spatial frequency k_{spp} as a function of the slit width.

Chapter 4

Conclusion

This thesis has examined the interaction of light with small slit apertures in metallic films, focussing on the problem of light coupling from the exit of a slit aperture to surface waves sustained on the adjacent metal surface. Light interaction with small apertures is a centuries-old problem which has been critical to the development of basic concepts in optics such as the Huygens-Fresnel theory, Kirchoff's scalar diffraction theory, and Fresnel and Fraunhofer diffraction. There has been renewed interest in the problem of light transmission through small apertures since the recent discovery that apertures in metallic films can efficiently excite surface electromagnetic waves, known as surface plasmon polaritons (SPPs). Although there have been significant research efforts to apply SPPs in miniature light-based devices, the basic physical mechanism of SPP coupling from an illuminated aperture have not been fully elucidated and remains an active area of research.

In this thesis, we have proposed to study SPP coupling from a slit aperture using a simple model in which the slit and adjacent metal surface are treated as independent, semi-infinite waveguides. This approach enables the electromagnetic response of a slit structure to be treated as two waveguide boundary value problems. By mapping the electromagnetic solutions (or modes) of the waveguide sub-components, it is possible to describe light coupling from the slit to the SPP mode adjacent to the slit in terms of conventional wave vector matching. Based on this approximation, we have investigated different methods to improve SPP coupling efficiencies from various slit apertures by determining conditions that lead to wave vector matching to the SPP mode. In Chapter 2, we have introduced the possibility of using a dielectric layer to facilitate wave vector matching between the light at the exit of a slit and the SPP mode. Experiments and simulations have been conducted to show that a sub-wavelength slit coated with a thin dielectric layer can exhibit SPP coupling efficiencies that are many times greater than the coupling efficiencies without the dielectric layer. In Chapter 3, we have shown high efficiency SPP coupling can even be achieved from a slit with dimensions larger than the wavelength by exploiting the onset of the first-order

mode in the slit. This hypothesis was first developed through simulations showing large SPP coupling enhancements from a slit with the width was increased above the wavelength and then further validated by experimental measurements. A SPP coupling condition for large slits, analogous to the well-established SPP coupling condition for gratings, was proposed and verified over a limited range of parameters. Overall, the results presented in this thesis illustrate that SPP coupling from a slit can be understood and optimized through simple waveguide models and that judicious tuning of parameters such as the slit width, dielectric layer coating thickness, or the refractive index of the dielectric surrounding the slit can yield significant enhancements in SPP coupling efficiencies.

It is important to recall the key assumptions that have been used to generate the conclusions of our this work and to discuss the limitations of these assumptions. We have in general restricted our work to the study of the slit geometry, a simple geometry that has been assumed to be independent of one coordinate and can be analyzed in two dimensions. Although the analysis approach should also be valid for more complex aperture geometries such as holes, specific conditions for optimal SPP coupling from slits obtained in our work should not a priori be expected to apply to other geometries. In our analysis in Chapter 2, we have invoked a variant of the single-mode approximation in which the field in the slit is assumed to be constant, which is generally accepted to be valid only for apertures with deep sub-wavelength dimensions. In the electromagnetic simulations performed throughout the thesis, we have consistently assumed that the metal surfaces are perfectly smooth. In sections where these simulation results have been compared to experiment, it should be noted that fabricated metal surfaces are not perfectly smooth and have average surface roughness on the order of 1.3 nm. Simulations performed using the FDTD method have employed the Drude model to describe the electromagnetic response of metals. As discussed in the Appendix, the Drude model is not a completely accurate model for the permittivity of common plasmonic materials such as Ag, Au, and Al, and is particularly poor at predicting the imaginary part of the permittivity of these metals. In our experiments to measure the SPP coupling efficiency, we have made the experimental assumption that a single groove can completely scatter SPPs into the far-field. Of course, the scattering efficiency of a single groove is not perfect and the SPP coupling efficiency inferred from the far-field brightness of single grooves likely underestimates the true SPP coupling efficiency. In our proposed coupling condition given in Chapter 3, we have assumed that a guided mode in a slit incident onto the exit of the slit can be have a lateral wave vector component boosted by diffraction

from the slit exit. Although this proposal draws upon the well-established scattering concept used to describe grating coupling, the implementation of this condition for a guided mode incident onto a slit exit leads to the appearance of double counting of the lateral wave vector component of the guided mode. As discussed in Chapter 3, the appearance of double counting arises from the application of approximate scalar diffraction theory to describe the scattering process at the slit exit and can be alleviated by taking, for example, the numerically calculated field profile after the guided mode has scattered from the slit exit. Certainly, there is room for future refinement and improvement of the model to describe coupling to SPPs from larger apertures.

Although our experimental and numerical studies have been restricted to enhancing SPP coupling at visible frequencies, it should be noted that the strategies we have proposed to achieve SPP coupling enhancement can be exploited at other frequencies. To briefly demonstrate this, we have conducted FDFD simulations in which a sub-wavelength slit in a opaque metallic film coated with a thin, lossless dielectric layer (of variable thickness and fixed refractive index of $n = 1.5$) is excited with ultraviolet (UV), visible, and infrared (IR) light. For visible illumination, we have assumed a metallic film composed of silver, and for UV and IR illumination, we have assumed metallic films composed of aluminum and gold, respectively. As shown in Figure 4.1, the SPP coupling efficiency from a sub-wavelength slit subjected to either UV, visible, or IR illumination can be dramatically enhanced by simply tuning the dielectric layer thickness, based on the principles introduced and discussed in this work.

This thesis represents a first step towards better optimization of SPP coupling from apertures by using simple physical models of the coupling process to predict conditions that achieve wave vector matching. Future work in this research area should be focused on improving the physical model of SPP coupling, extending its capability to treat more complex geometries, and finding suitable applications for the SPP coupling enhancement methods proposed and demonstrated in this work. Although our physical model for SPP coupling can predict conditions that lead to wave vector matching and therefore, optimal SPP coupling, it still does not provide quantitative estimates of the amount of SPP coupling. Improving the model to enable quantitative estimates of coupling would need to go beyond simple wave vector matching concepts and may incorporate field matching algorithms [85]. To extend our treatment to more complex geometries, three-dimensional analysis techniques and simulations would have to be developed. Ultimately, the goal of such efforts would be to create design tools that would enable a

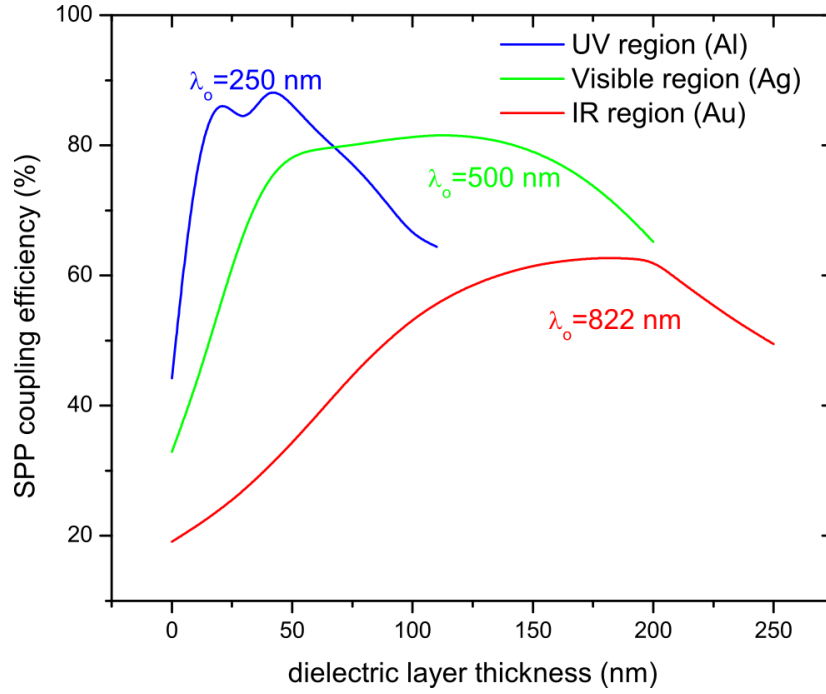


Figure 4.1: SPP coupling efficiency as a function of dielectric layer thickness calculated at representative wavelengths in the infrared, visible, and UV. For the case of UV illumination, the metal is aluminum, the slit width is 50 nm, and the incident wavelength is 250 nm. For the case of visible illumination, the metal is silver, the slit width is 100 nm, and the incident wavelength is 500 nm. For the case of IR illumination, the metal is gold, the slit width is 150 nm, and the incident wavelength is 822 nm.

practitioner to specify desired SPP wave properties (such as beam amplitude and phase profile) and retrieve an optimized aperture geometry.

In this thesis, we have explored SPP excitation using sub-wavelength and super-wavelength slits. Of the two, SPP excitation by sub-wavelength slits is a more well-established technique, and our contribution has been to introduce a coating method to refine this method to achieve very high efficiencies and therefore, high signal-to-noise ratios. It is important to keep in mind, however, that the overall SPP throughput for a sub-wavelength slit is still small and limited by its surface area. On the other hand, SPP excitation by super-wavelength slits has received very little research attention, and our contribution has been to make an initial attempt to develop a physical model for SPP excitation in this slit-width regime. We have observed that it is possible to boost the SPP coupling efficiency of a super-wavelength slit, but this generally requires the slit to be immersed in a high-index dielectric fluid. A super-wavelength slit inherently allows more light to pass through than a sub-wavelength one and thus has greater SPP throughput, but cannot achieve the same efficiency values. Future work in this area should be devoted to using the coating method that we have developed for sub-wavelength slits to achieve higher efficiencies and greater signal-to-noise ratios with super-wavelength slits. In the end, the usefulness of this work will be measured by how it is used. Given the growing number of research reports on the use of apertures in metallic films as localized, easily-manufactured sources of SPPs [86, 87], it is envisioned that the eventual commercialization of these efforts will motivate efforts to increase device efficiency, at which point the strategies and methods proposed here could prove useful.

Bibliography

- [1] P. Fischer, S. E. Skelton, C. G. Leburn, C. T. Streuber, E. M. Wright, and K. Dholakia, “The dark spots of Arago,” *Optics Express*, vol. 15, pp. 11860–11873, 2007.
- [2] J. C. Maxwell, *A Treatise on Electricity and Magnetism*. Oxford Press, 1873.
- [3] J. W. Goodman, *Introduction to Fourier Optics*. Roberts and Company Publishers, 3rd ed., 2004.
- [4] M. Born and E. Wolf, *Principles of Optics*. Cambridge University Press, 7th ed., 1999.
- [5] H. A. Bethe, “Theory of diffraction by small holes,” *Physical Review*, vol. 66, pp. 163–182, 1944.
- [6] R. F. Harrington and D. Auckland, “Electromagnetic transmission through narrow slots in thick conducting screens,” *IEEE Transactions on Antennas and Propagation*, vol. 28, pp. 616–622, 1980.
- [7] V. Klimov and V. Letokhov, “A simple theory of the near field in diffraction by a round aperture,” *Optics Communications*, vol. 106, pp. 151 – 154, 1994.
- [8] O. Kwon, S. H. Pak, J. K. So, I. Baik, S. H. Min, and G. Park, “Experimental confirmation of Bethe’s diffraction theory,” *36th International Conference on Infrared, Millimeter and Terahertz Waves*, pp. 1–2, 2011.
- [9] M. W. Kowarz, “Homogeneous and evanescent contributions in scalar near-field diffraction,” *Applied Optics*, vol. 34, pp. 3055 – 3063, 1995.
- [10] Y. Xie, A. Zakharian, J. Moloney, and M. Mansuripur, “Transmission of light through slit apertures in metallic films,” *Optics Express*, vol. 12, pp. 6106–6121, 2004.

- [11] Y. Xie, A. Zakharian, J. Moloney, and M. Mansuripur, "Transmission of light through a periodic array of slits in a thick metallic film," *Optics Express*, vol. 13, pp. 4485–4491, 2005.
- [12] R. Gordon and A. Brolo, "Increased cut-off wavelength for a subwavelength hole in a real metal," *Optics Express*, vol. 13, pp. 1933–1938, 2005.
- [13] H. Shi, C. Wang, C. Du, X. Luo, X. Dong, and H. Gao, "Beam manipulating by metallic nano-slits with variant widths," *Optics Express*, vol. 13, pp. 6815–6820, 2005.
- [14] B. Ung and Y. Sheng, "Interference of surface waves in a metallic nanoslit," *Optics Express*, vol. 15, pp. 1182–1190, 2007.
- [15] L. Verslegers, P. B. Catrysse, Z. Yu, J. S. White, E. S. Barnard, M. L. Brongersma, and S. Fan, "Planar lenses based on nanoscale slit arrays in a metallic film," *Nano Letters*, vol. 9, pp. 235–238, 2009.
- [16] A. Chandran, E. S. Barnard, J. S. White, and M. L. Brongersma, "Metal-dielectric-metal surface plasmon-polariton resonators," *Physical Review B*, vol. 85, p. 085416, 2012.
- [17] A. Taflove, "Application of the finite-difference time-domain method to sinusoidal steady-state electromagnetic-penetration problems," *IEEE Transactions on Electromagnetic Compatibility*, vol. EMC-22, pp. 191–202, 1980.
- [18] K. Yee, "Numerical solution of initial boundary value problems involving maxwell's equations in isotropic media," *IEEE Transactions on Antennas and Propagation*, vol. 14, pp. 302 – 307, 1966.
- [19] J. Berenger, "A perfectly matched layer for the absorption of electromagnetic waves," *Journal of Computational Physics*, vol. 114, pp. 185 – 200, 1994.
- [20] S. D. Gedney, "An anisotropic perfectly matched layer absorbing media for the truncation of FDTD lattices," *IEEE Transactions on Antennas and Propagation*, vol. 44, pp. 1630 – 1639, 1996.
- [21] A. Taflove and S. C. Hagness, *Computational Electrodynamics: The Finite-Difference Time-Domain Method*. Artech House, 3rd ed., 2005.

- [22] R. Rumpf, “Simple implementation of arbitrarily shaped total-field/scattered-field regions in finite-difference frequency-domain,” *Progress In Electromagnetics Research B*, vol. 36, pp. 221–248, 2012.
- [23] T. W. Ebbesen, H. J. Lezec, H. F. Ghaemi, T. Thio, and P. A. Wolff, “Extraordinary optical transmission through sub-wavelength hole arrays,” *Nature*, vol. 391, pp. 667 – 669, 1998.
- [24] H. F. Ghaemi, T. Thio, D. E. Grupp, T. W. Ebbesen, and H. J. Lezec, “Surface plasmons enhance optical transmission through subwavelength holes,” *Physical Review B*, vol. 58, pp. 6779–6782, 1998.
- [25] J. A. Porto, F. J. Garcia-Vidal, and J. B. Pendry, “Transmission resonances on metallic gratings with very narrow slits,” *Physical Review Letters*, vol. 83, pp. 2845–2848, 1999.
- [26] T. Thio, K. M. Pellerin, R. A. Linke, H. J. Lezec, and T. W. Ebbesen, “Enhanced light transmission through a single subwavelength aperture,” *Optics Letters*, vol. 26, pp. 1972–1974, 2003.
- [27] Y. Takakura, “Optical resonance in a narrow slit in a thick metallic screen,” *Physical Review Letters*, vol. 86, pp. 5601–5603, 2001.
- [28] R. Wannemacher, “Plasmon-supported transmission of light through nanometric holes in metallic thin films,” *Optics Communications*, vol. 195, pp. 107 – 118, 2001.
- [29] H. J. Lezec, A. Degiron, E. Devaux, R. A. Linke, L. Martin-Moreno, F. J. Garcia-Vidal, and T. W. Ebbesen, “Beaming light from a sub-wavelength aperture,” *Science*, vol. 297, pp. 820–822, 2002.
- [30] W. L. Barnes, A. Dereus, and T. W. Ebbesen, “Surface plasmon sub-wavelength optics,” *Nature*, vol. 424, pp. 824–830, 2003.
- [31] F. J. Garcia-Vidal, H. J. Lezec, T. W. Ebbesen, and L. Martin-Moreno, “Multiple paths to enhance optical transmission through a single sub-wavelength slit,” *Physical Review Letters*, vol. 90, p. 213901, 2003.
- [32] L. Martin-Moreno, F. J. Garcia-Vidal, H. J. Lezec, A. Degiron, and T. W. Ebbesen, “Theory of highly directional emission from a single subwavelength aperture surrounded by surface corrugations,” *Physical Review Letters*, vol. 90, p. 167401, 2003.

- [33] R. Gordon, “Light in a subwavelength slit in a metal: Propagation and reflection,” *Physical Review B*, vol. 73, p. 153405, 2006.
- [34] J. Wuenschell and H. K. Kim, “Surface plasmon dynamics in an isolated metallic nanoslit,” *Optics Express*, vol. 14, pp. 10000–10013, 2006.
- [35] A. P. Hibbins, M. J. Lockyear, and J. R. Sambles, “The resonant electromagnetic fields of an array of metallic slits acting as Fabry-Perot cavities,” *Journal of Applied Physics*, vol. 99, p. 124903, 2006.
- [36] F. J. Garcia de Abajo, “*Colloquium* : Light scattering by particle and hole arrays,” *Reviews of Modern Physics*, vol. 79, pp. 1267–1290, 2007.
- [37] L. Aigouy, P. Lalanne, H. Liu, G. Juli, V. Mathet, and M. Mortier, “Near-field scattered by a single nanoslit in a metal film.,” *Applied Optics*, vol. 46, pp. 8573–8577, 2007.
- [38] V. E. Babicheva and Y. E. Lozovik, “Role of propagating slit mode in enhanced transmission through slit arrays in a metallic films,” *Optical and Quantum Electronics*, vol. 41, pp. 299–313, 2010.
- [39] A. Otto, “Eine neue methode der anregung nichtstrahlender oberflächenplasmaschwingungen,” *Physica Status Solidi (b)*, vol. 26, pp. K99–K101, 1968.
- [40] E. Kretschmann, “The angular dependence and the polarisation of light emitted by surface plasmons on metals due to roughness,” *Optics Communications*, vol. 5, pp. 331 – 336, 1972.
- [41] H. Raether, *Surface Plasmons on Smooth and Rough Surfaces and on Gratings*. Springer, 1988.
- [42] *Biacore Sensor Surface Handbook*. GE Healthcare, online ed., <http://tinyurl.com/k33rtuo>, extracted on 26 July, 2013.
- [43] S. A. Maier, *Plasmonics: Fundamentals and Applications*. Springer Science, 1st ed., 2007.
- [44] J.-Y. Laluet, A. Drezet, C. Genet, and T. W. Ebbesen, “Generation of surface plasmons at single subwavelength slits: from slit to ridge plasmon,” *New Journal of Physics*, vol. 10, p. 105014, 2008.

- [45] A.-L. Baudrion, F. de Leon-Perez, O. Mahboub, A. Hohenau, H. Ditlbacher, F. J. Garcia-Vidal, J. Dintinger, T. W. Ebbesen, L. Martin-Moreno, and J. R. Krenn, "Coupling efficiency of light to surface plasmon polariton for single subwavelength holes in a gold film," *Optics Express*, vol. 16, pp. 3420–3429, 2008.
- [46] R. F. Oulton, D. F. P. Pile, Y. Liu, and X. Zhang, "Scattering of surface plasmon polaritons at abrupt surface interfaces: Implications for nanoscale cavities," *Physical Review B*, vol. 76, p. 035408, 2007.
- [47] J. Homola, "Surface plasmon resonance sensors for detection of chemical and biological species.," *Chemical Reviews*, vol. 108, pp. 462–493, 2008.
- [48] A. J. Haes, W. P. Hall, L. Chang, W. L. Klein, and R. P. Van Duyne, "A localized surface plasmon resonance biosensor: first steps toward an assay for alzheimer's disease," *Nano Letters*, vol. 4, pp. 1029–1034, 2004.
- [49] N. C. Lindquist, P. Nagpal, A. Lesuffleur, D. J. Norris, and S.-H. Oh, "Three-dimensional plasmonic nanofocusing," *Nano Letters*, vol. 10, pp. 1369–1373, 2010.
- [50] S. Bozhevolnyi, V. Volkov, E. Devaux, J.-Y. Laluet, and T. Ebbesen, "Channelling surface plasmons," *Applied Physics A*, vol. 89, pp. 225–231, 2007.
- [51] L. Yin, V. K. Vlasko-Vlasov, J. Pearson, J. M. Hiller, J. Hua, U. Welp, D. E. Brown, and C. W. Kimball, "Subwavelength focusing and guiding of surface plasmons," *Nano Letters*, vol. 5, pp. 1399–1402, 2005.
- [52] H. Ditlbacher, A. Hohenau, D. Wagner, U. Kreibig, M. Rogers, F. Hofer, F. R. Aussenegg, and J. R. Krenn, "Silver nanowires as surface plasmon resonators," *Physical Review Letters*, vol. 95, p. 257403, 2005.
- [53] H. Lezec and T. Thio, "Diffracted evanescent wave model for enhanced and suppressed optical transmission through subwavelength hole arrays," *Optics Express*, vol. 12, pp. 3629–3651, 2004.
- [54] G. Gay, O. Alloschery, B. V. de Leseqno, J. Weiner, and H. J. Lezec, "Surface wave generation and propagation on metallic subwavelength structures measured by far-field interferometry," *Physical Review Letters*, vol. 96, p. 213901, 2006.

- [55] F. Kalkum, G. Gay, O. Alloschery, J. Weiner, H. J. Lezec, Y. Xie, and M. Mansuripur, “Surface-wave interferometry on single subwavelength slit-groove structures fabricated on gold films,” *Optics Express*, vol. 15, pp. 2613–2621, 2007.
- [56] P. Lalanne, J. P. Hugonin, and J. C. Rodier, “Theory of surface plasmon generation at nanoslit apertures,” *Physical Review Letters*, vol. 95, p. 263902, 2005.
- [57] P. Lalanne, J. P. Hugonin, and J. C. Rodier, “Approximate model for surface-plasmon generation at slit apertures,” *Journal of the Optical Society of America A*, vol. 23, pp. 1608–1615, 2006.
- [58] H. F. Schouten, N. Kuzmin, G. Dubois, T. D. Visser, G. Gbur, P. F. A. Alkemade, H. Blok, G. W. t. Hooft, D. Lenstra, and E. R. Eliel, “Plasmon-assisted two-slit transmission: Young’s experiment revisited,” *Physical Review Letters*, vol. 94, p. 053901, 2005.
- [59] J. Renger, S. Grafström, and L. M. Eng, “Direct excitation of surface plasmon polaritons in nanopatterned metal surfaces and thin films,” *Physical Review B*, vol. 76, p. 045431, 2007.
- [60] H. W. Kihm, K. G. Lee, D. S. Kim, J. H. Kang, and Q.-H. Park, “Control of surface plasmon generation efficiency by slit-width tuning,” *Applied Physics Letters*, vol. 92, p. 051115, 2008.
- [61] R. Mehfuz, M. W. Maqsood, and K. J. Chau, “Enhancing the efficiency of slit-coupling to surface-plasmon-polaritons via dispersion engineering,” *Optics Express*, vol. 18, pp. 18206–18216, 2010.
- [62] R. Mehfuz, F. A. Chowdhury, and K. J. Chau, “Imaging slit-coupled surface plasmon polaritons using conventional optical microscopy,” *Optics Express*, vol. 20, pp. 10526–10537, 2012.
- [63] M. W. Maqsood, R. Mehfuz, and K. J. Chau, “High-throughput diffraction-assisted surface-plasmon-polariton coupling by a super-wavelength slit,” *Optics Express*, vol. 18, pp. 21669–21677, 2010.
- [64] F. Lopez-Tejeira, S. G. Rodrigo, L. Martin-Moreno, F. J. Garcia-Vidal, E. Devaux, T. W. Ebbesen, J. R. Krenn, P. Radko, S. I. Bozhevolnyi, M. U. Gonzalez, J. C. Weeber, and A. Dereux, “Efficient unidirectional nanoslit couplers for surface plasmons,” *Nature Physics*, vol. 3, pp. 324–328, 2007.

- [65] A. Drezet, A. Hohenau, D. Koller, A. Stepanov, H. Ditlbacher, B. Steinberger, F. Aussenegg, A. Leitner, and J. Krenn, “Leakage radiation microscopy of surface plasmon polaritons,” *Materials Science and Engineering: B*, vol. 149, pp. 220 – 229, 2008.
- [66] J. Grandidier, S. Massenot, G. C. des Francs, A. Bouhelier, J.-C. Weeber, L. Markey, A. Dereux, J. Renger, M. U. González, and R. Quidant, “Dielectric-loaded surface plasmon polariton waveguides: Figures of merit and mode characterization by image and Fourier plane leakage microscopy,” *Physical Review B*, vol. 78, p. 245419, 2008.
- [67] S. I. Bozhevolnyi, I. I. Smolyaninov, and A. V. Zayats, “Near-field microscopy of surface-plasmon polaritons: Localization and internal interface imaging,” *Physical Review B*, vol. 51, pp. 17916–17924, 1995.
- [68] J.-C. Weeber, J. R. Krenn, A. Dereux, B. Lamprecht, Y. Lacroute, and J. P. Goudonnet, “Near-field observation of surface plasmon polariton propagation on thin metal stripes,” *Physical Review B*, vol. 64, p. 045411, 2001.
- [69] H. Ditlbacher, J. R. Krenn, N. Felidj, B. Lamprecht, G. Schider, M. Salerno, A. Leitner, and F. R. Aussenegg, “Fluorescence imaging of surface plasmon fields,” *Applied Physics Letters*, vol. 80, pp. 404–406, 2002.
- [70] P. B. Johnson and R. W. Christy, “Optical constants of the noble metals,” *Physical Review B*, vol. 6, pp. 4370 – 4379, 1972.
- [71] A. Bouhelier and G. P. Wiederrecht, “Excitation of broadband surface plasmon polaritons: Plasmonic continuum spectroscopy,” *Physical Review B*, vol. 71, p. 195406, 2005.
- [72] Z.-M. Qi, M. Wei, H. Matsuda, I. Honma, and H. Zhou, “Broadband surface plasmon resonance spectroscopy for determination of refractive-index dispersion of dielectric thin films,” *Applied Physics Letters*, vol. 90, p. 181112, 2007.
- [73] B. L. Feber, J. Cesario, H. Zeijlemaker, N. Rotenberg, and L. Kuipers, “Exploiting long-ranged order in quasiperiodic structures for broadband plasmonic excitation,” *Applied Physics Letters*, vol. 98, p. 201108, 2011.
- [74] R. M. Gelfand, L. Bruderer, and H. Mohseni, “Nanocavity plasmonic device for ultrabroadband single molecule sensing,” *Optics Letters*, vol. 34, pp. 1087–1089, 2009.

- [75] B. Roberts and P. C. Ku, "Broadband characteristics of surface plasmon enhanced solar cells," *35th IEEE Photovoltaic Specialists Conference (PVSC)*, pp. 2952–2954, 2010.
- [76] F. Djidjeli, E. Jaberansary, H. M. H. Chong, and D. M. Bagnall, "Broadband plasmonic couplers for light trapping and waveguiding," *Proceedings of SPIE*, vol. 7712, pp. 77122R–8, 2010.
- [77] J. Chen, Z. Li, M. Lei, S. Yue, J. Xiao, and Q. Gong, "Broadband unidirectional generation of surface plasmon polaritons with dielectric–film–coated asymmetric single–slit," *Optics Express*, vol. 19, pp. 26463–26469, 2011.
- [78] R. Verre, K. Fleischer, O. Ualibek, and I. V. Shvets, "Self-assembled broadband plasmonic nanoparticle arrays for sensing applications," *Applied Physics Letters*, vol. 100, p. 031102, 2012.
- [79] J.-S. Bouillard, S. Vilain, W. Dickson, G. A. Wurtz, and A. V. Zayats, "Broadband and broadangle SPP antennas based on plasmonic crystals with linear chirp," *Scientific Reports*, p. 829, 2012.
- [80] G. Kirchhoff, "Zur theorie der lichtstrahlen," *Annalen Der Physik*, vol. 254, pp. 663–695, 1883.
- [81] A. G. Brolo, R. Gordon, B. Leathem, and K. L. Kavanagh, "Surface plasmon sensor based on the enhanced light transmission through arrays of nanoholes in gold films," *Langmuir*, vol. 20, pp. 4813–4815, 2004.
- [82] R. Buckley and P. Berini, "Radiation suppressing metallo-dielectric optical waveguides," *Journal of Lightwave Technology*, vol. 27, pp. 2800–2808, 2009.
- [83] S. H. Talisa, "Application of davidenkos method to the solution of dispersion relations in lossy waveguiding systems," *IEEE Transactions on Microwave Theory and Techniques*, vol. 33, pp. 967 – 971, 1985.
- [84] M. W. Maqsood, *Metal Waveguides for Multi-Axial Light Guiding at Nanometer Scales*. Master's Thesis, The University of British Columbia, Nov. 2011.
- [85] A. Yariv and P. Yeh, *Optical Waves in Crystals: Propagation and Control of Laser Radiation (Wiley Series in Pure and Applied Optics)*. Wiley-Interscience, 2002.

Bibliography

- [86] B. Wang and P. Lalanne, “Surface plasmon polaritons locally excited on the ridges of metallic gratings,” *Journal of Optical Society of America. A*, vol. 27, pp. 1432–1441, 2010.
- [87] J. Feng, V. S. Siu, A. Roelke, V. Mehta, S. Y. Rhieu, G. T. R. Palmore, and D. Pacifici, “Nanoscale plasmonic interferometers for multispectral, high-throughput biochemical sensing,” *Nano Letters*, vol. 12, pp. 602–609, 2012.
- [88] P. Drude, “Zur elektronentheorie der metalle,” *Annalen Der Physik*, vol. 306, p. 506, 1900.
- [89] P. Drude, “Zur elektronentheorie der metalle; ii. teil. galvanomagnetische und thermomagnetische effecte,” *Annalen Der Physik*, vol. 308, p. 369, 1900.
- [90] E. J. Zeman and G. C. Schatz, “An accurate electromagnetic theory study of surface enhancement factors for silver, gold, copper, lithium, sodium, aluminum, gallium, indium, zinc, and cadmium,” *Journal of Physical Chemistry*, vol. 91, pp. 634 – 643, 1987.
- [91] D. R. Lide, *CRC Handbook of Chemistry and Physics*. CRC Press, 88th ed., 2007.
- [92] M. J. Madou, *Fundamentals of Microfabrication: the Science of Miniaturization*. CRC Press, 2nd ed., 2002.

Appendices

Appendices A

Drude Model and its Limitations

Metals are characterized by a real permittivity that is negative. The frequency-dependent permittivity of metals can be modeled to good approximation by a simple kinetic model of an electron gas proposed by Paul Drude in 1900 [88, 89]. The model begins by considering a density of unbounded free electrons. From the equation of motion for an electron in the gas under the influence of a time-varying electric field, the permittivity of the electron gas can be shown to be

$$\underline{\epsilon}(\omega) = 1 - \frac{\omega_p^2}{\omega(\omega + i/\tau)}. \quad (\text{A.1})$$

where $1/\tau$ is the collision frequency and ω_p is the plasma frequency. Rewriting Eq. A.1 into distinctive real and imaginary parts yields

$$\underline{\epsilon}(\omega) = 1 - \frac{\omega_p^2}{(\omega^2 + 1/\tau^2)} + i \frac{\omega_p^2 \tau}{\omega(1 + \omega^2 \tau^2)}. \quad (\text{A.2})$$

Assuming negligible damping $1/\tau \simeq 0$, the permittivity can be written simply as

$$\underline{\epsilon}(\omega) = 1 - \frac{\omega_p^2}{\omega^2}, \quad (\text{A.3})$$

which is negative when the frequency is less than the plasma frequency. Thus, for a low-loss electron gas, the plasma frequency sets an upper frequency bound below which the gas behaves like a metal.

Three metals that have been commonly used to sustain SPPs are gold (Au), silver (Ag), and aluminum (Al). As seen in Table A.1, a common feature of these metals is that their collision rates are several orders of magnitude less than the plasma frequency, meaning that they all have relatively low loss. Of the three metals, Ag has the lowest losses, followed by Au and then Al. Although Al has the largest losses, its high plasma frequency means

Table A.1: Plasma frequency and collision rate measured by Zeman and Sachts [90] for Ag, Au, and Al

Metal	Plasma frequency ω_p (Hz)	Collision rate τ^{-1} (s^{-1})
Silver	2.186×10^{15}	5.139×10^{12}
Gold	2.15×10^{15}	17.14×10^{12}
Aluminium	2.911×10^{15}	31.12×10^{12}

it retains its metallic-like behavior at higher frequencies than Au and Ag, making it attractive for application in the deep UV. Ag is perhaps the most ideal metal in terms of its low loss, but it is reactive to sulphur in the atmosphere and tarnishes easily. Au has moderate losses and is only metallic for frequencies below the red, but boasts the advantages of chemical inertness and ease of deposition. In this thesis, we will use both Ag and Au to form SPP-sustaining surfaces.

Because we have used the Drude model in the FDTD simulators to describe the permittivity of metals, it will be useful to briefly compare predictions of the permittivity made by the Drude model (based on the parameters in Table A.1) against experimentally-measured values of the permittivity available in the literature. For Au and Ag, we use experimental data from Johnson and Christy [70]. For Al, we use experimental data from the CRC Handbook of Chemistry and Physics [91]. As seen in Figures A.1, A.2, and A.3, the Drude model is fairly accurate in modeling the real part of the permittivity for all three metals over a wide frequency range. Discrepancies in the Drude model predictions of the imaginary part of the permittivity for all three metals versus the experimental data are due to interband transitions, which are not included in Eqn. A.1 but can be implemented, for instance, by restricting the free-electron approximation and modeling electrons as bound, resonant entities.

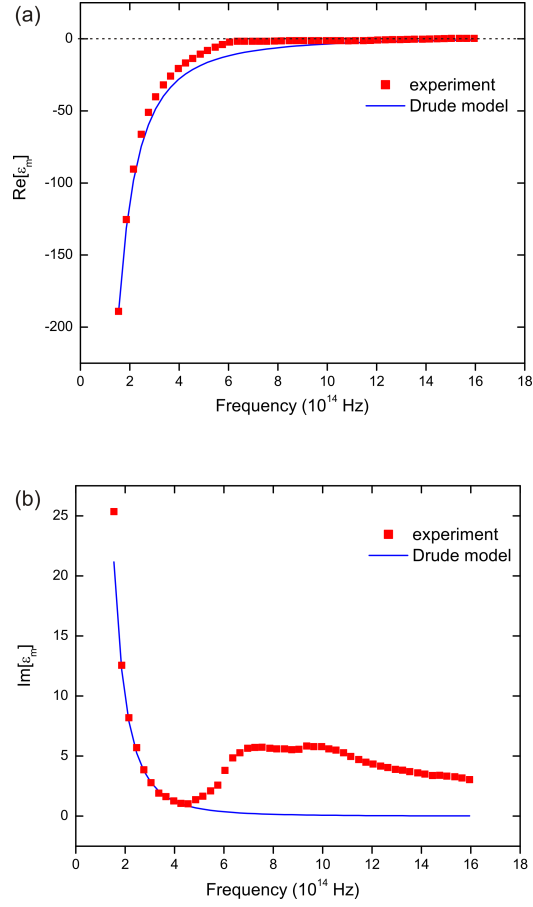


Figure A.1: Permittivity values of gold predicted by the Drude model and obtained from experimental measurements [70].

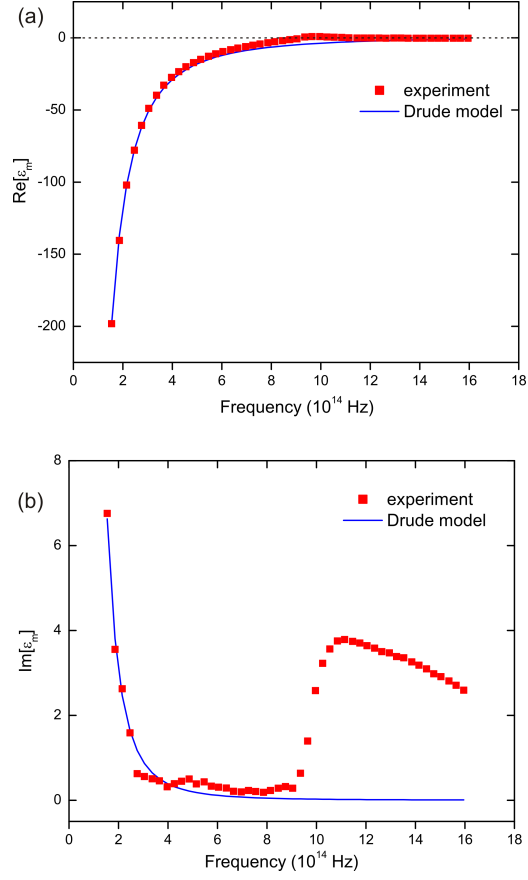


Figure A.2: Permittivity values of silver predicted by the Drude model and obtained from measurements [70].

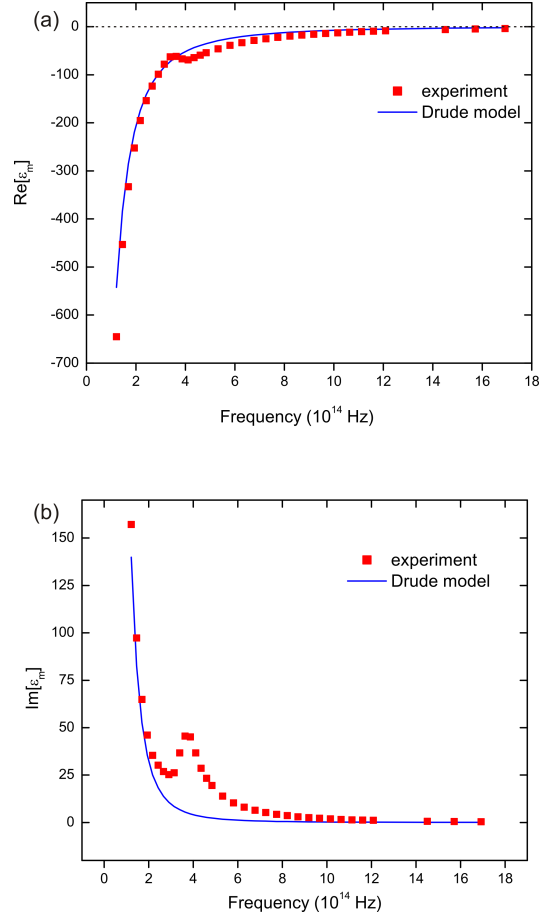


Figure A.3: Permittivity values of aluminum predicted by the Drude model and obtained from measurements [91].

Appendices B

Fabrication Tools

We have used a number of nanofabrication tools to build various slit devices used in the experiments of this thesis. The general methodology employed was to deposit a thin layer of metal (either gold or silver) on a microscope glass slide, etch features into the metal film using focused ion beam milling, and apply various dielectric coatings. This appendix will briefly discuss the salient features of the various tools used.

Physical vapor deposition

We have used three different types of deposition systems based either on thermal evaporation, electron-beam evaporation, or sputtering.

Thermal evaporation

Thermal evaporation is based on evaporating a source material in vacuum using resistance-heating. In vacuum, the vaporized particles travel directly from the source to the substrate, where they condense back to a solid state. Thermal evaporation is one of the simplest ways to deposit material onto a substrate, but is limited to low-melting-point metals. One major disadvantage is that the process is wasteful of the source material and evaporated films generally exhibit poor adhesion. One way to increase adhesion is to first lay down an ultra-thin (thickness smaller than 10 nm) layer on the substrate before depositing the source material.

For the experiments in Chapter 2, we used a NRC 3115 thermal evaporator deposition system, which is a custom built system designed and manufactured by the Simon Fraser University Technical Centre. This system was used to deposit a 300-nm-thick silver film onto a glass substrate. A 5-nm-thick chromium layer was used to increase adhesion between the substrate and silver. The measured surface roughness of the film was approximately 1.1 - 1.4 nm.

Electron-beam evaporation

Electron beam (e-beam) evaporation is based on bombarding a source material with an electron beam given off by a charged tungsten filament under high vacuum. The electron beam applies immense heat to the target material and vaporizes it. The vaporized particles then precipitate into solid form, coating everything in the vacuum chamber including the substrate. E-beam deposition provides high material deposition rates with relatively low waste of the source material. It is economically suitable for depositing expensive metals such as gold and platinum.

For the experiments in Chapter 3, we used a Lesker PVD 75 Deposition System to deposit a 300-nm-thick gold film onto microscope glass substrates. A 5-nm-thick chromium layer was used to increase adhesion between the glass substrate and gold film. The measured surface roughness of the film was on the order of 1.1 - 1.3 nm.

Sputter deposition

Sputter deposition is based upon ion bombardment of a source material, the target. Ion bombardment results in a vapor consisting of atoms from the target material. The most common approach for growing thin films by sputter deposition is to use a magnetron source in which positive ions present in the plasma of a magnetically enhanced glow discharge bombard the target.

For the broadband experiments in Chapter 2, we used a Lesker PVD 75 Deposition System to deposit a 300-nm-thick silver film onto microscope glass substrates. A 5-nm-thick chromium layer was used to increase the adhesion. The measured surface roughness of the film was on the order of 1.3 - 1.5 nm.

Focused ion beam milling

Focused ion beam milling is a direct etching process that does not require the use of masking and process chemicals and is capable of sub-micrometer feature resolution. The ion source, usually liquid gallium, is heated up and then a high acceleration voltage is applied to extract Ga^+ ions. Electrostatic lenses and other control mechanisms are used to guide and accelerate the ions towards the substrate. The incident ions bombard the substrate and material from the substrate is etched. To etch a desired feature, the focused ion beam is rastered digitally across the area to be milled. FIB is simple

and versatile, and it has gained widespread use for fabricating miniaturized structures such as high-aspect-ratio surgical burbs, vertical field emitters, and probe tips [92]. In our experiments, we have used a FEI Strata Dual Beam 235 system, with a focused ion beam resolution of 7 nm and a focused electron beam resolution of 3 nm.

Spin coating

We used Laurell WS-400B-6NPP-LITE precision spin coater to coat PMMA on metal substrates. We use the standard spinning speeds provided in the table below to target the desired thickness. After spinning, substrates are baked at a temperature of 180 ° for 1 minute. The thickness is re-checked by a high-sensitivity surface profiler (Tencor P10) with 1 Å resolution.

Table B.1: Spin speed of the Laurell WS-400B-6NPP-LITE coater versus the expected thickness and experimentally measured PMMA layer thickness

Speed (rpm)	Expected thickness (nm)	Measured thickness (nm)
3100	60	58.0
2500	80	78.6
1400	100	101.3
1200	120	122.5
1050	140	140.0
980	160	160.3